

ABSTRACT

KAJBAFVALA, AMIR. High Strength Silver/Alumina Sheath for $\text{Bi}_2\text{Sr}_2\text{CaCu}_2\text{O}_{8+x}$ Conductor. (Under the direction of Prof. Justin Schwartz).

Ongoing advances in high energy physics depend on developing high field superconducting (HTS) magnets capable of producing fields in excess of 20 T. These HTS magnets have the potential to be transformative for a variety of applications, including magnets for future high-energy physics accelerators. Neither NbTi nor Nb_3Sn can provide fields greater than 18 T in dipole magnets or 20-22 T in solenoids, so future devices require HTS materials capable of generating high magnetic field. The potential candidates are $\text{YBa}_2\text{Cu}_3\text{O}_{7-\delta}$ (YBCO) coated conductor tapes and $\text{Bi}_2\text{Sr}_2\text{CaCu}_2\text{O}_{8+x}$ (Bi2212) round wire. YBCO tapes are highly anisotropic, constraining magnet design and adding complexity to its fabrication. Bi2212 is the only HTS material available as an isotropic multifilamentary round wire with high critical current density (J_c), which is preferred for magnets.

Ag/0.20wt%Mg is the most commonly used alloy for the outer sheath of Bi2212 wire. Despite the recent successes with Ag/0.20wt%Mg sheathed Bi2212, the use of Ag/0.20wt%Mg for the outer alloy sheath poses some challenges and limitations, including increased difficulty in conductor manufacturing. The alloy has low strength in the un-reacted condition and loses ductility rapidly as it is drawn, necessitating frequent anneals. Annealing restores ductility, but it must be done in an inert atmosphere or MgO will precipitate on the grain boundaries and embrittle the alloy, making further cold working impossible.

In this work, we report on dispersion-strengthened (DS) Ag/Al alloys with various compositions as potential candidates for sheathing Bi2212 wire. The fabrication of Ag/Al alloys by powder metallurgy, their internal oxidation heat treatment to form DS Ag/Al alloy, the relationship between microstructure, physical and mechanical properties of the DS Ag/Al alloys are studied in detail. Next, the Ag/Al alloys are used for making Bi2212 wire. Heat treatment, microstructure, mechanical and electrical properties of Bi2212/AgAl wires having various Al content are studied to improve the strain sensitivity of Bi2212 after partial melt processing (PMP). The properties of Ag/Al alloys and Bi2212/AgAl wires are compared with Ag/0.20wt%Mg alloy and Bi2212/AgMg wire.

The non-optimized DS Ag/0.50wt%Al alloy showed high yield strength and tensile strength in the annealed condition at both room temperature and 4.0 K. The DS Ag/0.50wt%Al alloy also showed significant ductility at 4.0 K, i.e., a temperature at which Ag and Ag/0.20wt%Mg have little measurable ductility. Transport measurements showed that the Bi2212/Ag0.50Al wires outperform Bi2212/Ag0.20Mg wires by nearly 50%, indicating that the Al₂O₃ precipitates in the sheath have neither any significant effect on oxygen solubility or oxygen diffusion through the sheath, nor any detrimental reactions with the Bi2212 filaments. Tensile studies showed that the as-drawn Bi2212/Ag0.50Al wire has very high strength. After PMP, the Bi2212/Ag0.50Al wire not only had yield and tensile strength that were slightly higher than those of Bi2212/Ag0.20Mg wire but also exhibited > 2% elongation, which was several times higher than that of Bi2212/Ag0.20Mg. The internal oxidation heat treatment was optimized to maximize the strength and modulus of DS Ag/Al alloy and it was found that the Ag/Al alloy oxidized at 675-700°C for 4 hours gave the

highest tensile strength and hardness after PMP. In addition, this alloy could retain its fine grain size and strength during PMP in oxygen.

Scanning transmission electron microscope studies demonstrated the formation of nanosize MgO and Al₂O₃ precipitates via internal oxidation. Large spherical MgO precipitates were formed on the Ag grain boundaries of Ag/0.20wt%Mg alloy sheath, whereas the Al₂O₃ precipitates were distributed homogenously in the DS Ag/Al alloy. These large MgO precipitates made the Bi2212/Ag0.20Mg wire more brittle than Bi2212/AgAl wire. EDS elemental mappings demonstrated that less Cu diffused-out of the Bi2212 filament cores in the Bi2212/Ag0.75Al wire during PMP than that of Bi2212/Ag0.20Mg.

© Copyright 2014 by Amir Kajbafvala

All Rights Reserved

High Strength Silver/Alumina Sheath for $\text{Bi}_2\text{Sr}_2\text{CaCu}_2\text{O}_{8+x}$ Conductor

by
Amir Kajbafvala

A dissertation submitted to the Graduate Faculty of
North Carolina State University
in partial fulfillment of the
requirements for the degree of
Doctor of Philosophy

Materials Science and Engineering

Raleigh, North Carolina

2014

APPROVED BY:

Prof. Justin Schwartz
Committee Chair

Prof. Ronald O. Scattergood

Prof. Frank Hunte

Prof. Mohammed A. Zikry

DEDICATION

To my beloved, friend and wife, Maryam, whom I owe my love and trust and whom I always share my reverie. This would have never happened without her unsparing supports.

And,

To my parents, Ali-Akbar and Farkhondeh, who taught me the value of patience.

BIOGRAPHY

Amir Kajbafvala received the B.Sc. degree in materials engineering and industrial metallurgy from Shahid Chamran University of Ahvaz, Ahvaz, Iran, in July 2004, and the M.Sc. degree in materials science and engineering from Sharif University of Technology, Tehran, Iran, in January 2007. After his master's degree, he moved to the department of advanced materials, Materials and Energy Research Center, Karaj, Iran, where he was a research assistant for two and a half years. Amir came to the US in August 2009 and joined Prof. Justin Schwartz's research group at North Carolina State University as a PhD student. He took his PhD in materials science and engineering in December 2013.

ACKNOWLEDGMENTS

I would like to express my gratitude to my advisor Prof. Justin Schwartz for his great supervision, patience and support throughout this research. I also thank Profs. Hunte, Scattergood and Zikry for being members of my PhD committee and giving thoughtful suggestions.

Many thanks are deserved for Dr. Yi Liu (NCSU) for his help for the microscopy work.

Also, I would like to thank Dr. Nachtrab (Supercon Inc.) for his kind helps during my experimental work.

I would also like to thank Edna Deas who gave me numerous help since my admission until graduation.

Support for this work by the US Department of Energy, Office of High Energy Physics, SBIR and STTR Phase I and II; Grant DE-SC0004268, is gratefully acknowledged.

Finally, I would like to thank my lovely wife, Maryam, for her great patience, guidance, encouragement, and kind support.

TABLE OF CONTENTS

LIST OF TABLES	ix
LIST OF FIGURES	xi
CHAPTER 1	1
1.1. General background	1
1.1.1. Superconductivity discovery and general properties	1
1.1.2. Superconductors classifications	5
1.1.3. Superconducting critical properties	7
1.1.4. Applications of superconductor materials	8
1.1.5. Source of stresses in superconducting applications	10
1.2. $\text{Bi}_2\text{Sr}_2\text{Ca}_1\text{Cu}_2\text{O}_x$ (Bi2212)	12
1.2.1. Discovery and general properties	12
1.2.2. Bi2212 round wire fabrication, heat treatment and microstructure	14
1.2.3. Bi2212 sheath materials	18
1.2.4. Internal oxidation of Ag alloys	19
1.2.5. Attempts to improve electromechanical properties of Bi2212	21
1.2.6. Attempts on using various sheath alloys for Bi2212	30
1.3. Objectives of this work	32
1.4. References cited	35
CHAPTER 2	47
2.1. Sample fabrication	47
2.1.1. Pure silver	47
2.1.2. Ag/Al alloy	48
2.1.3. Ag/0.20wt%Mg alloy (Ag/Mg)	50
2.1.4. Bi2212 conductor	51
2.2. Heat treatment	54
2.2.1. Annealing	54
2.2.2. Internal oxidation	54
2.2.3. Melt processing of Bi2212	55
2.3. Characterization	58

2.3.1.	Microstructure.....	58
2.3.1.1.	Optical imaging	58
2.3.1.2.	Scanning Electron Microscopy (SEM).....	58
2.3.1.3.	Transmission Electron Microscopy (TEM).....	59
2.3.1.4.	Focused Ion Beam (FIB)	59
2.3.1.5.	Aberration corrected Scanning Transmission Electron Microscopy.....	60
2.3.2.	Mechanical behavior.....	60
2.3.2.1.	Hardness test.....	60
2.3.2.2.	Tensile test.....	61
2.3.3.	Electrical behavior	63
2.3.3.1.	Critical current (I_c) test	63
2.3.3.2.	Resistivity vs. temperature (ρ -T).....	66
2.3.4.	Coil studies.....	67
2.4.	References cited.....	67
CHAPTER 3		68
3.1.	Background and motivation.....	68
3.2.	Experimental method.....	70
3.3.	Results and Discussion	72
3.3.1.	Part I: Alloy characterization	72
3.3.1.1.	Microstructural observations	72
3.3.1.2.	Mechanical properties.....	73
3.3.1.2.1.	RT tensile test for alloy sheets	73
3.3.1.2.2.	DS Ag/0.50wt%Al solid alloy wire tensile behavior at RT, 4.0K	78
3.3.1.2.3.	Vickers micro-hardness (HVN) measurements.....	79
3.3.1.2.4.	Tensile samples fractography.....	82
3.3.1.3.	Electrical properties.....	82
3.3.1.3.1.	Resistivity measurements.....	82
3.3.2.	Part II: Bi2212/Ag0.50Al multifilamentary RW conductor	84
3.3.2.1.	Bi2212/Ag0.50Al microstructure	84
3.3.2.2.	Tensile behavior of Bi2212/Ag0.50Al RW conductor at RT, 77 K, 4.0K	89
3.3.2.3.	I_c measurements.....	93

3.3.2.4. Coil studies	94
3.4. Summary	96
3.5. References cited	97
CHAPTER 4	98
4.1. Background and motivation	98
4.2. Experimental method	99
4.3. Results	101
4.3.1. Silver/aluminum alloy synthesis	101
4.3.2. Mechanical properties	105
4.3.2.1. Hardness measurements	105
4.3.2.2. Room temperature tensile behavior	109
4.3.3. Microstructural observations	110
4.3.4. Electrical resistivity	111
4.4. Discussion	116
4.5. Summary	120
4.6. References cited	120
CHAPTER 5	123
5.1. Background and motivation	123
5.2. Experimental method	124
5.3. Results	125
5.3.1. Microstructure	125
5.3.1.1. Grain size measurements	125
5.3.1.2. Oxide precipitates size, distribution and chemical composition	132
5.3.1.3. Tracking of Cu diffusion using high resolutions EDS mapping	154
5.3.2. Mechanical behavior	162
5.3.2.1. Hardness measurement	162
5.3.2.2. Tensile behavior	163
5.3.3. Transport measurement	165
5.4. Discussion	167
5.5. Summary	171
5.6. References cited	173

CHAPTER 6	175
6.1. Conclusions.....	175
6.2. Recommendation for future work.....	180
6.3. Referenced cited.....	181

LIST OF TABLES

Table 2-1: Bi2212 wires specifications used in this study	53
Table 3-1: Various alloy sheet and wire samples and their processing conditions	71
Table 3-2: RT tensile test results for pure Ag, Ag/0.20wt%Mg and DS Ag/0.50wt%Al sheet alloys	77
Table 3-3: RT tensile properties for DS Ag/0.50wt%Al solid alloy wires with various heat treatments	79
Table 3-4: Tensile behaviors of DS Ag/0.50wt%Al solid alloy wires at 4.0 K with various heat treatments	81
Table 3-5: Vickers micro-hardness (HVN) for all alloy sheets	81
Table 3-6: Electrical resistivity as a function of temperature for pure Ag and DS Ag/0.50wt%Al solid alloy wires	84
Table 3-7: RT tensile properties of Bi2212/Ag0.20Mg and Bi2212/Ag0.50Al wires before and after PMP heat treatment	91
Table 3-8: Tensile properties of Bi2212/Ag0.50Al wires after PMP heat treatment at 77 K and 4.0 K along with that of Bi2212/Ag0.20Mg at RT	92
Table 3-9: Short sample I_c (A), n-value and J_c (A/mm ²) results of Bi2212/Ag0.50Al and Bi2212/Ag0.20Mg wires at self-field after PMP heat treatment	93
Table 4-1: HVN for non-oxidized and internally oxidized alloys versus oxidation temperatures and times	107
Table 4-2: Comparing HVN for internally oxidized Ag/Al alloys pre- and post-PMP	108
Table 4-3: Comparison of HVN for Ag/0.50wt%Al and Ag/0.75wt%Al alloys heat treated in various atmospheres	111
Table 5-1: Conductors specifications. All wires are double-restack with an outer diameter of 0.8 mm	125
Table 5-2: HVN measured on the outer alloy sheath of Bi2212 wires at various heat treatment conditions	163

Table 5-3: Room temperature tensile test results for Bi2212 round wires 166
Table 5-4: Transport measurements at 4.2K, self-field 167

LIST OF FIGURES

Figure 1-1: Change of electrical resistance with temperature for a superconductor and normal material.	3
Figure 1-2: History of developing superconducting material by critical temperature.....	4
Figure 1-3: Diagram of the Meissner effect. Magnetic field lines, represented as arrows, are excluded from a superconductor body when it is below its critical temperature.....	5
Figure 1-4: Superconducting critical surface, it defines a boundary for operation of superconducting materials.	8
Figure 1-5: Critical current density vs. applied magnetic field [20].....	14
Figure 1-6: Schematic diagram of PIT method to Bi2212 make wires and tapes [26].....	15
Figure 1-7: Time-temperature profile for partial melt processing used in this study (not to scale).	16
Figure 1-8: Optical micrographs showing cross section of a Bi2212 RW, a) before PMP (green wire), and b) after PMP heat treatment.....	17
Figure 1-9: a) polished cross-section of Bi2212/Ag/Ag composite wire, and b) measured tensile stress-strain curve of Bi2212 wire at room temperature [75].....	22
Figure 1-10: a) Tensile stress-strain curves of heat-treated Ag and Ag alloys measured at room temperature, and b) mechanical properties of pure Ag and a selection of Ag alloys at room temperature [69].	24
Figure 1-11: a) Results of $I_c(\epsilon)$ for a selection of strain values, obtained in tensile strain at 4.0 K and 16 T. Each pair of unprimed and primed letters indicates a loaded strain point (solid symbol) and its corresponding partially unloaded strain point (empty symbol), respectively. I_c values showed an unambiguous reversible behavior with strain up to at least the strain point J, b) Results of $I_c(\epsilon)$ obtained in compressive then tensile strain at 4.0 K and 16 T. I_c degraded fairly linearly and rapidly with compressive strain down to -0.86% , where the irreversible degradation was $\approx 21\%$. Upon releasing compression and increasing strain into tension up to $+0.46\%$ and then back to zero strain, the total I_c irreversible degradation was	

<p>≈41% and (c) shows details of the data highlighted by the blue rectangle in (b). The load–unload experiment revealed that the $I_c(\epsilon)$ behavior is irreversible for any amount of compressive strain applied to the sample. Nonetheless, upon releasing compression and then applying it, $I_c(\epsilon)$ behavior was ‘reversible’ as long as the reapplied compression did not go near or beyond the compressive strain reached before unloading started [68].</p>	27
<p>Figure 1-12: SEM micrograph showing a longitudinal cross section of Bi2212 sample. The heat treatment formed dense Bi2212 grain colonies at the interface with the Ag matrix. A fibrous network of Bi2212 grains formed inside the filament. [68].</p>	29
<p>Figure 2-1: step-by-step fabrication process for manufacturing Ag/Al alloy.</p>	50
<p>Figure 2-2: a) Starting 450 mesh ($d_{90} < 30 \mu\text{m}$) gas atomized Ag/0.50wt%Al powder, b) extruded and cold drawn Ag/0.50wt%Al tubes.</p>	51
<p>Figure 2-3: a) 0.8 mm diameter Bi2212/Ag0.5Al conductor wire, b) an optical image from cross section of fabricated 85 x 7 double restack Bi2212 wire before PMP heat treatment.</p>	53
<p>Figure 2-4: Time-temperature profile for a) a partial melt processing (PMP) used here, b) Split melt processing (SMP) heat treatment applied to single layer coil for leakage studies, and c) Internal oxidation heat treatment for Ag/Al alloys (axes not to scale).</p>	57
<p>Figure 2-5: Room temperature tensile-testing equipment used for Bi2212 RW samples.</p>	62
<p>Figure 2-6: The LabVIEW program used for controlling the RT tensile-testing equipment.</p>	62
<p>Figure 2-7: Schematic of equipment for Bi2212 round wire electrical characterization showing connections between different devices.</p>	65
<p>Figure 3-1: FESEM images of DS Ag/0.50wt%Al alloy (a) before and (b) after PMP heat treatment.</p>	73
<p>Figure 3-2: RT stress/strain behavior of as-rolled Ag/0.20wt%Mg alloy before and after PMP heat treatment.</p>	75
<p>Figure 3-3: RT stress/strain behavior of annealed Ag/0.20wt%Mg, DS Ag/0.50wt%Al and pure Ag sheet alloys before and after PMP heat treatment.</p>	76
<p>Figure 3-4: Stress/strain behavior of three groups of DS Ag/0.50wt%Al solid alloy wires at 4.0 K. One sample was annealed at 375 °C for 20 min; and two other samples, one annealed</p>	

at 375 °C and the other at 850 °C before being partial-melt processed. The results from the latter two overlap on the graph.	80
Figure 3-5: SEM images of fracture surfaces of (a) DS Ag/0.50wt%Al and (b) Ag/0.20wt%Mg alloys after PMP heat treatment. The images show ductile behavior of DS Ag/0.50wt%Al in comparison to brittle fracture of Ag/0.20wt%Mg. Note that the magnifications are not the same; optimum magnifications were chosen in order to best highlight the microstructural features.	83
Figure 3-6: Optical images of Bi2212/Ag0.50Al multifilamentary wire (a) before and (b) after PMP heat treatment.	86
Figure 3-7: Cross-sectional images of Bi2212/Ag0.50Al wire showing grain sizes in the alloy sheath before and after PMP. (a , b) Optical micrographs of etched Bi2212/Ag0.50Al green wire (before PMP), (c , d) optical micrographs of etched Bi2212/Ag0.50Al wire after PMP, (e , f) High magnification SEM images showing the grain structure of DS Ag/0.50wt%Al alloy in the Bi2212/Ag0.50Al wire outer alloy sheath after PMP.	87
Figure 3-8: a) Cross-sectional optical micrograph of Bi2212/Ag0.20Mg wire showing the Ag/0.20wt%Mg alloy sheath grain size after PMP, and b) optical micrograph from the same Ag/0.20wt%Mg outer alloy sheath in an etched sample. The grain size is measured to be about 13-15 μm	89
Figure 3-9: RT stress/strain behavior for Bi2212/Ag0.20Mg and Bi2212/Ag0.50Al wires before and after PMP heat treatment.	90
Figure 3-10: Stress/strain behavior for Bi2212/Ag0.50Al wires at 77 K and 4.0 K after PMP heat treatment.	92
Figure 3-11: Bi2212/Ag0.50Al single layer spirals (a) before and (b) after heat treatment. Spiral I is composed of 10 turns of wire (wire length of 1 m) and Spiral II is composed of 20 turns of wire (wire length of 2 m). Spiral I is heat treated using the partial melt process and Spiral II is heat treated using the split melt process (SMP).	95
Figure 3-12: I_c and n-value for (a) spiral I and (b) spiral II. End to end (ETE) defined in the text.	95

Figure 4-1: Optical micrographs of a) as-atomized Ag/0.50wt%Al powder particles, and the powder annealed under an argon atmosphere at b) 600°C for 45 min, c) 650°C for 45 min, d) 700°C for 45 min, e) 725°C for 45 min, f) 750°C for 45 min and g) 700°C for 4 hours.	102
Figure 4-2: HVN versus oxidation temperature (held for 4 hours) for Ag/Al alloys with and without PMP heat treatment.....	109
Figure 4-3: RT tensile data for Ag/0.50wt%Al solid alloy wires. a) YS and UTS after internal oxidation in pure oxygen, b) YS and UTS post-PMP for internally oxidized alloy wires, c) strength changes for DS Ag/0.50wt%Al alloy wire during PMP, d) a comparison of UTS for internally oxidized alloy wires pre- and post-PMP, and e) a comparison of EI% for internally oxidized alloy wires pre- and post-PMP.....	113
Figure 4-4: SEM images of the grain structure of the Ag/0.50wt%Al alloy after various heat treatments: a) non-oxidized (HVN of 55 and grain size of 3.32 μm), b) internally oxidized at 675°C for 4 hours (HVN of 183 and grain size of 5.72 μm), c) non-oxidized alloy post-PMP (HVN of 160 and grain size of 5.58 μm), and d) oxidized alloy post-PMP (HVN of 174 and grain size of 5.28 μm). Similar results are obtained with the microstructure of the Ag/0.75wt%Al alloy.	114
Figure 4-5: a) Low and b) higher magnification ion channeling contrast micrographs showing the dispersion of nanosize Al_2O_3 precipitates in the Ag matrix for the DS Ag/0.50wt%Al alloy oxidized at 675°C for 4 hours. The dark and light gray color bands/stripes are twins in the Ag matrix. The white and occasionally-black precipitates are Al_2O_3	115
Figure 4-6: Electrical resistivity versus temperature for Ag/0.50wt%Al, Ag/0.75wt%Al and Ag/0.20wt%Mg alloys pre- and post-PMP.....	116
Figure 5-1: Optical micrographs from etched cross-sections of a) Bi2212/Ag0.20Mg, b) Bi2212/Ag0.50Al, c) Bi2212/Ag0.75Al, d) Bi2212/Ag1.00Al, and e) Bi2212/Ag1.25Al green wires.	127
Figure 5-2: SEM micrographs of a) Ag/0.50wt%Al outer alloy sheath in Bi2212/Ag0.50Al, and b) Ag/0.20wt%Mg outer alloy sheath in Bi2212/Ag0.20Mg green wires.	128

Figure 5-3: Optical micrographs from etched cross-section of a) Bi2212/Ag0.50Al, b) Bi2212/Ag0.75Al, c) Bi2212/Ag1.00Al, and d) Bi2212/Ag1.25Al, internally oxidized at 675°C for 4 hours. The grain size for the Ag/Al outer alloy sheathes of these wires is measured to be 11.7, 11.3, 10.5, and 9.7 μm , respectively.	129
Figure 5-4: Optical micrographs from etched cross-section of a) Bi2212/Ag0.50Al, b) Bi2212/Ag0.75Al, c) Bi2212/Ag1.00Al, and d) Bi2212/Ag1.25Al after internal oxidation and PMP heat treatment. The grain size for the Ag/Al outer alloy sheathes of these wires is measured to be 9.7, 9.5, 8.3, and 8.6 μm , respectively.	130
Figure 5-5: Optical micrographs from etched cross-section of a) Bi2212/Ag0.20Mg, b) Bi2212/Ag0.50Al, c) Bi2212/Ag0.75Al, d) Bi2212/Ag1.00Al, and e) Bi2212/Ag1.25Al green wires after PMP. The grain size for the Ag/Al outer alloy sheathes is measured to be 7.6, 7.4, 7.8, and 7.3 μm , respectively. The Ag/0.20wt%Mg outer alloy sheath in Bi2212/Ag0.20Mg has a grain size of ~ 8.2 μm	131
Figure 5-6: HAADF STEM images of the Ag/0.20wt%Mg alloy sheath lifted-out from outer alloy sheath of Bi2212/Ag0.20Mg wire after PMP, a) low magnification, and (b,c) higher magnification micrographs from highlighted box in a.	133
Figure 5-7: HAADF STEM micrographs of the Ag/0.20wt%Mg alloy sheet after PMP heat treatment showing, (a-c) small MgO precipitates dispersed inside the Ag matrix, and d) a higher magnification HAADF STEM image of a single hexagonal shape MgO precipitate having misfit dislocations at its interface with the Ag matrix, (e,f) HRTEM images of Ag/0.20wt%Mg alloy sheet after PMP heat treatment.	134
Figure 5-8: a) EDS maps demonstrate the HAADF STEM image along with the Mg, O, Cu, and Ag chemical distributions of the large MgO precipitates formed on the Ag grain boundaries, b) Combined EDS maps with the HAADF STEM image in Figure 8a.	139
Figure 5-9: a) HAADF STEM image of the dark gray spherical nanosize MgO precipitates formed inside Ag grains of Ag/0.20wt%Mg alloy sheet after PMP, b) EDS map of Mg chemical distribution, c) EDS map of O chemical distribution, and d) EDS map of Ag chemical distribution.	142

Figure 5-10: (a-c) HAADF STEM micrographs of as-received Ag/0.75wt%Al alloy sheet, and d) HRTEM image of as-received Ag/0.75wt%Al alloy sheet showing diffraction contrast of various defects, e.g. stacking faults in the (111) plane of Ag.....	145
Figure 5-11: (a-d) HAADF STEM micrographs of Ag/0.75wt%Al alloy sheet internally oxidized at 675°C for 4 hours, and (e-g) HRTEM images of Ag/0.75wt%Al alloy sheet internally oxidized at 675°C for 4 hours showing diffraction contrast of various defects and misfit strain fields around each precipitate.	146
Figure 5-12: (a,b) HAADF STEM micrographs of Ag/0.75wt%Al alloy sheet internally oxidized at 675°C for 4 hours after PMP, and (c,d) HRTEM images of Ag/0.75wt%Al alloy sheet internally oxidized at 675°C for 4 hours after PMP.....	149
Figure 5-13: a) HAADF STEM micrographs of Ag/0.75wt%Al alloy sheet internally oxidized at 675°C for 4 hours after PMP, b) EDS map of Al chemical distribution, c) EDS map of O chemical distribution, d) EDS map of Ag chemical distribution, e) combined HAADF STEM image and EDS map of Al chemical distribution, and f) combined EDS maps of Ag and Al chemical distributions.	151
Figure 5-14: a) HAADF STEM micrograph of Bi2212 filament interface with Ag matrix in the Bi2212/Ag0.20Mg wire after PMP along with EDS maps of Ag, Cu, O, Mg, Bi, Sr, and Ca chemical distributions.....	156
Figure 5-15: a) EDS line scan showing Cu chemical distribution throughout the entire sample, and b) EDS spectrum acquired only from the Ag matrix showing the amount of Cu diffused out of Bi2212/Ag0.20Mg filament core during PMP.....	159
Figure 5-16: a) HAADF STEM micrograph of Bi2212 filament interface with Ag matrix in the Bi2212/Ag0.75Al wire after PMP along with EDS maps of Ag, Cu, O, Al, Bi, Sr, and Ca chemical distributions.	160
Figure 5-17: a) EDS line scan showing Cu chemical distribution throughout the entire sample, and b) EDS spectrum acquired only from the Ag matrix showing the amount of Cu diffused out of Bi2212/Ag0.75Al filament core during PMP.....	161

CHAPTER 1

Introduction and overview

1.1. General background

1.1.1. Superconductivity discovery and general properties

The electrical resistivity of metals and alloys decreases when they are cooled. The current in a conductor is carried by “conduction electrons” which are free to move through the material. Thermal vibration of atoms and the presence of defects and impurities in the crystal structure of the materials can scatter the moving electrons and give rise to electrical resistance. When the temperature is lowered, the thermal vibration of atoms decreases and the conduction electrons are less scattered. Therefore, the electrical resistance decreases with decreasing temperature.

Superconductivity was initially discovered by Heike Kammerlingh Onnes in Leiden, the Netherlands, in 1911 after liquefaction of Helium in 1908. Onnes measured the resistance of pure mercury and he found that at very low temperatures the resistance becomes imperceptibly small. This was not surprising, but he discovered that the manner in which the resistance disappeared is completely unexpected. Instead of resistance falling smoothly as the temperature was reduced towards 0 K, he found that pure mercury suddenly loses its

resistance to direct current flow when it is cooled below 4.2 K. Within a month, superconductivity was been found in lead and tin as well. Since then, the same phenomenon has been observed in about half of pure elements and hundreds of compounds.

Superconductors are a class of materials which show zero resistance to electrical current when they cooled below their transitions temperature. This is also called critical temperature (T_c) which is different for each material. Superconductivity exists in pure elements, intermetallic alloys and compounds. The zero resistance property is obtained in direct current (dc) applications and a resistance has been observed in alternating current (ac) applications. Figure 1-1 compares the change of electrical resistance for a superconductor and normal material with decreasing temperature. Figure 1-2 shows the history of developing superconducting materials by year.

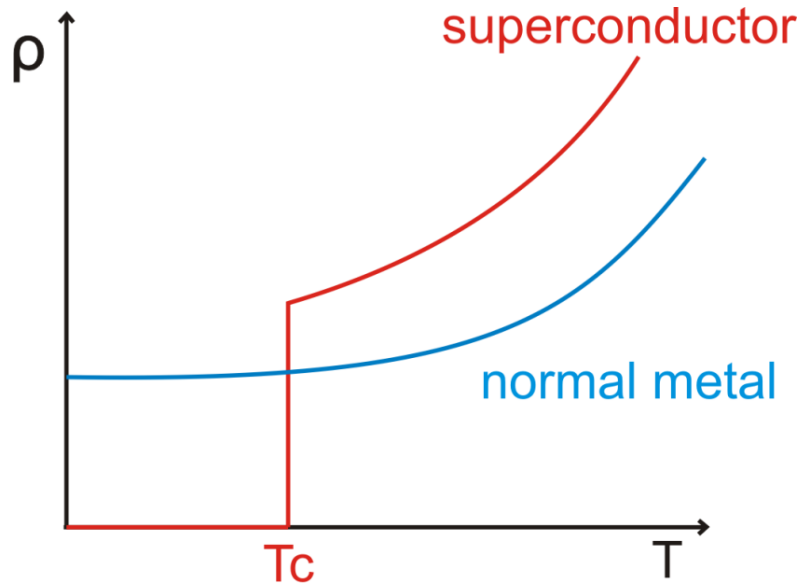


Figure 1-1: Change of electrical resistance with temperature for a superconductor and normal material.

When a material makes the transition from the normal to superconducting state, it actively excludes magnetic fields from its interior; this is called the Meissner effect. The German physicists Walther Meissner and Robert Ochsenfeld discovered the phenomenon in 1933 by measuring the magnetic field distribution outside superconducting tin and lead samples [1]. The samples, in the presence of an applied magnetic field, were cooled below their superconducting transition temperature. Below the transition temperature, the samples cancelled nearly all interior magnetic fields. They detected this effect only indirectly because the magnetic flux is conserved by a superconductor: when the interior field decreases, the exterior field increases. For the first time, they provided a uniquely defining property of the

superconducting state. Figure 1-3 shows a diagram of the Meissner effect. Superconductors in the Meissner state exhibit perfect diamagnetism, meaning that the total magnetic field is almost zero deep inside the body of superconductor material. In Figure 1-3, magnetic field lines, represented as arrows, are excluded from a superconductor when it is cooled below T_c .

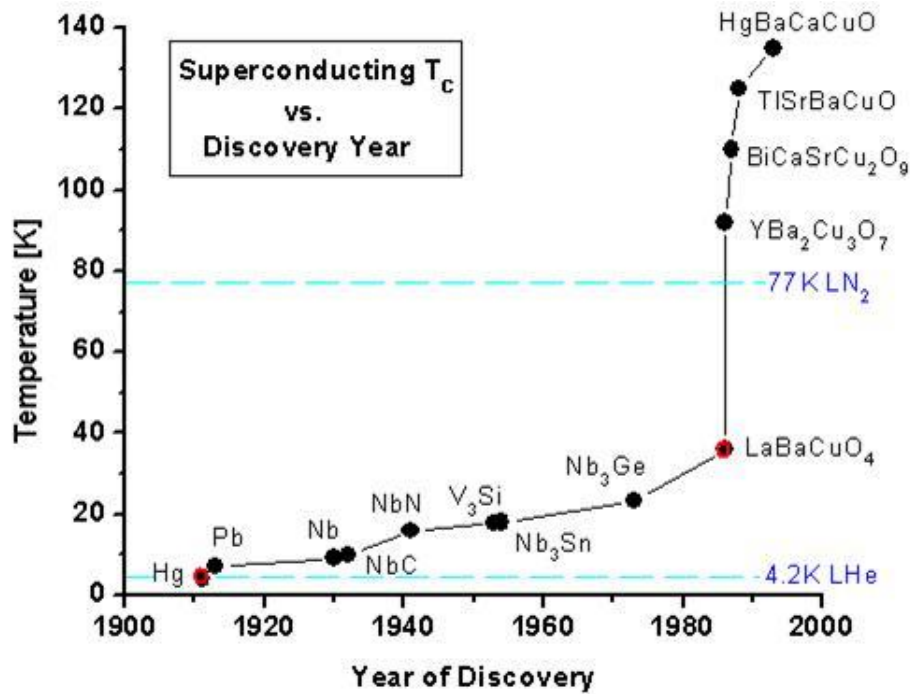


Figure 1-2: History of developing superconducting material by critical temperature.

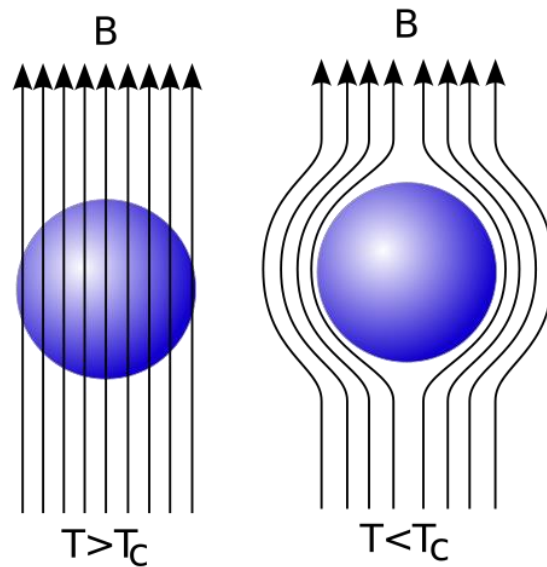


Figure 1-3: Diagram of the Meissner effect. Magnetic field lines, represented as arrows, are excluded from a superconductor body when it is below its critical temperature.

1.1.2. Superconductors classifications

There are several criteria to classify superconductors. I) by their response to a magnetic field: when the applied magnetic field becomes too large, superconductivity breaks down. Superconductors can be divided into two groups of type I and II according to how this breakdown occurs. In type-I superconductors, superconductivity is abruptly destroyed when the strength of the applied field rises above a critical value (H_c). This type of superconductivity is normally exhibited by pure metals, e.g. aluminium, lead, and mercury. In general and with the exception of Nb and V, all elemental superconductors are Type I.

This type of superconductors has a single critical magnetic field (H_c), above which all superconductivity is lost.

Type II superconductor exhibits two lower and upper critical magnetic fields (H_{c1} , H_{c2}). Lower critical field occurs when magnetic field penetrates the material but the material still remains superconducting. When the field becomes too large, the entire material becomes non-superconducting; this corresponds to the higher critical field. Type II superconductors do not show perfect diamagnetism above H_{c1} . These have a mixed state ($H_{c1} < H_c < H_{c2}$) in which magnetic field partially diffuses in the body of superconductor but the superconductivity does not destroy.

II) By their critical temperature, superconducting materials are divided into two groups: low temperature superconductors (LTS) and high temperature superconductors (HTS). With some exceptions like MgB_2 with $T_c=39$ K, in general materials that superconduct when cooled below the boiling point of liquid nitrogen 77 K are LTS while those that are superconducting at or above 77 K are HTS. Some examples of LTS superconductors are NbTi, Nb_3Sn , Nb_3Ge , Nb_3Si , Nb_3Ga , and HTS materials are compounds of bismuth (Bi-Sr-Ca-Cu-O), yttrium or other RE elements (Y-Ba-Cu-O), thallium (Tl-Ba-Ca-Cu-O) and mercury (Hg-Ba-Ca-Cu-O).

1.1.3. Superconducting critical properties

A transition from the superconducting to normal state can occur in three different ways: by increasing the temperature above T_c , by raising the current density above the critical current density (J_c), and by increasing the applied magnetic field above H_c for type I superconductors and above H_{c2} for type II. If these variables occur in combination, a lesser change in their variations can cause the transition. These three variables define a boundary within which the material is in superconducting state and outside of which the material is in the normal resistive state. This boundary is shown in the critical surface diagram Figure 1-4. The values of these critical parameters depend not only on the type of material, but also on its processing history, purity, etc. For application of superconductor materials, the operation temperature, current density and magnetic field should fall well within these boundaries. H_{c1} , H_{c2} and T_c are material intrinsic parameters such as elements and crystal structure, but J_c is mostly affected by microstructure.

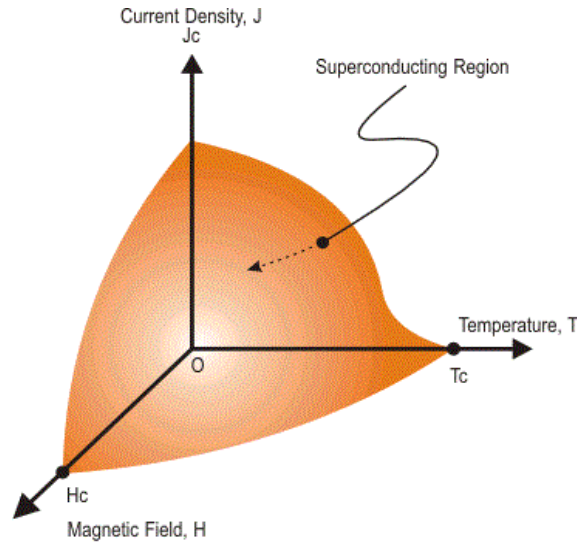


Figure 1-4: Superconducting critical surface, it defines a boundary for operation of superconducting materials.

1.1.4. Applications of superconductor materials

For about 50 years after Onnes' discovery, the applications of superconducting materials made minimal progress. The physics of superconductivity in magnetic fields were misunderstood and technically limiting [2]. In 1961, Kunzler et al. [3] showed that high magnetic field applications of superconductor materials are possible. They reacted tin (Sn) which was drawn inside niobium (Nb) wire to form a brittle intermetallic Nb_3Sn and they were able to reach a current density of $J_c > 10^5 \text{ A/cm}^2$ at 8.8 T and 4.2 K. Since then, application of superconducting materials for magnetic accelerators and magnetic resonance imaging (MRI) were introduced. Most of these applications were based on LTS materials

including NbTi and Nb₃Sn. The main reason MRI has to be superconducting is that power supplies are too noisy. In addition, various power applications were also explored from 1961-1986, but these applications were found to be too complex and expensive compared to the power applications using conductors like copper and aluminum.

In 1986, Bednorz and Muller [4] discovered superconductivity at 30 K in a layered cuprate, Ba-La-Cu-O system with the composition of Ba_xLa_{5-x}Cu₅O_{5(3-y)}. Another discovery happened in 1987, YBa₂Cu₃O_x (YBCO) with T_c at 92 K, well above the liquid nitrogen boiling point (77 K) [5].

Traditionally, LTS materials have been used most commonly in applications that require large magnetic fields, such as MRI devices. Tevatron was the first real large application. It enabled MRI by fostering scale up and quality control of wire manufacturing [6]. The discovery of HTS materials in 1986, however, significantly increased the range of potential applications for superconducting materials in the electric power and electronics industries. Recent advances in superconductivity has focused more on applications of HTS materials, since these are better alternative in terms of efficiency and space utilization compared to conventional conductors.

HTS are available in three material forms including bulk, thin film and wires or tapes. Bulk materials have the potential to generate large magnetic fields. Thin films have the potential

for use in high speed electronics and microwave circuits. Wires and tapes have the potential for use in high current applications including medical diagnostics (MRI magnets), accelerator magnets, high field superconducting magnets, energy and power applications such as transformers, fault current limiters, motors, generators, transmission cables and superconducting magnetic energy storage systems (SMES). In addition, these can be used in low current applications that use resistivity and quantum nature of superconductor materials including superconducting quantum interface device (SQUID) and superconducting filter for cellular phone communications [7-15]. HTS materials are more compact and more efficient replacement for copper technology. In addition, superconductor manufactures are working hard to improve the performance of the superconductor materials in order to meet the requirement for various applications.

1.1.5. Source of stresses in superconducting applications

In most magnet applications, and in particular high field applications, the superconductor materials are subjected to stresses that can reach substantial levels. There are many sources of mechanical loads on the superconductor wires, including stresses due to fabrication, handling, winding, thermal contraction (pre-stresses), stresses due to magnetic field during operation (Lorentz forces) and fault conditions. In most of the applications, there are needs for coil form of superconductor materials. Therefore, during coil fabrication, the superconductor materials are subjected to both bending and uniaxial stresses. To form a coil, the superconductor is being wound and this creates bending stress. In addition, uniaxial

stresses are applied from pre-tensioning of the superconductor during winding process. These types of stresses can be relieved if the conductor is annealed after coil winding.

In the final form, most superconducting materials are in a composite. For multifilamentary Bi2212 round wire (RW) and also tapes, superconducting filaments are encased in a metallic matrix. For coated conductors like YBCO, metallic layers include the substrate, protective cap, and stabilizer that surround the superconducting layer. When a superconductor material is cooled down from its fabrication temperature to operation temperature, various materials within the composite of conductor contract at different rates. This operation temperature can be 77 K or below for HTS and typically 4.2 K for LTS. Thus, due to this mismatch in the thermal contraction, significant stresses are generated on the superconductor materials [13, 16].

When superconducting coils are energized in magnetic field, the Lorentz force acts on the superconductor and this could be quite large, especially for large coils. The hoop stress σ_h on each turn of wire/tape in a coil is given by: $\sigma_h = JBR$, where J is the transport current density, B is the magnetic field strength and R is the radius of the winding.

1.2. $\text{Bi}_2\text{Sr}_2\text{Ca}_1\text{Cu}_2\text{O}_x$ (Bi2212)

1.2.1. Discovery and general properties

$\text{Bi}_2\text{Sr}_2\text{Ca}_{n-1}\text{Cu}_n\text{O}_{2n+4+x}$ (BSCCO) as a new class of superconductor was discovered by Maeda et al. [17] at the National Research Institute for Metals in Japan in 1988. Superconductors in Bi-Sr-Ca-Cu-O system have been attracting great attention due to particular relationship between the structure and the superconductivity characteristics. A series of compounds exist in this system. The best known are $\text{Bi}_2\text{Sr}_2\text{CaCu}_2\text{O}_{8+x}$ (Bi2212) with $n=2$, $\text{Bi}_2\text{Sr}_2\text{CuO}_{6+x}$ (Bi2201) with $n=1$, and $\text{Bi}_2\text{Sr}_2\text{Ca}_2\text{Cu}_3\text{O}_{10+x}$ (Bi2223) with $n=3$. At the time they were unable to determine its precise composition and structure. Almost immediately several groups, and most notably Subramanian et al. [18] at Dupont and Sunshine et al. [19] at AT&T Bell Labs in the same year, identified Bi2212.

Ongoing advances in high energy physics depend on developing high field superconducting magnets capable of producing fields in excess of 20 T. These high field superconducting magnets have the potential to be transformative for a variety of applications, including high field nuclear magnetic resonance, magnets for future high-energy physics accelerators, 20 to 50 T solenoids for muon cooling in a neutrino factory or a muon collider. Figure 1-5 shows the variation of J_c versus applied magnetic field (B (T)) for various superconductor's wires and tapes [20]. Neither NbTi nor Nb_3Sn can provide fields greater than 18 T in dipole magnets or 20-22 T in solenoids, so future devices require HTS materials capable of

generating high magnetic field [21-25]. The potential candidates that may meet this need are $\text{YBa}_2\text{Cu}_3\text{O}_{7-\delta}$ (YBCO) coated conductor tapes and $\text{Bi}_2\text{Sr}_2\text{CaCu}_2\text{O}_{8+x}$ (Bi2212) round wire (RW). YBCO tapes are highly anisotropic, constraining magnet design and adding complexity to its fabrication. Furthermore, options for forming high current cables with YBCO remain limited. Bi2212 is the only HTS material available as an isotropic multifilamentary RW with high J_c , which is preferred for magnets and in particular those requiring cables like Rutherford cable-wound magnets [23-25]. Furthermore, the transport properties of Bi2212 wire continue to improve. As a result of improved compositions and processing techniques, Bi2212 can now be produced as multifilamentary round wire with engineering critical current density (J_e) of 325 A/mm^2 at 4.2 K, 25 T and in long lengths [22]. While further improvements are needed, Bi2212 wire performance is sufficient to evaluate other important factors for high field magnets.

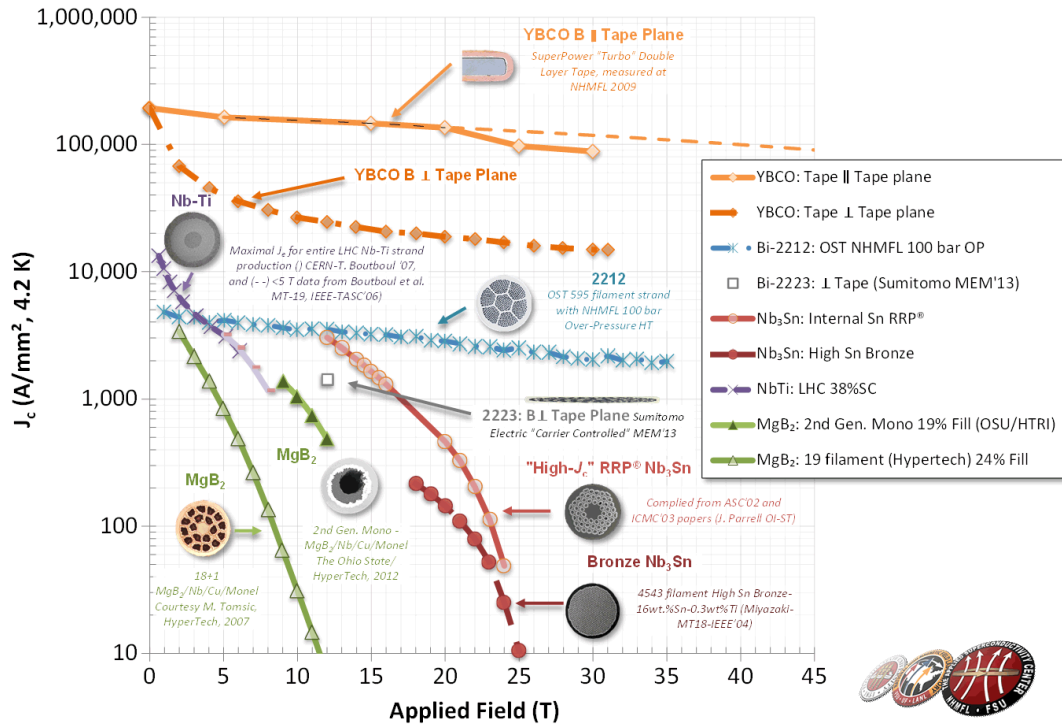


Figure 1-5: Critical current density vs. applied magnetic field [20].

1.2.2. Bi2212 round wire fabrication, heat treatment and microstructure

Bi2212 round wires, made up of multiple filaments, are fabricated using the powder-in-tube (PIT) method in which Bi2212 powder is packed inside Ag tubes and drawn to the desired size. The PIT process consists of powder packing, swaging, drawing, pressing or rolling and thermal treatment. Figure 1-6 shows a schematic diagram of the PIT method to make wires and tapes [26]. In a typical PIT process, the precalcined powders are pressed into round bars

of designed dimensions. The bars are loaded into Ag tubes, and the composites are swaged and drawn to a final diameter of 0.7-1.0 mm.

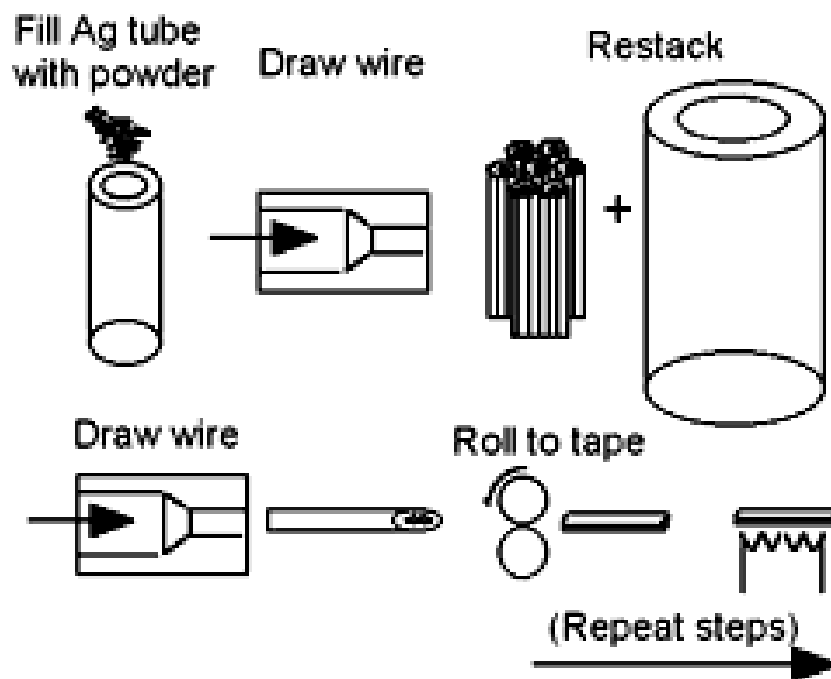


Figure 1-6: Schematic diagram of PIT method to Bi2212 make wires and tapes [26].

After Bi2212 fabrication, the filaments of Bi2212 powder must firstly be melted inside their Ag sheath and then slowly cooled to allow the Bi2212 to reform. Therefore, a partial melt processing (PMP) heat treatment in pure oxygen is required to obtain a well-oriented microstructure, good connectivity between superconducting grains and high J_c [27, 28].

During PMP, Bi2212 wire is heated above the Bi2212 peritectic temperature, around 890°C, decomposing the single phase Bi2212 starting powder into alkaline earth cuprate (AEC) and copper free (CF) phases in addition to liquid. In the subsequent re-solidification, the reverse peritectic reaction reforms the Bi2212 phase in a network of grains and grain colonies with end-to-end connectivity. Due to phase separation in the partial-melt and kinetic limitations of re-solidification, the reverse reaction is not complete; Bi2201 intergrowths and grains form within and beside Bi2212 grains, and AEC and CF phases may remain [29-31]. Figure 1-7 illustrates a time-temperature profile for PMP heat treatment used in this study (not to scale).

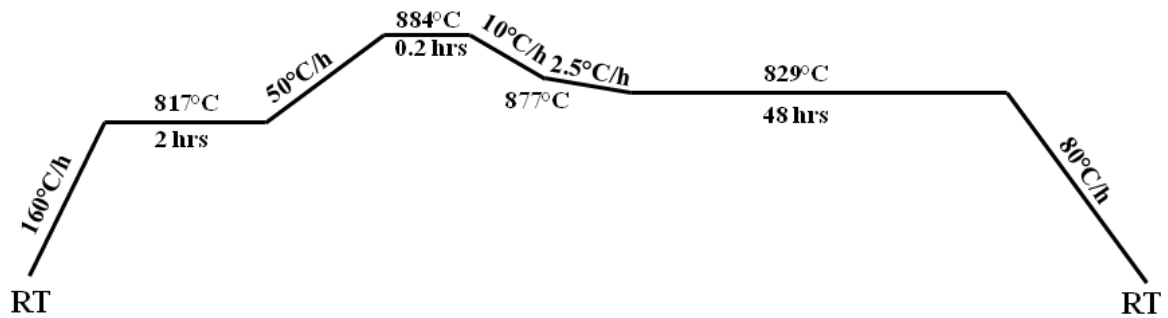


Figure 1-7: Time-temperature profile for partial melt processing used in this study (not to scale).

Recently, there are studies introducing some modified heat treatment profiles for Bi2212 including saw tooth processing [31] and split melt processing [32] which are resulted in

nearly 40% and 120% improvement in the J_c of Bi2212 RWs. Figure 1-8 shows optical micrographs from cross sections of a Bi2212 RW with 0.8 mm diameter before and after PMP heat treatment. Before PMP and in non-reacted condition (known as green wire condition), Bi2212 powders are not connected (Figure 1-8a). After PMP, the Bi2212 superconducting filaments form. The Bi2212 filaments are embedded in pure Ag (inner sheath), while there is an outer sheath made of Ag-alloy (mostly Ag/Mg alloy, see section 2.3.) surrounding the wire (Figure 1-8b).

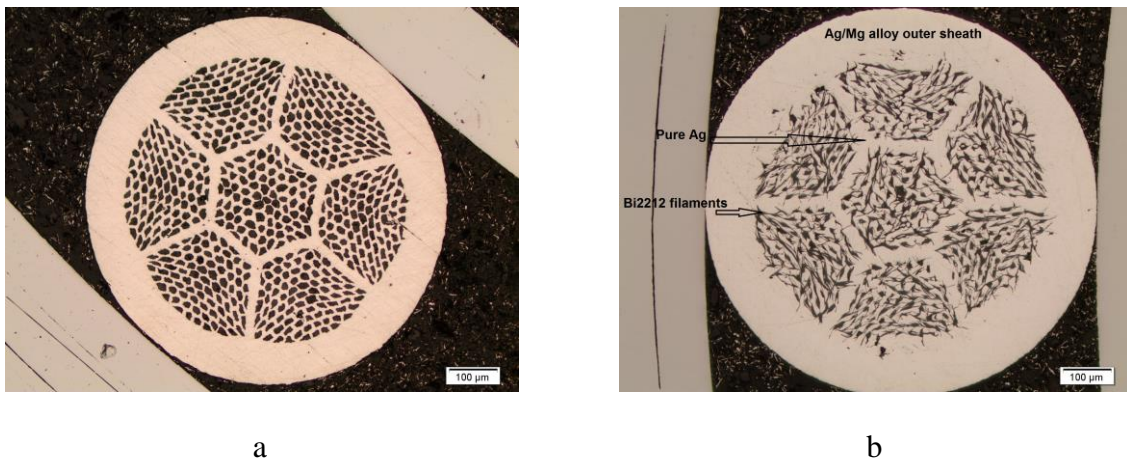


Figure 1-8: Optical micrographs showing cross section of a Bi2212 RW, a) before PMP (green wire), and b) after PMP heat treatment.

1.2.3. Bi2212 sheath materials

High field superconducting magnets not only require high J_c at high magnetic field, but also require sufficient strain tolerance. Bi2212 is a brittle material which exhibits an irreversible reduction in critical current density (J_c) beyond a critical strain value (ϵ_{irr}). For Bi2212 multifilamentary RW, some ductility is obtained from the Ag-alloy sheath which is typically combinations of pure Ag and Ag/Mg alloy. At 4.2 K after full processing, the yield strength of pure Ag is only ~45 MPa and the elastic modulus is ~80 GPa [33]. Thus, alloying is used to obtain a higher strength, higher stiffness sheath material that increases the strain tolerance and strength of Bi2212 wires. As mentioned earlier, in applications, and in particular high field applications, there are many sources of mechanical loads on the wires, including very large Lorentz forces. If the conductor is not adequately supported, the induced strain degrades the conductor critical current (I_c). Thus, a Bi2212 RW with improved strain sensitivity and increased elastic modulus and yield stress, is needed for high magnetic field applications [34-38].

Ag alloys containing a dispersion of oxide particles have been used as sheath materials for high temperature superconductor wires and tapes [39-44]. The sheath materials for Bi2212 wires must satisfy multiple requirements. First, they must be chemically compatible with the Bi2212 oxide phase. They must be stable at ambient temperature and not susceptible to atmospheric oxygen while being permeable to oxygen. They should have good mechanical strength while also having excellent workability for drawing to small wire diameters. Finally,

they must have reasonably high electrical conductivity to serve as stabilizer [28]. High J_c is obtained in Bi2212 wires by partial melt processing in flowing pure oxygen at temperatures up to $\sim 890^\circ\text{C}$. Ag withstands this temperature without oxidizing and is also permeable to oxygen, facilitating oxygenation of Bi2212. Ag is also chemically compatible with the Bi2212 cations. Thus, Ag-alloys are considered options for Bi2212 sheaths.

At present, Ag/0.20wt%Mg is the most commonly used alloy for the outer sheath of Bi2212 RW. MgO precipitates form within the Ag/0.20wt%Mg outer sheath alloy during PMP of Bi2212 in oxygen and strengthens the alloy. Unfortunately, it is believed that Mg is not completely inert to Bi2212. If the Mg content is greater than about 0.3wt%, there is sufficient Mg available to react with Cu that diffuses from the Bi2212 cores into the matrix, forming compounds with MgO, depleting Cu from the Bi2212 cores and reducing J_c [45, 46]. Due to this reactivity, the Ag/0.20wt%Mg alloy is used strictly for the outer sheath to prevent direct contact with the Bi2212 filaments and pure Ag is used for the innermost sheath that interfaces with Bi2212 phase. A practical limit of about 0.2wt%Mg is typically used to reduce reactivity and maintain ductility. Thus, it would be great to have stronger Ag-alloy sheath materials with higher amount of alloying elements for making Bi2212 [45, 47].

1.2.4. Internal oxidation of Ag alloys

Hardening of Ag alloys is predominately accomplished by internally oxidizing solute species such as Mg [39, 41, 42, 47-53], Ni [54-56], Cu [57], Ti [39, 58, 59], Pr [60, 61], Mn [39],

etc., which provide solid solution strengthening [62-65]. Internal oxidation is defined as heating of a dilute $Ag_{100-x}M_x$ alloy under pure oxygen for a specific time and temperature. During internal oxidation, the alloying element oxidizes; forming oxide precipitates which disperse in the matrix and strengthen the alloy [53, 62-67].

The strengthening of metals by internal oxidation was first demonstrated by J.L. Meijering in 1947 [62]. This technique consists of choosing a metal like Ag, Cu, and Ni in which oxygen diffuses rapidly and which has very light affinity to oxygen. One percent or more of a second element such as Mg, Al, Ti, Mn, Cr, Zn, Ni, or Cu for which oxygen has a strong affinity is then added. Since oxygen diffuses much more rapidly than the solute element, a fine stable dispersion of oxide particles is formed, contributing a measurable strength increase to the dispersion-strengthened (DS) Ag alloy [67]. This internal oxidation treatment is a complex process in which several events occur simultaneously: oxygen diffuses in from the environment, the solute diffuses toward the oxygen source, the solute oxidizes to form, first, oxygen rich clusters and, later, discrete oxide precipitates. Each of these events affects the final mechanical properties of the alloy. The resulting microstructure contains a dispersion of hard oxide precipitates in a softer matrix and is called a dispersion-strengthened (DS) alloy.

Dispersion-strengthening is an effective method for producing a metallurgical structure with small grain that is resistant to softening during high temperature heat treatment. Compared to other methods for particle strengthening, such as blending or mixing hard particles with

metal powders, dispersion strengthening produces nanosize oxide precipitates that are distributed homogeneously within the matrix, refine the grain structure and impede dislocation movement. A DS Ag-alloy with nanosize oxide precipitates hardened via internal oxidation could be beneficial for making Bi2212.

1.2.5. Attempts to improve electromechanical properties of Bi2212

The effects of applied stress on the microstructure, mechanical behavior and transport properties of Bi2212 have been extensively studied [43, 44, 68-85]. Sugano et al. [72] investigated the strain dependence of I_c for Bi2212 wires under magnetic fields up to 30 T. Their result at 6 K under 30 T showed that I_c does not change largely up to a tensile strain of 0.50%, at which 95% of I_c compared to its original value is maintained.

Shin et al. [75] attempted to estimate the Young's modulus of the Bi2212 filaments in Bi2212/Ag/Ag composite wire at room temperature by analyzing various stages of the tensile stress-strain curve of Bi2212. Figure 1-9 shows the cross-section of studied Bi2212/Ag/Ag wire and the corresponding measured tensile stress-strain curve of the wire at room temperature. The tensile stress-strain curve was composed of the three stages I, II and III depending on the elastic or plastic behavior of each constituent. Each stage was characterized as follows. In stage I, all constituents (Bi2212 filaments, Ag, Ag alloy) deformed elastically. In stage II, Ag deformed plastically while Bi2212 filaments and Ag alloy elastically. In stage III, Ag and Ag alloy deformed plastically while Bi2212 filaments elastically.

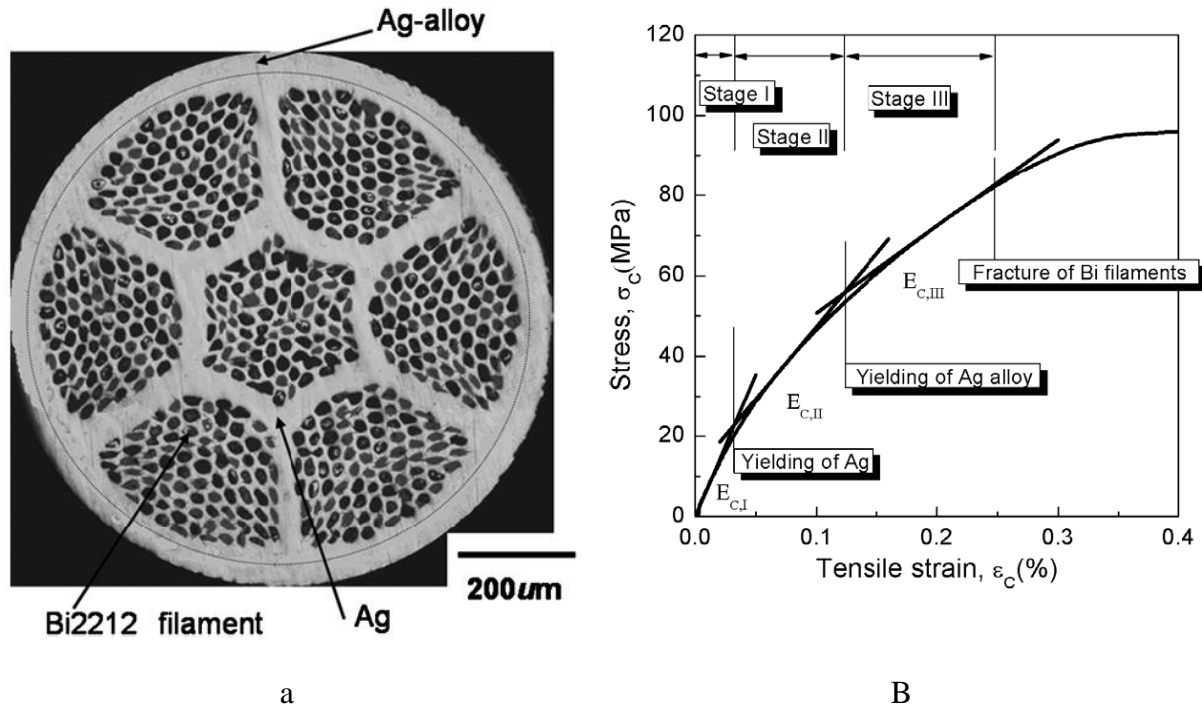


Figure 1-9: a) polished cross-section of Bi2212/Ag/Ag composite wire, and b) measured tensile stress-strain curve of Bi2212 wire at room temperature [75].

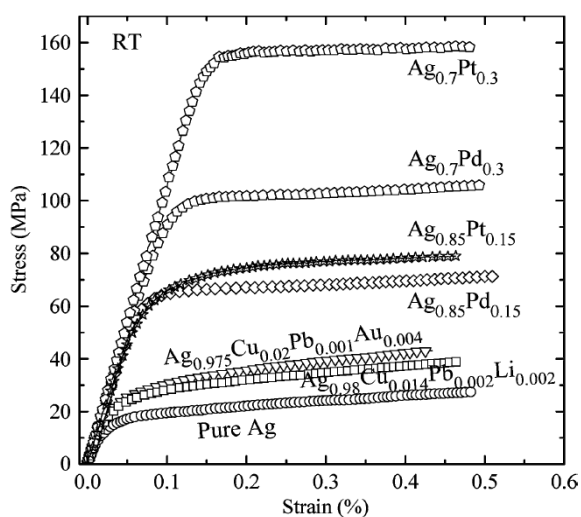
Sotelo et al. [79] studied the electrical, magnetic, and mechanical properties of textured rods of Bi2212 based materials with nominal compositions of $\text{Bi}_2\text{Sr}_2\text{CaCu}_2\text{O}_{8+\delta}$, $\text{Bi}_2\text{Sr}_2\text{CaCu}_2\text{O}_{8+\delta} + 1 \text{ wt\% Ag}$, $\text{Bi}_{1.6}\text{Pb}_{0.4}\text{Sr}_2\text{CaCu}_2\text{O}_{8+\delta}$, and $\text{Bi}_{1.6}\text{Pb}_{0.4}\text{Sr}_2\text{CaCu}_2\text{O}_{8+\delta} + 3 \text{ wt\% Ag}$ which were fabricated using a laser floating zone (LFZ) melting method. Pb doping of Bi2212 samples was shown to degrade the sample microstructure, which leads to a drastic reduction of the superconducting properties. Furthermore, Ag addition improved the microstructure of the Bi2212 and Bi(Pb)2212 samples, reducing the porosity and increasing their mechanical properties, as well as improving the electric and magnetic properties. These effects are

related to the microstructural observations, since Pb doping dramatically reduces the texture while Ag doping improves it.

Mbaruku et al. [70] used a Weibull statistical approach to study the electromechanical behaviors of Bi2212 RW. They showed that Bi2212 RW has significantly different behavior than previously studied Bi2212 tape conductors, with evidence of an underlying mechanically strong but poorly connected electrical ‘backbone’ in the round wire that was not found in the tape conductor. Furthermore, a distribution in the dependence of critical current upon strain ($I_c(\epsilon)$) at the microscopic level was observed for Bi2212 RW, consistent with reports that a complex network of interfilamentary bridges plays a key role in connectivity [78].

Lu et al. [69] measured the uniaxial strain dependence of critical current both in tension and compression for Bi2212 wires. Their measurements showed that I_c significantly degraded starting from a tensile strain of 0.3%–0.4%, and almost immediately under compressive strain. This indicates that the mechanical properties of these Bi2212 wires need to be improved. Measurements of the stress-strain characteristics showed that the yield strength of this Bi2212 wire is only about 107 MPa at room temperature. Hence, there is need to develop strong Ag-alloy materials that could provide a better strengthening of Bi2212 conductors. Figure 1-10a presents stress-strain characteristics measured at room temperature on some newly developed Ag alloy wires and compare them to that of a pure Ag wire and Figure 1-

10b lists the tensile stress-strain curves of heat-treated Ag and Ag alloys measured at room temperature. From the mechanical viewpoint, these alloys may provide good reinforcement for a Bi2212 conductor, and could possibly be incorporated into the inner structure of the wire. They concluded that improved electromechanical properties of Bi2212 wires require the development of stronger sheathing material. It is mentioned that mechanical tests should be ultimately conducted on real Bi2212 wires into which these alloys are incorporated, in order to verify reinforcement efficiency. In addition, chemical compatibility should be studied and cost issues should be considered.



a

	Young's Modulus (GPa)	Yield Strength (MPa)
Ag	70	23
Ag _{0.98} Cu _{0.014} Pb _{0.002} Li _{0.004}	92	33
Ag _{0.975} Cu _{0.02} Pb _{0.001} Au _{0.004}	78	38
Ag _{0.85} Pd _{0.15}	101	68
Ag _{0.85} Pt _{0.15}	94	77
Ag _{0.7} Pd _{0.3}	102	102
Ag _{0.7} Pt _{0.3}	104	153
Ag _{0.9995} Mg _{0.0005}	--	80*

B

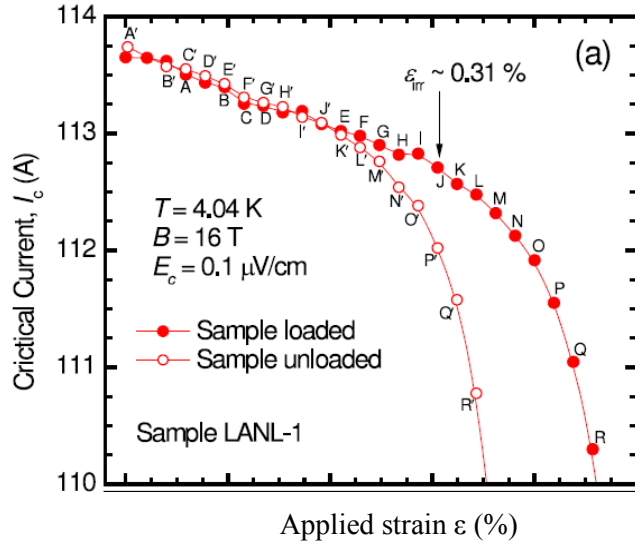
Figure 1-10: a) Tensile stress-strain curves of heat-treated Ag and Ag alloys measured at room temperature, and b) mechanical properties of pure Ag and a selection of Ag alloys at room temperature [69].

Yamazaki et al. [71] attempted to improve the mechanical properties of Bi2212 wire by making stainless steel laminated wires using various thicknesses. The developed tough Bi2212 had a higher hoop force as compared with a YBCO coated superconductor using Hastelloy substrates under the same conditions such as magnetic field, winding diameter and transport current.

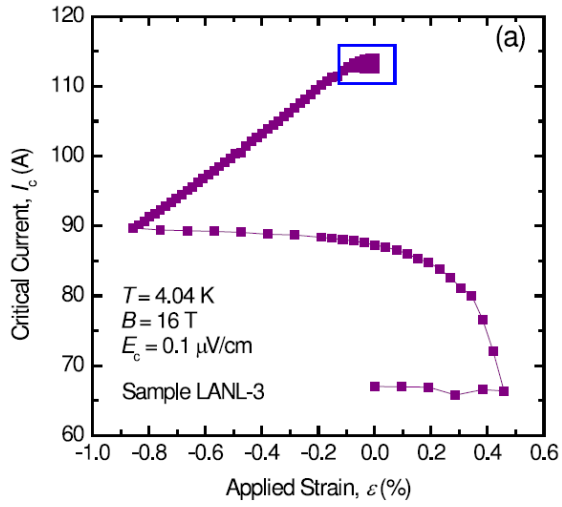
Cheggour et al. [68] found a reversible strain effect on critical current in the tensile regime for Bi2212 wires and developed a modified descriptive strain model that considered the Bi2212 microstructure and its role in tensile and compressive behavior. As seen in Figure 1-11a, the reversible behavior of critical current (I_c) with the applied strain (ϵ) was observed under tension up to 0.31% strain, while no reversibility was observed under axial compressive strain (Figure 1-11b and c). Detailed microstructural studies using scanning electron microscopy revealed that in general there are two “types” of Bi2212 filaments, one mechanically weak and the other mechanically strong. The two-component model postulates that the dense Bi2212 is the strong component and that the porous and fibrous Bi2212 network is the weak component (see Figure 1-12). If the weak component does not contribute to transport current initially, then the Bi2212 wire behavior is reversible. But, if the weak component contributing to transport current initially, then an irreversible behavior was observed until this component fails mechanically due to strain. This study identified the major role that porosity plays in limiting the resilience of the Bi2212 to strain, and anticipated that improved mechanical properties would result from eliminating it. They

concluded that replacing at least part of the Ag sheath with a stronger and compatible alloy to provide a distributed reinforcement across the wire section would be beneficial to I_c .

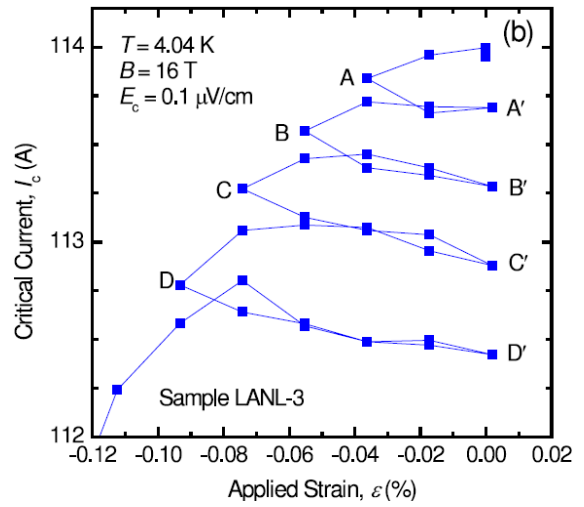
Figure 1-11: a) Results of $I_c(\epsilon)$ for a selection of strain values, obtained in tensile strain at 4.0 K and 16 T. Each pair of unprimed and primed letters indicates a loaded strain point (solid symbol) and its corresponding partially unloaded strain point (empty symbol), respectively. I_c values showed an unambiguous reversible behavior with strain up to at least the strain point J, b) Results of $I_c(\epsilon)$ obtained in compressive then tensile strain at 4.0 K and 16 T. I_c degraded fairly linearly and rapidly with compressive strain down to -0.86% , where the irreversible degradation was $\approx 21\%$. Upon releasing compression and increasing strain into tension up to $+0.46\%$ and then back to zero strain, the total I_c irreversible degradation was $\approx 41\%$ and (c) shows details of the data highlighted by the blue rectangle in (b). The load–unload experiment revealed that the $I_c(\epsilon)$ behavior is irreversible for any amount of compressive strain applied to the sample. Nonetheless, upon releasing compression and then applying it, $I_c(\epsilon)$ behavior was ‘reversible’ as long as the reapplied compression did not go near or beyond the compressive strain reached before unloading started [68].



a



b



c

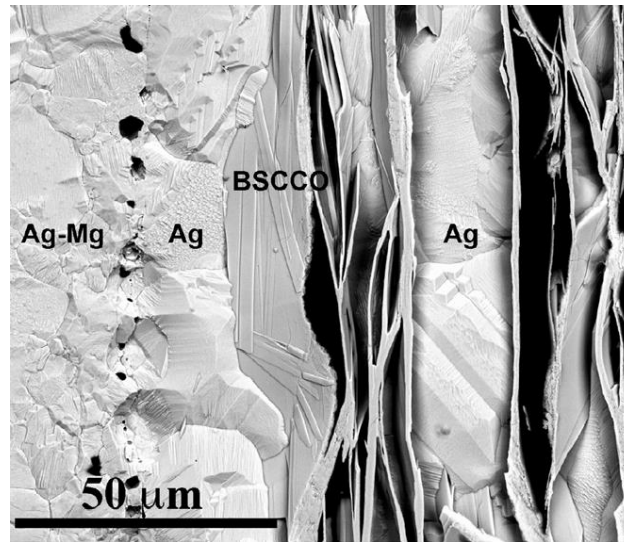


Figure 1-12: SEM micrograph showing a longitudinal cross section of Bi2212 sample. The heat treatment formed dense Bi2212 grain colonies at the interface with the Ag matrix. A fibrous network of Bi2212 grains formed inside the filament. [68].

1.2.6. Attempts on using various sheath alloys for Bi2212

There have been attempts to improve the mechanical properties of Bi2212 by changing the sheath material. Nomura et al. [86] studied the influence of Ag/Au and Ag/Cu alloy substrates on the microstructure and superconducting properties of Bi2212. It was found that the J_c of Bi2212/AgAu was not degraded by increasing the Au content of the Ag/Au alloy, while the J_c of Bi2212/AgCu was drastically degraded by increasing the Cu content of the Ag/Cu alloy. The microstructure of Bi2212 on the Ag/Au alloy was uniform and no precipitates were observed. The J_c degradation of Bi2212 in contact with the Ag/Cu alloy was understood by the fact that Cu absorption of Bi2212 from the Ag/Cu alloys changed the composition of the Bi2212 oxide layer. Parrel et al. [87] investigated the effect of sheath material and deformation method on the oxide core density, filament uniformity, and J_c of $(\text{Bi,Pb})_2\text{Sr}_2\text{Ca}_2\text{Cu}_3\text{O}_x$ tapes. The B2223 tapes were made with pure Ag and oxide dispersion hardened Ag-Mg-Ni alloy sheaths. Samples of these tapes were then heat treated, and deformed between heat treatments either by pressing or rolling. A strong positive correlation between Vickers micro-hardness and J_c was observed. Based on the observed greater micro-hardness values, it is thought that the higher J_c of the pressed tapes is due to a greater oxide core density than is present in the rolled tapes. While the hardened Ag alloy sheath did increase the micro-hardness (bulk density) of the Bi2223 core in the rolled tapes more effectively than the pure Ag sheath, any J_c increase as a result of this higher bulk density appeared to be negated by reactions between the Bi2223 and the Mg and Ni alloying

elements. The degree of transformation from the 2212 to the 2223 phase was always found to be greater in the pressed tapes.

Guo et al. [82] investigated the effects of sheath composition and rolling conditions on the microstructural development and superconducting properties of Bi2212 powder in tube tapes. The best properties were obtained in hot-rolled, Ag (7 at.% Cu) sheathed Bi2212 tapes. These sample had the highest degree of grain alignment, improved sheath and core interfacial uniformity, and significantly higher magnetization and transport critical current densities relative to either cold-rolled Ag(Cu) sheathed or hot- or cold-rolled Ag sheathed Bi2212 tapes. Motowidlo et al. [43, 44, 81] fabricated Bi2212 round wire with various dispersion-strengthened Ag sheath alloys, including Ag/Al. They reported improvements in process control and fabrication that resulted in less porosity and more uniform filaments. The bending strain approached 1% for fabricated Bi2212 wire.

Yoo et al. [88] studied the effects of alloying Au and Mg into Ag for Bi2223 tapes. They found that alloying with Au and Ag increases the resistivity but is not very effective in increasing the hardness. The addition of a small quantity of Mg to Ag/Au and Ag/Pd increases the hardness significantly due to dispersion hardening. Wesolowski et al. [89] studied reactions between Ag sheathed Bi2212 conductors and a variety of oxides. The dominant species that diffused through the Ag sheath was Cu because its solubility in Ag and diffusivity through Ag under Bi2212 melt processing conditions is the highest. Al_2O_3 , CeO_2 ,

SiO₂, Y₂O₃, ZrO₂, CaZrO₃, and SrZrO₃ were identified as non-reactive when heat treated in contact with Bi2212, whereas Fe₂O₃, MgO, and NiO, reacted with Cu that diffused through the Ag during heat treatment.

Nachtrab et al. [54] proposed the use of Ag/Ni composite sheath to improve the mechanical performance of Bi2212. They used a tube made of Ag/Ni composite containing continuous Ni filaments to fabricate a Bi2212 mono-core tape. The Ni filaments oxidized during melt processing in oxygen, showing that Ni is not stable enough to be used in an oxidizing atmosphere in conjunction with Bi2212 oxides. The Ni oxidized and reacted with Cu from the Bi2212 oxide forming a Ni/Cu solid solution oxide phase, and depleting the Cu from the Bi2212 oxide core. The loss of Cu affected the formation of the superconducting Bi2212 phase.

1.3. Objectives of this work

Ag/0.20wt%Mg is the most commonly used alloy for the outer sheath of Bi2212 RW. Ag/0.20wt%Mg alloy demonstrates the advantages of dispersion strengthening by internal oxidation for hardening Ag. MgO precipitates form within the Ag/0.20wt%Mg outer sheath during PMP heat treatment of Bi2212 in pure oxygen and strengthen the Ag/0.20wt%Mg alloy.

Despite the recent successes with Ag/0.20wt%Mg sheathed Bi2212, the use of Ag/0.20wt%Mg for the outer sheath poses some challenges and limitations, including increased difficulty in conductor manufacturing. The alloy has low strength in the unreacted condition and loses ductility rapidly as it is drawn, necessitating frequent anneals. In this condition, the alloy can be extruded and cold drawn to form tubing. During drawing, it work-hardens and loses ductility. Annealing restores ductility, but it must be done in an inert atmosphere or MgO will precipitate on the grain boundaries and embrittle the alloy, making further cold working impossible. It is only during the final heat treatment that it is desirable to form MgO precipitates through internal oxidation. The MgO dispersion formed by internal oxidation is resistant to coarsening and hardens the alloy even after full partial melt processing. In the fully processed condition, the tensile strength of the alloy is approximately four times greater than pure Ag. Most of the MgO precipitates after the Ag has recrystallized and a significant amount of grain growth has occurred [90].

It is desirable to have an alternative high strength and high modulus Ag alloy sheath for Bi2212. The availability of Ag alloys that are compatible with Bi2212 oxide phase is very limited. An Ag alloy must have the following primary characteristics to be useful for making sheath of Bi2212 RW:

1. Good workability for drawing to small wire diameters
2. Oxygen permeability for partial melt heat treatment of Bi2212
3. Chemical compatibility with Bi2212

Among the elements that are typically used to strengthen Ag, precious metals like Au, Pd, and Pt are expensive and elements like Cu, Sn, Sb, and Mn are reactive with Bi2212 phase and reduce J_c . An improved dispersion-strengthened Ag alloy where the alloy is internally oxidized to harden it prior to the Bi2212 conductor fabrication could produce a higher strength conductor after partial melt processing. A potential candidate is the Ag/Al system. Ag/Al alloys have melting and processing characteristics similar to Ag/Mg alloys and have good permeability for oxygen. Furthermore, after Mg, Al has the highest affinity to oxygen based upon free energy [39, 91]. While both Ag/Mg and Ag/Al can be produced in the dispersion-strengthen condition by similar approaches, Al_2O_3 has a higher elastic modulus and lower coefficient of thermal expansion (CTE) than MgO. Additionally, previous research has shown that Al_2O_3 is relatively inert to Bi2212 and does not react strongly with the ceramic fiber used to insulate the conductor [92]. Lastly, Al is inexpensive and readily available [89, 92].

In this work, we report on DS Ag/Al with various compositions as potential candidates for sheathing Bi2212 RW conductor. The fabrication of Ag/Al alloys by powder metallurgy, their internal oxidation heat treatment to form DS Ag/Al alloy (a uniform dispersion of Al_2O_3 precipitates in the Ag matrix), the relationship between microstructure, physical and mechanical properties of the DS Ag/Al alloys are studied in detail. Next, the Ag/Al alloys are used for making Bi2212 round wire. Heat treatment, microstructure, mechanical and electrical properties of Bi2212 wires with Ag/Al sheath alloys having various Al content are

studied to improve the strain sensitivity of Bi2212 wires after PMP. The properties of Ag/Al alloy sheaths and Bi2212/AgAl wires are compared with Ag/0.20wt%Mg alloy sheath and Bi2212/AgMg wire.

1.4. References cited

- [1] W. Meissner and R. Ochsenfeld, "Ein neuer Effekt bei Eintritt der Supraleitfähigkeit," *Naturwissenschaften*, vol. 21, pp. 787-788, 1933/11/01 1933.
- [2] T. Berlincourt, "Type II superconductivity: Quest for understanding," *IEEE Transactions on Magnetics*, vol. 23, pp. 403-412, 1987.
- [3] J. E. Kunzler, *et al.*, "Superconductivity in Nb₃Sn at High Current Density in a Magnetic Field of 88 kgauss," *Physical Review Letters*, vol. 6, pp. 89-91, 1961.
- [4] J. G. Bednorz and K. A. Müller, "Possible highT_c superconductivity in the Ba-La-Cu-O system," *Zeitschrift für Physik B Condensed Matter*, vol. 64, pp. 189-193, 1986/06/01 1986.
- [5] M. K. Wu, *et al.*, "Superconductivity at 93 K in a new mixed-phase Y-Ba-Cu-O compound system at ambient pressure," *Physical Review Letters*, vol. 58, pp. 908-910, 1987.
- [6] (2012). *Energy Frontier: Tevatron*. Available:
<http://www.fnal.gov/pub/science/experiments/energy/tevatron/>
- [7] M. Chen, *et al.*, "High temperature superconductors for power applications," *Journal of the European Ceramic Society*, vol. 24, pp. 1815-1822, 2004.

- [8] W. V. Hassenzuhl, *et al.*, "Electric power applications of superconductivity," *Proceedings of the IEEE*, vol. 92, pp. 1655-1674, 2004.
- [9] S. S. Kalsi, *et al.*, "Development status of rotating machines employing superconducting field windings," *Proceedings of the IEEE*, vol. 92, pp. 1688-1704, 2004.
- [10] R. M. Scanlan, *et al.*, "Superconducting materials for large scale applications," *Proceedings of the IEEE*, vol. 92, pp. 1639-1654, 2004.
- [11] A. P. Malozemoff, *et al.*, "Progress in high temperature superconductor coated conductors and their applications," *Superconductor Science and Technology*, vol. 21, p. 034005, 2008.
- [12] A. P. Malozemoff, *et al.*, "HTS Wire: status and prospects," *Physica C: Superconductivity*, vol. 386, pp. 424-430, 2003.
- [13] D. Larbalestier, *et al.*, "High-T-c superconducting materials for electric power applications," *Nature*, vol. 414, pp. 368-377, Nov 15 2001.
- [14] A. P. Malozemoff, *et al.*, "HTS wire at commercial performance levels," *IEEE Transactions on Applied Superconductivity*, vol. 9, pp. 2469-2473, 1999.
- [15] A. P. Malozemoff, *et al.*, "Power applications of high-temperature superconductors: status and perspectives," *IEEE Transactions on Applied Superconductivity*, vol. 12, pp. 778-781, 2002.
- [16] P. Skov-Hansen, *et al.*, "Stresses and strains in multi-filament HTS tapes," *IEEE Transactions on Applied Superconductivity*, vol. 9, pp. 2617-2620, 1999.

- [17] H. Maeda, *et al.*, "A new high- T_c oxide superconductor without a rare-earth element," *Japanese Journal of Applied Physics Part 2-Letters*, vol. 27, pp. L209-L210, Feb 1988.
- [18] M. A. Subramanian, *et al.*, "A new high-temperature superconductor: $\text{Bi}_2\text{Sr}_{3-x}\text{Ca}_x\text{Cu}_2\text{O}_{8+y}$," *Science*, vol. 239, pp. 1015-1017, February 26, 1988.
- [19] S. A. Sunshine, *et al.*, "Structure and physical properties of single crystals of the 84-K superconductor $\text{Bi}_{2.2}\text{Sr}_2\text{Ca}_{0.8}\text{Cu}_2\text{O}_{8+\delta}$," *Physical Review B*, vol. 38, pp. 893-896, 1988.
- [20] P. J. Lee. A comparison of superconductor critical currents [Online]. Available: <http://fs.magnet.fsu.edu/~lee/plot/plot.htm>
- [21] H. C. Freyhardt and E. E. Hellstrom, "High-Temperature Superconductors: A Review of $\text{YBa}_2\text{Cu}_3\text{O}_{6+x}$ and $(\text{Bi,Pb})_2\text{Sr}_2\text{Ca}_2\text{Cu}_3\text{O}_{10}$," in *Cryogenic Engineering*, K. Timmerhaus and R. Reed, Eds., ed: Springer New York, 2007, pp. 309-339.
- [22] H. Miao, *et al.*, "Development of round multifilament Bi-2212/Ag wires for high field magnet applications," *IEEE Transactions on Applied Superconductivity*, vol. 15, pp. 2554-2557, 2005.
- [23] H. Miao, *et al.*, "High field insert coils from Bi-2212/Ag round wires," *IEEE Transactions on Applied Superconductivity*, vol. 17, pp. 2262-2265, 2007.
- [24] J. Schwartz, *et al.*, "High Field Superconducting Solenoids Via High Temperature Superconductors," *IEEE Transactions on Applied Superconductivity*, vol. 18, pp. 70-81, 2008.

- [25] H. W. Weijers, *et al.*, "High Field Magnets With HTS Conductors," *IEEE Transactions on Applied Superconductivity*, vol. 20, pp. 576-582, 2010.
- [26] L. R. Motowidlo, *et al.*, "Multifilament BPSCCO superconductor: fabrication and heat treatment study," *IEEE Transactions on Applied Superconductivity*, vol. 3, pp. 942-945, 1993.
- [27] J. Kase, *et al.*, "Partial melt growth process of $\text{Bi}_2\text{Sr}_2\text{Ca}_1\text{Cu}_2\text{O}_x$ textured tapes on silver," *Japanese Journal of Applied Physics Part 2-Letters*, vol. 29, pp. L1096-L1099, Jul 1990.
- [28] D. A. Cardwell and D. S. Ginley, *Handbook of Superconducting Materials* vol. I: Institute of Physics 2003.
- [29] X. T. Liu, *et al.*, "Effect of Resolidification Conditions on $\text{Bi}_2\text{Sr}_2\text{Ca}_1\text{Cu}_2\text{O}_x/\text{Ag}/\text{AgMg}$ Coil Performance," *IEEE Transactions on Applied Superconductivity*, vol. 19, pp. 2232-2236, 2009.
- [30] W. T. Nachtrab, *et al.*, "Effect of Solidification Conditions on Partial Melt Processed $\text{Bi}_2\text{Sr}_2\text{Ca}_1\text{Cu}_2\text{O}_x/\text{Ag}$ Round Wire," *IEEE Transactions on Applied Superconductivity*, vol. 21, pp. 2795-2799, 2011.
- [31] G. Naderi, *et al.*, "Understanding processing–microstructure–properties relationships in $\text{Bi}_2\text{Sr}_2\text{Ca}_1\text{Cu}_2\text{O}_x/\text{Ag}$ round wires and enhanced transport through saw-tooth processing," *Superconductor Science and Technology*, vol. 26, p. 105010, 2013.

- [32] T. Shen, *et al.*, "Electromechanical Behavior of $\text{Bi}_2\text{Sr}_2\text{CaCu}_2\text{O}_x$ Conductor Using a Split Melt Process for React-Wind-Sinter Magnet Fabrication," *IEEE Transactions on Applied Superconductivity*, vol. 18, pp. 520-524, 2008.
- [33] D. R. Smith and F. R. Fickett, "Low temperature properties of silver," *Journal of Research of the National Institute of Standards and Technology*, vol. 100, pp. 119-171, Mar-Apr 1995.
- [34] W. P. Chen, *et al.*, "Microstructures and properties of Bi2212/Ag tapes grown in high magnetic fields," *Physica C: Superconductivity*, vol. 324, pp. 172-176, 1999.
- [35] J. K. Shin, *et al.*, "Analysis of the residual strain change of Bi2212, Ag alloy and Ag during the heating and cooling process in Bi2212/Ag/Ag alloy composite wire," *Superconductor Science and Technology*, vol. 21, p. 075018, 2008.
- [36] M. Sugano, *et al.*, "Irreversible behavior of thermal expansion in Bi2212 composite wire at low temperature," *Physica C: Superconductivity*, vol. 445-448, pp. 751-755, 2006.
- [37] A. Villaume, *et al.*, "Self-field redistributions and strain effects observed by magneto-optical imaging in Bi2212 multifilaments," *Physica C: Superconductivity*, vol. 469, pp. 120-125, 2009.
- [38] H. W. Weijers, *et al.*, "Field dependence of the critical current and its relation to the anisotropy of BSCCO conductors and coils," *IEEE Transactions on Applied Superconductivity*, vol. 15, pp. 2558-2561, 2005.

- [39] R. Navarro, "Silver alloys used in composite BSCCO tapes: development of electrical and mechanical properties during manufacture," *Superconductor Science & Technology*, vol. 13, pp. R147-R170, Dec 2000.
- [40] B. C. Prorok, *et al.*, "Hardness and microstructure of internally oxidized silver alloys," *IEEE Transactions on Applied Superconductivity*, vol. 10, pp. 1178-1181, Mar 2000.
- [41] J. Schwartz, *et al.*, "High temperature mechanical properties and high strength sheaths for powder-in-tube tapes," *Applied Superconductivity*, vol. 2, pp. 271-280, 1994.
- [42] J. Tenbrink, *et al.*, "Development of technical high T_c superconductor wires and tapes," *IEEE Transactions on Applied Superconductivity*, vol. 3, pp. 1123-1126, 1993.
- [43] G. B. Galinski, *et al.*, "The Dependence of J_c on bending strain in round multifilament $\text{Bi}_2\text{Sr}_2\text{CaC}_2\text{O}_x$ wires sheathed in Ag and Ag alloys," *Applied Superconductivity* vol. 3, pp. 117-121, 1995.
- [44] G. B. Galinski, *et al.*, "Processing and properties of BSCCO 2212 Ag and Ag alloy multifilament round wires," *Advances in cryogenic engineering* vol. 42B, pp. 617-621, 1997.
- [45] P. Majewski, *et al.*, "Diffusion of Cu into the Ag sheath of BPSCCO tapes," *Physica C: Superconductivity*, vol. 325, pp. 8-12, 1999.
- [46] P. Majewski, *et al.*, "Cu diffusion into Ag during BSCCO tape processing," *Physica C: Superconductivity*, vol. 351, pp. 62-66, 2001.

- [47] B. C. Prorok, *et al.*, "Oxygen diffusion and internal oxidation of Mg in Ag/1.12at.%Mg," *Physica C: Superconductivity*, vol. 370, pp. 31-38, 2002.
- [48] L. Charrin, *et al.*, "Internal oxidation of silver-magnesium and silver-copper alloys," *Journal of thermal analysis*, vol. 14, pp. 89-92, 1978/10/01 1978.
- [49] R. E. Koritala, *et al.*, "Microstructure and mechanical properties of internally oxidized Ag/1.12 at.% Mg," *AIP Conference Proceedings*, vol. 614, pp. 768-776, 2002.
- [50] M. O. Rikel and W. Goldacker, "Kinetics and mechanism of low-temperature internal oxidation of Ag-2 and 4 at.%Mg alloys," *Journal of Materials Research*, vol. 14, pp. 2436-2445, Jun 1999.
- [51] L. Charrin, *et al.*, "Evidence for the formation of substoichiometric species during internal oxidation of Ag-Mg alloys," *Oxidation of Metals*, vol. 40, pp. 483-501, 1993/12/01 1993.
- [52] L. Charrin, *et al.*, "Reactivity at macroscopic, meso and microscopic scale in oxidized silver magnesium alloys," *Scripta Materialia*, vol. 42, pp. 701-709, Mar 2000.
- [53] B. M. Semega, *et al.*, "Evolution of the structure of precipitates during internal oxidation of Ag-0.4 at.% Mg alloy," *Philosophical Magazine A*, vol. 66, pp. 1139-1148, 1992/12/01 1992.
- [54] W. T. Nachtrab, *et al.*, "Reactions Between Bi-2212 and Silver-Nickel Composite Sheath," *IEEE Transactions on Applied Superconductivity*, vol. 17, pp. 3091-3094, 2007.

- [55] Y. Nemoto, *et al.*, "Fabrication of low cost Bi-2212 superconductors using Ag/Ni clad tape," *IEEE Transactions on Applied Superconductivity*, vol. 11, pp. 3246-3251, 2001.
- [56] Y. Shida, *et al.*, "Development of preferential intergranular oxides in nickel-aluminum alloys at high temperatures," *Oxidation of Metals*, vol. 18, pp. 93-113, 1982/10/01 1982.
- [57] B. M. Semega, *et al.*, "Mechanical properties of internally oxidized silver alloys," *Journal of Alloys and Compounds*, vol. 188, pp. 268-271, 1992.
- [58] R. Zeng, *et al.*, "Effect on the phase formation of Bi-2223 in some Ag-alloy sheathed PIT tapes," *Physica C: Superconductivity*, vol. 307, pp. 229-236, 1998.
- [59] T. Kuroda, *et al.*, "Critical current densities of AgCu-sheathed Bi-2212 multifilamentary round wires in long length," *Physica C: Superconductivity*, vol. 357-360, Part 2, pp. 1098-1101, 2001.
- [60] E. Asikuzun, *et al.*, "Vickers hardness measurements and some physical properties of Pr₂O₃ doped Bi-2212 superconductors," *Journal of Materials Science: Materials in Electronics*, vol. 23, pp. 1001-1010, 2012/05/01 2012.
- [61] O. Ozturk, *et al.*, "The effect of Pr addition on superconducting and mechanical properties of Bi-2212 superconductors," *Journal of Materials Science: Materials in Electronics*, vol. 23, pp. 511-519, 2012/02/01 2012.
- [62] J. L. Meijering and M. J. Druyvesteyn, "Hardening of Metals by Internal Oxidation," *Philips Research Reports*, vol. 2, pp. 81-102, 1947.

- [63] J. L. Meijering, "Internal Oxidation and Related Phenomena in Alloys," *Angewandte Chemie International Edition in English*, vol. 8, pp. 775-775, 1969.
- [64] J. L. Meijering, "Internal Oxidation in Alloys," *Advances in Materials Research*, vol. 5, pp. 1-82, 1971.
- [65] A. Combe and J. Cabane, "Mechanism of internal oxidation in silver alloys," *Oxidation of Metals*, vol. 21, pp. 21-37, 1984/02/01 1984.
- [66] M. J. Marcinkowski and D. F. Wriedt, "The Effect of internal oxidation on the plastic deformation of silver-aluminum single crystals," *Journal of the Electrochemical Society*, vol. 111, pp. 92-100, 1964.
- [67] J. Takada, *et al.*, "Internal oxidation of dilute silver alloys," *Oxidation of Metals*, vol. 37, pp. 13-22, 1992.
- [68] N. Cheggour, *et al.*, "Reversible effect of strain on transport critical current in $\text{Bi}_2\text{Sr}_2\text{CaCu}_2\text{O}_{8+x}$ superconducting wires: a modified descriptive strain model," *Superconductor Science and Technology*, vol. 25, p. 015001, 2012.
- [69] X. F. Lu, *et al.*, "Electromechanical Characterization of Bi-2212 Strands," *IEEE Transactions on Applied Superconductivity*, vol. 21, pp. 3086-3089, 2011.
- [70] A. L. Mbaruku, *et al.*, "Weibull analysis of the electromechanical behavior of AgMg sheathed $\text{Bi}_2\text{Sr}_2\text{CaCu}_2\text{O}_{8+x}$ round wires and $\text{YBa}_2\text{Cu}_3\text{O}_{7-\delta}$ coated conductors," *Superconductor Science and Technology*, vol. 23, p. 115014, 2010.
- [71] K. Yamazaki, *et al.*, "Recent progress on improvement to mechanical properties of DI-BSCCO wire," *Superconductor Science and Technology*, vol. 25, p. 054015, 2012.

- [72] M. Sugano, *et al.*, "Strain Dependence of Critical Current in Bi2212 W and R Wires Under Magnetic Field Up to 30 T," *IEEE Transactions on Applied Superconductivity*, vol. 16, pp. 1039-1042, 2006.
- [73] S. L. Bray, *et al.*, "Transverse compressive stress effects on the critical current of Bi-2223/Ag tapes reinforced with pure Ag and oxide-dispersion-strengthened Ag," *Journal of Applied Physics*, vol. 88, pp. 1178-1180, 2000.
- [74] M. F. Imayev, *et al.*, "Microstructure, texture and superconducting properties of Bi2212 ceramics, deformed by torsion under pressure," *Physica C: Superconductivity*, vol. 467, pp. 14-26, 2007.
- [75] J. K. Shin, *et al.*, "Estimation of Young's modulus, residual strain and intrinsic fracture strain of Bi2212 filaments in Bi2212/Ag/Ag alloy composite wire," *Physica C: Superconductivity*, vol. 468, pp. 1792-1795, 2008.
- [76] H. W. Weijers, *et al.*, "Bi-based HTS insert coils at high stress levels," *Physica C: Superconductivity*, vol. 372-376, Part 3, pp. 1364-1367, 2002.
- [77] H. W. Weijers, *et al.*, "Bi-Sr-Ca-Cu-O conductors and magnets at high stress-strain levels," *Physica C: Superconductivity*, vol. 357-360, Part 2, pp. 1160-1164, 2001.
- [78] T. Shen, *et al.*, "Filament to filament bridging and its influence on developing high critical current density in multifilamentary Bi₂Sr₂CaCu₂O_x round wires," *Superconductor Science and Technology*, vol. 23, p. 025009, 2010.

- [79] A. Sotelo, *et al.*, "The influence of Pb and Ag doping on the $J_c(H, T)$ dependence and the mechanical properties of Bi-2212 textured rods," *Superconductor Science and Technology*, vol. 22, p. 034012, 2009.
- [80] R. Wesche, *et al.*, "Axial and bending strain effects in Ag and AgNiMg/Bi-2212 wires," *Cryogenics*, vol. 36, pp. 419-426, 1996.
- [81] L. R. Motowidlo, *et al.*, "Recent progress in high-temperature superconductors at Intermagnetics General Corporation," *Physica C: Superconductivity*, vol. 335, pp. 44-50, 2000.
- [82] J. Guo, *et al.*, "Properties and chemical stability of hot-rolled Ag(7 at. % Cu)-sheathed $\text{Bi}_2\text{Sr}_2\text{Ca}_{0.64}\text{Cu}_{1.64}\text{O}_x$ powder-in-tube tapes," *Journal of Applied Physics*, vol. 78, pp. 4596-4607, 1995.
- [83] K. Katagiri, *et al.*, "Stress/strain dependence of critical current in Cu-Ag externally reinforced Ag-Zr/Bi-2212 superconducting tapes," *Cryogenics*, vol. 39, pp. 453-458, 1999.
- [84] J. Kessler, *et al.*, "Preparation of dispersion-hardened single- and multifilamentary $\text{Bi}_2\text{Sr}_2\text{CaCu}_2\text{O}_x$ tapes and wires," *IEEE Transactions on Applied Superconductivity*, vol. 7, pp. 1560-1563, 1997.
- [85] X. F. Lu, *et al.*, "Correlation Between Pressure Dependence of Critical Temperature and the Reversible Strain Effect on the Critical Current and Pinning Force in $\text{Bi}_2\text{Sr}_2\text{CaCu}_2\text{O}_{8-x}$ Wires," *IEEE Transactions on Applied Superconductivity*, vol. 22, pp. 8400307-8400307, 2012.

- [86] K. Nomura, *et al.*, "Influence of Ag-Au and Ag-Cu alloys on $\text{Bi}_2\text{Sr}_2\text{CaCu}_2\text{O}_x$ superconductor," *Applied Physics Letters*, vol. 64, pp. 112-114, 1994.
- [87] J. A. Parrell, *et al.*, "The effect of sheath material and deformation method on the oxide core density, filament uniformity, and critical current density of $(\text{Bi,Pb})_2\text{Sr}_2\text{Ca}_2\text{Cu}_3\text{O}_x$ tapes " *Advances in cryogenic engineering*, vol. 40, pp. 193-200, 1994.
- [88] J. Yoo, *et al.*, "Effect of Au and Mg addition to Ag sheath on microstructure and superconducting properties of BSCCO-2223 tapes," *Physica C: Superconductivity*, vol. 269, pp. 109-114, 1996.
- [89] D. E. Wesolowski, *et al.*, "Reactions between oxides and Ag-sheathed $\text{Bi}_2\text{Sr}_2\text{CaCu}_2\text{O}_x$ conductors," *Superconductor Science and Technology*, vol. 18, p. 934, 2005.
- [90] W. T. Nachtrab and P. R. Roberts, "A Review of Powder Metal-Extrusion Technology," *Advances in Powder Metallurgy & Particulate Materials - 1992, Vol 4*, pp. 321-335, 1992.
- [91] J. D. Gilchrist, *Extraction Metallurgy*, 3rd Edition ed.: Oxford: Pergamon, 1989.
- [92] W. T. Nachtrab, *et al.*, "Effects of Insulation Materials on J_c of Ag and AgMg Sheath Bi_{2212} Wire," in *ICMC2009*, Tuscan, Arizona, 2009, pp. 308-316.

CHAPTER 2

Experimental procedure

2.1. Sample fabrication

The overall goal of the study is to make high strength dispersion-strengthened (DS) Ag/Al alloy for making Bi2212/Ag/AgAl round wire (RW) conductor that has higher strain sensitivity and is more resistant to deformation in high magnetic fields. Microstructure, mechanical, and electrical properties of the fabricated DS Ag/Al alloys and Bi2212/Ag/AgAl wires are measured and compared to an Ag/0.2wt%Mg (Ag/Mg) alloy and a Bi2212/Ag/AgMg RW conductor. All alloys and conductors are made by Supercon Inc., Shrewsbury, Massachusetts, MA.

2.1.1. Pure silver

Pure Ag wire with 1.0 mm diameter and Ag sheet with 0.18-0.28 mm thickness are used as a base material for alloys mechanical behavior comparison. Pure Ag wire and sheet are tested in as-rolled and annealed conditions. Annealing is performed at 375 and 850°C for 20 min in pure Ar atmosphere.

2.1.2. Ag/Al alloy

Ag/Al alloys with various Al content (0.50, 0.75, 1.00, and 1.25 wt%) are made via powder metallurgy and hardened via an internal oxidation heat treatment in oxygen to make dispersion-strengthened (DS) Ag/Al. Powder metallurgy is the most effective method for producing high strength DS alloys that can be cold worked in the fully hardened condition. Powder metallurgy processing promotes a uniform precipitate distribution and fine grain size, both of which contribute to the combination of high strength with good workability. This is a fundamentally different approach than is used to produce Ag/0.2wt%Mg alloy, which is produced from an ingot and is the most common used alloy for the outer sheath of Bi2212 conductor. Ag/0.20wt%Mg is made as a solid solution alloy which cannot be heat treated in oxygen to strengthen it until it is in the final form. In the fabrication process, the Ag/Al metal powder is created by induction melting and inert gas atomization to a mesh size of ~450 (30 μm). Particle size distribution measurements are performed using a Microtrac-X100. As-atomized Ag/Al powder is then annealed under an argon atmosphere at 600, 650, 700, 725 and 750°C for 45 min to find the suitable annealing temperature for creating single grain Ag/Al powder. Annealing at 700°C for 4 hours under an argon atmosphere is finally chosen and is performed for all fabricated Ag/Al powders. Note that each powder particle is initially polycrystalline and is converted to a single-grain powder during annealing. Grain boundaries are preferential sites for oxide precipitation. Grain boundary oxides tend to be larger than oxide particles precipitated homogeneously within the grains. These larger grain boundary oxides coarsen rapidly during PMP heat treatment, destabilizing the oxide particle

distribution and causing a loss of strength. Additionally, coarse grain boundary oxides reduce overall ductility and make the alloy more difficult to process. The annealed Ag/Al powder is then inserted into Cu extrusion cans which are evacuated, sealed and hot extruded at 650°C. Next, the Cu can is removed from the Ag/Al rod by etching with a ferric chloride solution. The extruded Ag/Al rods are then sintered and annealed at 820°C, then cold drawn into 0.8 mm Ag/Al solid alloy wires. Ag/Al alloy sheet is made by rolling the wire to a thickness of 0.20-0.28 mm. Figure 2-1 shows the step-by-step fabrication process for creating the Ag/Al alloy. Figure 2-2a shows the starting gas-atomized Ag/Al powder, and a sample of final extruded and cold drawn Ag/Al tube is shown in Figure 2.2b.

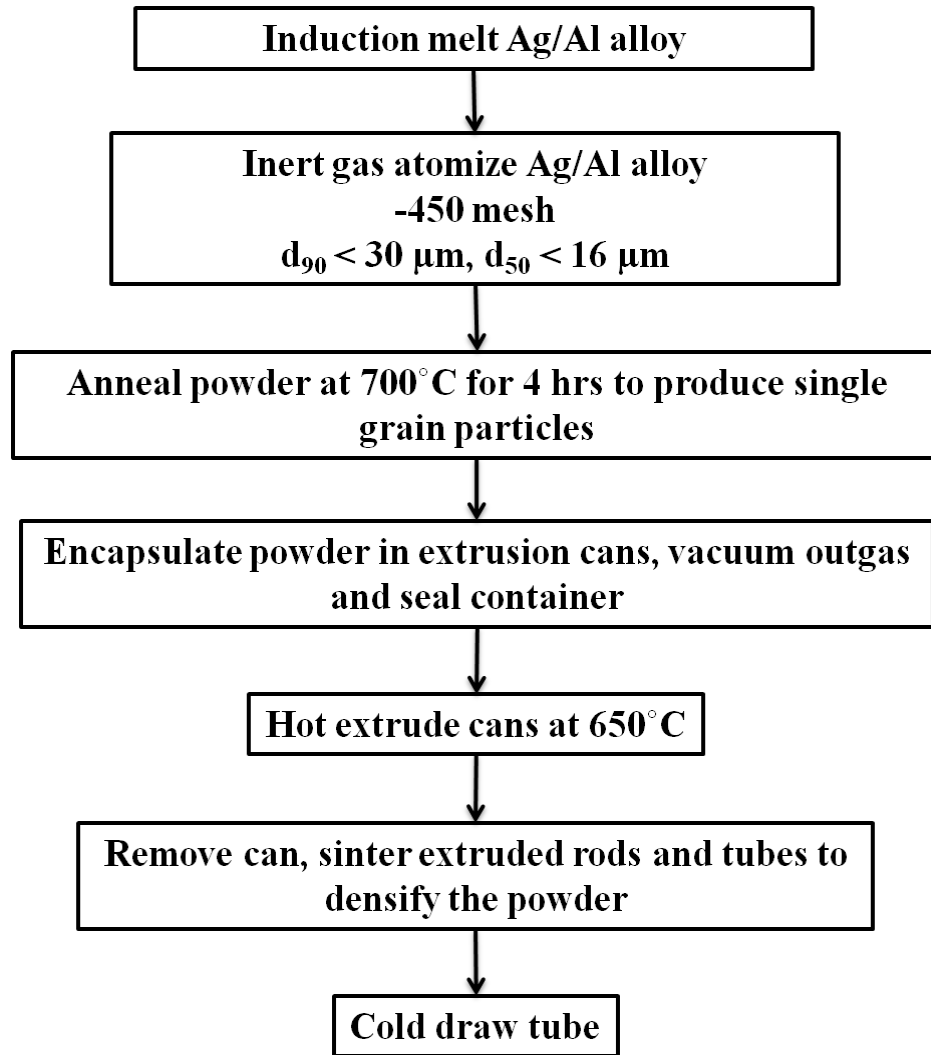


Figure 2-1: step-by-step fabrication process for manufacturing Ag/Al alloy.

2.1.3. Ag/0.20wt%Mg alloy (Ag/Mg)

The Ag/Al alloys are compared with commercial Ag/0.20wt%Mg alloy that is purchased as a tube (Tanaka Kikinzoku, Japan). This alloy is made by conventional ingot metallurgy and

supplied in non-hardened, mill-annealed condition. All annealing is done in pure Ar to avoid oxidation. During fabrication, Ag/0.20wt%Mg sheet is made by flattening a tube (19 mm OD x 17.5 mm ID, 0.75 mm wall) and rolling the 0.75 mm flattened piece. The Ag/0.20wt%Mg alloy sheets have final thickness in the range of 0.18-0.28 mm.

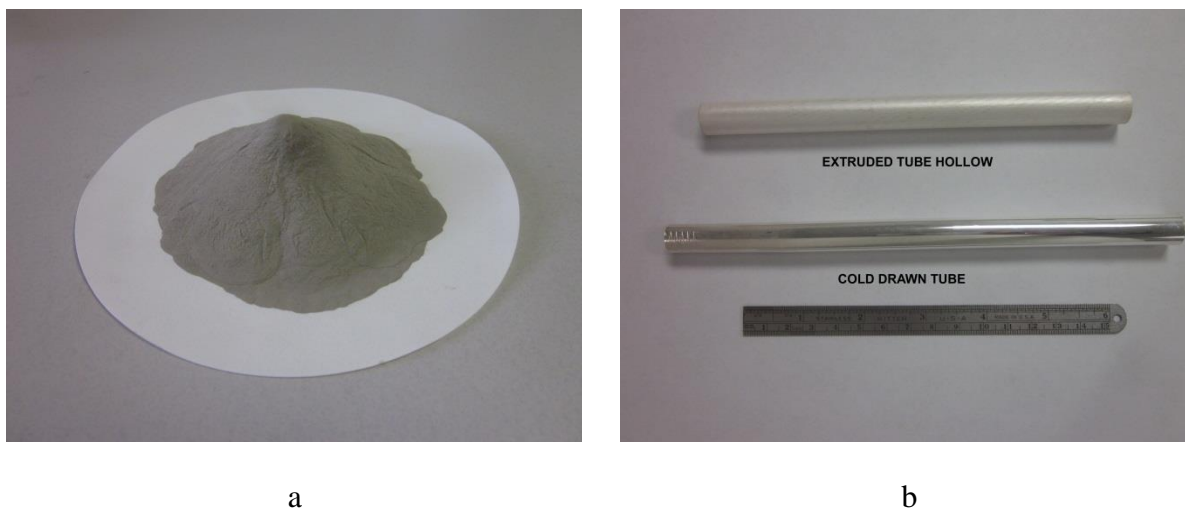


Figure 2-2: a) Starting 450 mesh ($d_{90} < 30 \mu\text{m}$) gas atomized Ag/0.50wt%Al powder, b) extruded and cold drawn Ag/0.50wt%Al tubes.

2.1.4. Bi2212 conductor

The double restack multifilamentary Bi2212 wires are made by powder in tube (PIT) method. The primary and innermost restack bundling tube is pure Ag for all conductors. Ag is permeable to oxygen and is not reactive with the Bi2212 oxide core material.

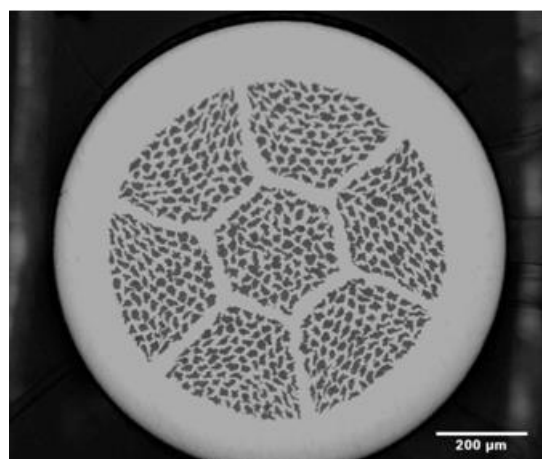
Ag/0.20wt%Mg and Ag/Al alloys with various Al content are used as the outer sheath alloy material. Nexans Bi2212 powder precursor, with a composition of 2.17 Bi, 1.94 Sr, 0.90 Ca, 1.98 Cu and 100 ppm C ($\text{Bi}_{2.17}\text{Sr}_{1.94}\text{Ca}_{0.88}\text{Cu}_{1.98}\text{O}_x$), is used. Table 2-1 lists the specification of all Bi2212 wires used in this study. During the PIT process for making multifilamentary Bi2212 wire, the initial Ag tube is filled with Bi2212 powder, then extruded or drawn to a wire with 1-2 mm diameter. Next, the wire is drawn in a hexagonal shape, cut into shorter lengths, and formed into a stack of 7, 19, 37, 55, 61, 85, or higher numbers of filaments. This stack is then inserted in Ag/0.2wt%Mg and/or Ag/Al alloy tube, and the composite is extruded or drawn to form the final wire. All the Bi2212 conductors in this study are double restack with 85 x 7 design having final diameter of 0.8 mm. Figure 2-3a shows a Bi2212/Ag0.5Al conductor wire coated with 72% Al_2O_3 , 28% SiO_2 ceramic fiber insulation braided onto the wire. Figure 2-3b is an optical image from the cross section of fabricated Bi2212 wire before heat treatment.

Table 2-1: Bi2212 wires specifications used in this study

Conductor's Geometry	Inner sheath	Outer sheath	Average Filament size (μm)	SC fill factor (%)
Bi2212/Ag/AgMg	Pure Ag	Ag/0.20wt%Mg	16.0 \pm 2	25.5 \pm 1
Bi2212/Ag/Ag0.50Al	Pure Ag	Ag/0.50wt%Al	16.5 \pm 2	22.5 \pm 1
Bi2212/Ag/Ag0.75Al	Pure Ag	Ag/0.75wt%Al	16.3 \pm 2	21.5 \pm 2
Bi2212/Ag/Ag1.00Al	Pure Ag	Ag/1.00wt%Al	16.4 \pm 2	23.5 \pm 1
Bi2212/Ag/Ag1.25Al	Pure Ag	Ag/1.25wt%Al	16.0 \pm 2	22.5 \pm 1



a



b

Figure 2-3: a) 0.8 mm diameter Bi2212/Ag0.5Al conductor wire, b) an optical image from cross section of fabricated 85 x 7 double restack Bi2212 wire before PMP heat treatment.

2.2. Heat treatment

2.2.1. Annealing

All Ag/Al and Ag/0.20wt%Mg solid alloy wires and sheets and Bi2212 wires are annealed at 375°C for 20 min in pure Ar after fabrication.

2.2.2. Internal oxidation

The internal oxidation step is the most critical step in the process of making the DS Ag/Al alloy. Internal oxidation heat treatment is performed using two different methods: For the first method, after annealing of as-atomized powder, an Ag/0.50wt%Al metal powder is placed in a tray and heated at 675°C for 24 hours in the flow of 100% oxygen. Ideally, the powder particles should be uniformly exposed to the oxygen atmosphere during the internal oxidation treatment. An oxygen flow over the top of the Ag/Al powder likely results in an O₂ gradient through the powder bed and this may not be an ideal oxidation technique. Next, this oxidized Ag/0.50wt%Al powder is used for making the DS Ag/0.50wt%Al alloy sheets and wires with the steps described in section 2.1.2. In the second method, the non-oxidized Ag/Al alloy powders with various 0.50, 0.75, 1.00 and 1.25 wt% Al content are used to make the Ag/Al solid alloy sheets and wires. These Ag/Al solid alloy sheets and wires are then internally oxidized at 600, 650, 675, 700, 725, 750, 800 and 900 °C for 1, 2, 4 and 8 hours in pure oxygen to form DS Ag/Al alloys. During internal oxidation, heating and cooling are performed under an argon atmosphere; all oxidation procedures are isothermal. Two of the

alloy compositions, Ag/0.50wt%Al and Ag/0.75wt%Al, are also heat treated in pure argon at 675°C for 4 hours for subsequent microstructural studies.

2.2.3. Melt processing of Bi2212

The Bi2212 wires are heat treated using the standard partial melt processing (PMP) heat treatment with temperatures selected based on a previous optimization of Bi2212/AgMg wire manufactured with the same batch of Bi2212 powder. Heat treatments are performed on 5-6 cm long wires in 1 bar flowing oxygen in a quartz tube within a horizontal tube furnace instrumented with R-type thermocouples monitored with programmable controllers. A monitoring thermocouple is placed close to the samples and the temperature-time data are recorded every 30 s using LabVIEW program. The temperature variation is controlled within 0.5°C of the set value. Temperature-time details of the internal oxidation and PMP heat treatment are presented in Figure 2-4a and c (axes not to scale). This PMP heat treatment is applied to all Bi2212 conductors. Furthermore, microstructure, mechanical and electrical behavior of the Ag/Al and Ag/0.20wt%Mg solid alloy sheets and wires are also tested before and after a PMP heat treatment.

For the coil studies and in order to investigate the effect of heat treatment, a Split melt processing (SMP) heat treatment is applied to single layer spiral tested for leakage observation. The SMP temperature-time profile is also selected based on a previous

optimization of Bi2212/AgMg wire manufactured with the same batch of Bi2212 powder (Figure 2-4b).

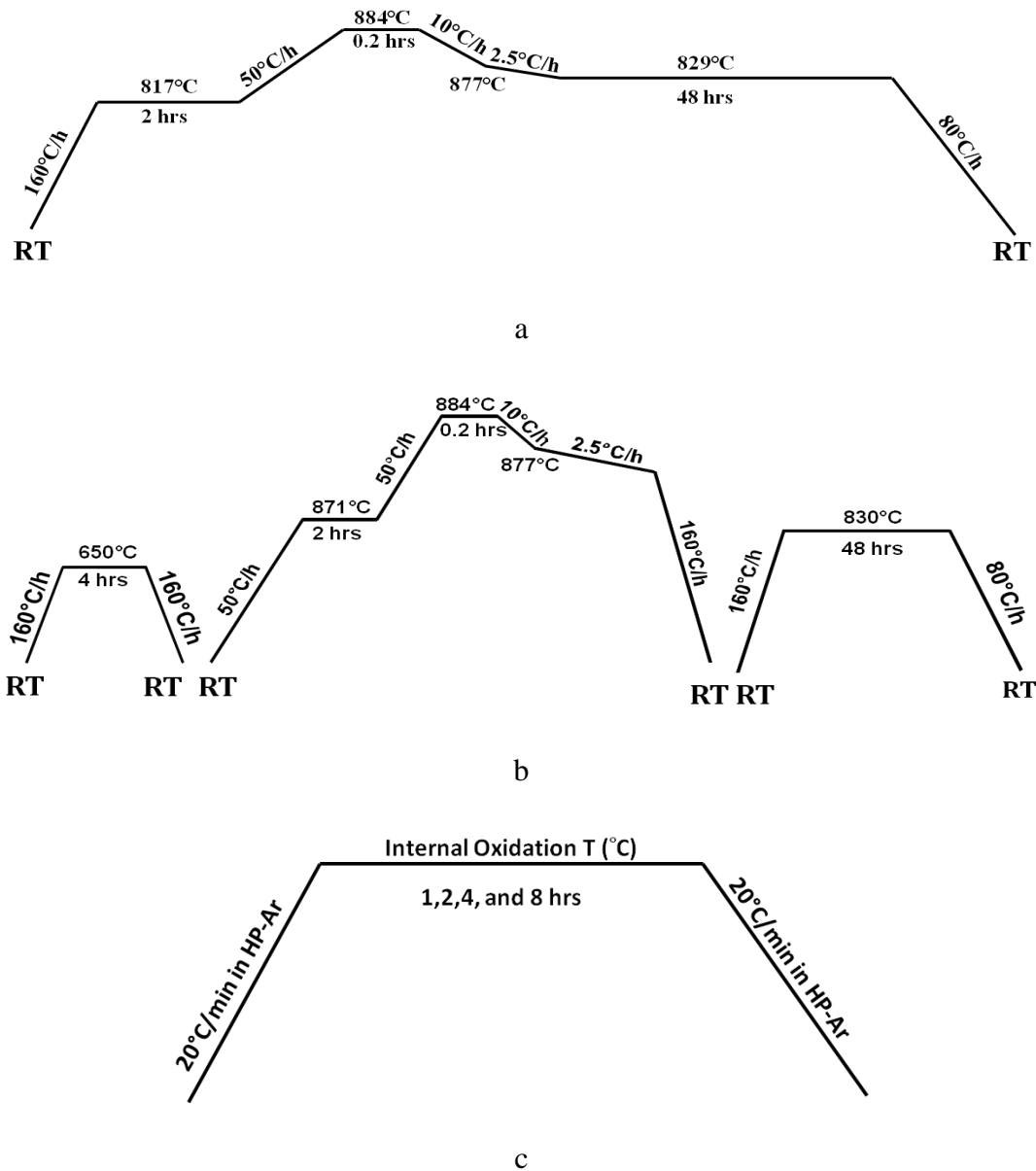


Figure 2-4: Time-temperature profile for a) a partial melt processing (PMP) used here, b) Split melt processing (SMP) heat treatment applied to single layer coil for leakage studies, and c) Internal oxidation heat treatment for Ag/Al alloys (axes not to scale).

2.3. Characterization

2.3.1. Microstructure

2.3.1.1. Optical imaging

Alloys and conductors microstructure is studied using an optical microscope (Olympus SC30). A mixed solution of 50 ml distilled water (H_2O), 20 ml ammonium hydroxide (NH_4OH) and 30 ml hydrogen peroxide (H_2O_2) is prepared as an etchant solution to reveal the alloy grain microstructure. Polished samples are etched for 5-10 seconds at room temperature (RT) to reveal the grain microstructure. ImageJ software is used for grain size measurements. For each sample, 10 micrographs are analyzed and the grain size is an average of 300-400 data points. For cross-sectional imaging of Bi2212 conductors, samples are prepared by mounting small pieces of wire using a Durocit cold mounting liquid with graphite added so that the mounting is conductive. Mounted samples are grinded using SiC papers, and polished with 1.0, 0.3 and 0.05 μm alumina suspensions. The percentage of superconducting fill factor (SC%) is calculated from the optical images of Bi2212 green wires using Photoshop and ImageJ software.

2.3.1.2. Scanning Electron Microscopy (SEM)

A table-top Hitachi TM3000, a Hitachi S3200 and a field emission SEM (JEOL JSM-6400F) are used to study the alloys microstructure (grain size, oxide precipitates size, shape and

distribution), fracture surfaces, and the microstructure of Bi2212 RW's after various heat treatments.

2.3.1.3. Transmission Electron Microscopy (TEM)

Transmission electron microscopy (TEM) is used to investigate the size, shape and distribution of Al_2O_3 precipitates in the Ag/Al and MgO precipitates in the Ag/0.20wt%Mg alloy with a JEOL 2000FX. HRTEM studies are performed with a JEOL 2010 TEM to acquire high resolution images from strain centers, stacking faults, deformation twins and other defects present around the oxide precipitates. TEM samples are prepared by mechanically polishing alloy sheets using SiO_2 papers down to the thickness of about 30-40 μm , punched into a 3 mm round disk and then perforated by a low angle-low energy ion milling procedure (Fischione 1010 Ion Mill). All TEM studies are done with an accelerating voltage of 200kV.

2.3.1.4. Focused Ion Beam (FIB)

Al_2O_3 precipitate sizes and distribution are also examined using ion channeling contrast imaging on a Focused Ion Beam (FIB) with a field emission gun (FIB - FEI Quant 3D FEG). This microscope is a dual beam instrument that combines a traditional field emission scanning electron microscope (FESEM) column with a FIB column. FIB is also used for TEM sample preparation from various cross sectional areas of Bi2212 wires.

2.3.1.5. Aberration corrected Scanning Transmission Electron Microscopy

An aberration corrected FEI Titan 80-300 KV probe scanning transmission electron microscope (STEM/TEM) with monochromator is used to study the microstructure of internally oxidized Ag/Al alloys and elemental composition of oxide precipitates. The SUPER X Energy Dispersive Spectrometry (EDS) system in Titan is able to collect characteristic X-Ray signal at high counts per second. The combination of field emission electron source and SUPER X together is called ChemiSTEM technology, which makes elemental mapping at atomic level possible. The FEI-Titan is operated at accelerating voltage of 200kV. The Bruker ESPRIT software package is used for drift correction during acquisition and post-processing with a 3-pixel smoothing filter to reduce noise.

2.3.2. Mechanical behavior

2.3.2.1. Hardness test

The local mechanical properties of the samples are assessed using Vickers micro-hardness (HVN) measurements. HVN is used to measure and compare the strength of the Ag/Al alloys and Bi2212 wires at various heat treatment conditions. HVN measurements are performed on a Buehler Micromet II micro-hardness tester with a 50 gr load and a 15 seconds holding period. The dwell time of 15 seconds for each indent is concurrent with ASTM standards. A mirror polished surface prepared by mechanical grinding and polishing is used for all samples to get accurate hardness data. For each sample type, two specimens are tested, and

for each specimen, ten indentations are used to obtain reasonably accurate data and standard deviation.

2.3.2.2. Tensile test

Room temperature (RT) tensile tests on Bi2212 wires are performed using a linear tensile testing device. The device is instrumented with a 90 lb load cell and linear LVDT displacement sensor to enable force and displacement measurements. LabVIEW controls the stepper motor, data acquisition from transducers via digital multimeters and their conversion into stress and strain [1]. Figure 2-5 shows the RT tensile-testing equipment used here. The front control view of the LabVIEW program used for controlling the RT tensile-testing equipment is shown in Figure 2-6.

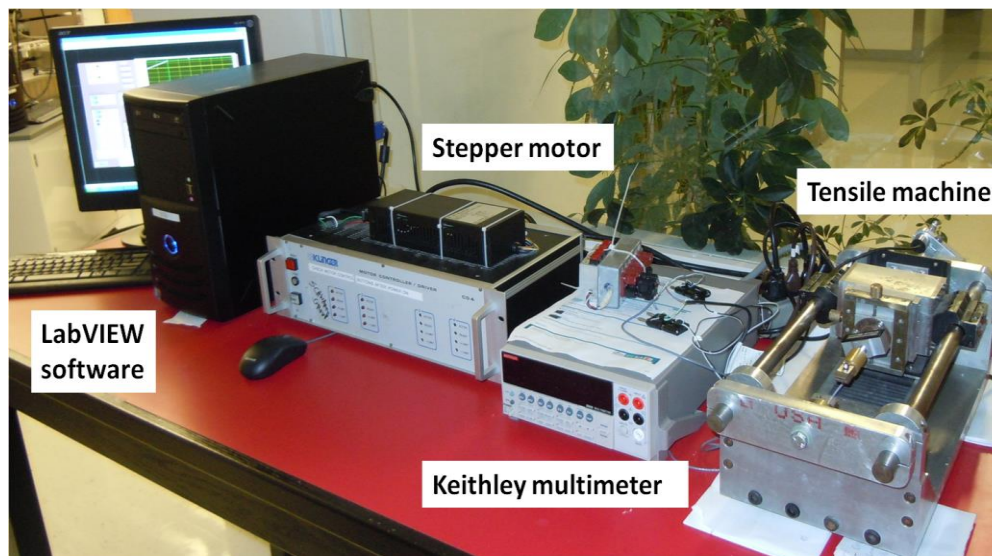


Figure 2-5: Room temperature tensile-testing equipment used for Bi2212 RW samples.

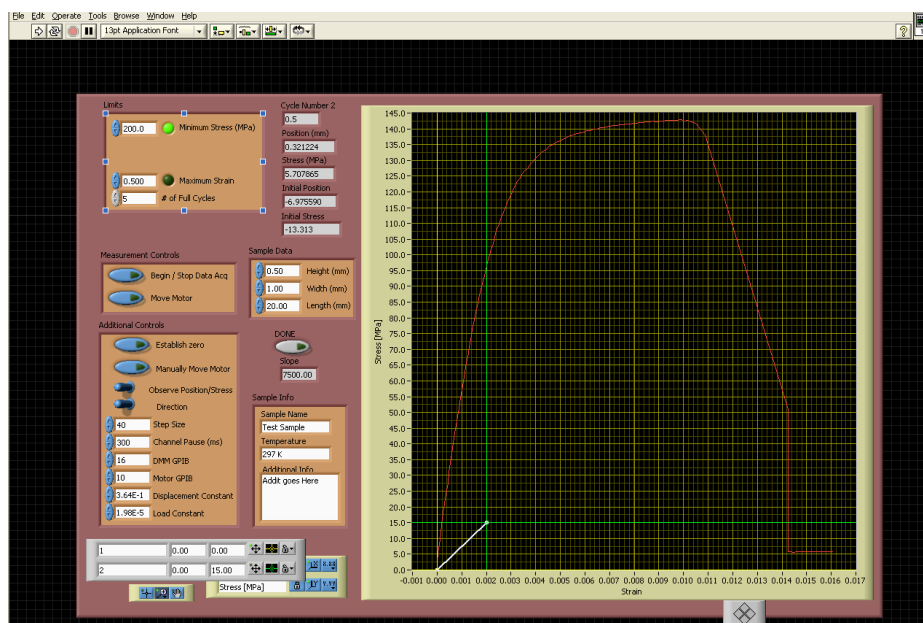


Figure 2-6: The LabVIEW program used for controlling the RT tensile-testing equipment.

For solid Ag/Al alloy wires, RT tensile tests are performed utilizing a benchtop INSTRON model 1011 tensile-testing machine with a 100 lb load cell. At least three tests are conducted for each sample condition, and the Young's modulus (E), yield strength (YS), ultimate tensile strength (UTS) and percent elongation (El %) are determined. A RT tensile-testing machine, equipped with Igor 6.04 professional software, is also used to measure the tensile behavior of the alloy sheets. For each sheet sample type, 2-3 tests are run [2].

77 K and 4.2 K tensile tests for Bi2212 wires and solid alloy wires are performed on straight wires (≈ 110 mm long) using a servo hydraulic system with a MTS (Flex Test SE) controller. Each end of the sample is soldered to a Cu grip; the sample length between the grips is at least 65 mm. The applied force is measured by a calibrated 1300 N capacity load-cell and displacement is measured using double Nyilas-type extensometers attached directly to the sample with a gauge length of ≈ 25 mm. The Young's modulus is derived from the initial linear part of the stress/strain curve measured during loading and the yield stress is determined using of the 0.2% strain offset criterion [3, 4].

2.3.3. Electrical behavior

2.3.3.1. Critical current (I_c) test

For characterizing the electrical behavior of a superconducting material, the current-voltage relationship is measured. The most common parameter obtained from the I-V measurement is

the transport critical current (I_c) which is defined as the maximum current that can be carried by the superconductor material in the superconducting state [5]. In practice, I_c is identified by either an electric field or resistivity criterion. An empirical quantity known as *n-value* of the superconducting to normal state transition which is related to the I_c ($V=I^n$), is also obtained. It quantifies the sharpness of the superconducting transition and influences the required ratio of operating current to the I_c in a superconducting magnet. After heat treatment, the I_c is measured for 50 cm long samples using the standard four-point method in liquid helium (4.2 K) at self-field. A 1 $\mu\text{V}/\text{cm}$ electric-field criterion and a 18-20 mm voltage tap spacing is used to determine I_c . For each sample type, three measurements are performed. Critical current density (J_c) is also calculated by dividing I_c by the superconductor area in the cross-section of the wire which is measured on the green wire. The J_c values reported are averages of at least three samples for each heat treatment with a maximum variance of less than 10%.

In the four-point electrical setup, a known precision resistor (R) is connected in series with the superconductor sample (Bi2212 wire here). The voltages across the resistor and between the voltage taps connected to sample are measured when the current is ramping in the circuit. The current through the series circuit is calculated using Ohm's law ($V=IR$) and a measured voltage across the resistor. The current and the voltage measured across the superconductor sample are plotted to form an I-V curve. Figure 2-7 shows a schematic view of the electrical measurement system. A computer is used to control the power supply, collect data from digital multimeters, plot the I-V curve and calculate the I_c and *n-value* via a LabVIEW

program. The ramp generator is connected to the power supply to ramp the current during measurements. The digital multimeters are used to measure the voltages across the precision resistor and the sample. The devices used in this work are as follow:

- DC power supply as current source: HP 6681A, (0-8V, 875A)
- Digital multimeter: Keithley 2001 with a GPIB-USB adaptor

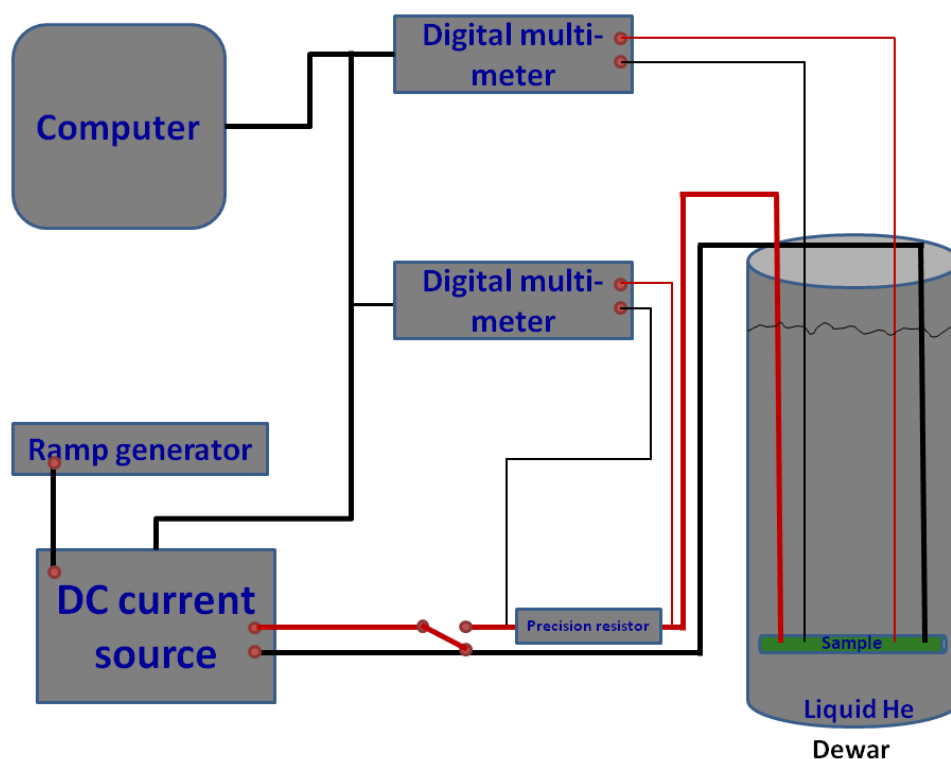


Figure 2-7: Schematic of equipment for Bi2212 round wire electrical characterization showing connections between different devices.

2.3.3.2. Resistivity vs. temperature (ρ -T)

The electrical resistivity of Ag/0.20wt%Mg and Ag/Al alloy wires and sheets as a function of temperature is measured from 4.2 K to RT at various heat treatment conditions. Resistivity is measured using the four-point method with a 2.5 mm probe spacing. A combination of two Keithley, one 6221 and a 2182A model, setup in *Deltamode* is used for R-T measurements. A constant current of 0.1 ampere is generated by Keithley 6221 current source and passed through the sample by outer current probes in the four-point probe setting. Then, the voltage generated across the sample is measured using two inner sensing probes by use of a Keithley 2182A nano-voltmeter unit. The contacts are made with spring loaded pogo-pins with fixed probe spacing of 2.5 mm and thickness of the sample sheets is chose to be a few hundred microns only so we can categorize our sheets as thin samples. Resistivity (ρ) is calculated from the resistance (V/I) value measured by Deltamode setup and thickness of the sample sheets using the following expression:

$$\rho(\text{ohm cm}) = 4.53 * Cf * \left(\frac{V}{I}\right) * t(\text{cm})$$

Where Cf ~ 0.65 is the “correction factor” which is calculated on the basis of ratio of the dimensions of the samples and probe spacing and “t” is thickness of the sample. $4.53 * Cf * (V/I)$ is called sheet resistance and when we multiply sheet resistance with thickness we get resistivity of the material.

2.3.4. Coil studies

Two single layer spirals of Bi2212/Ag/Ag0.5Al are wound for leakage studies. Spiral I, which is 10 turns of wire totaling 1 m, and Spiral II, which is 20 turns of wire totaling 2 m. Spiral I is heat treated with the PMP shown in Figure 2-4a and Spiral II uses SMP shown in Figure 2-4b. Turn-to-turn insulation used for both spirals is a 72% Al₂O₃, 28% SiO₂ ceramic fiber braided onto the wire.

2.4. References cited

- [1] J. Schwartz, *et al.*, "Mechanical properties and strain effects in Bi₂Sr₂CaCu₂O_x/AgMg composite conductors," *IEEE Transactions on Applied Superconductivity*, vol. 7, pp. 2038-2041, 1997.
- [2] K. M. Youssef, *et al.*, "Ultrahigh strength and high ductility of bulk nanocrystalline copper," *Applied Physics Letters*, vol. 87, pp. 091904-091904-3, 2005.
- [3] X. F. Lu, *et al.*, "Electromechanical Characterization of Bi-2212 Strands," *IEEE Transactions on Applied Superconductivity*, vol. 21, pp. 3086-3089, 2011.
- [4] A. Nyilas, "Strain sensing systems tailored for tensile measurement of fragile wires," *Superconductor Science and Technology*, vol. 18, p. S409, 2005.
- [5] H. W. Weijers, *et al.*, *Electrical measurements on superconductors by transport* vol. 2012: John Wiley & Sons, Inc., 2012.

CHAPTER 3

Step I: Dispersion-Strengthened Ag/0.50wt%Al alloy for sheathing $\text{Bi}_2\text{Sr}_2\text{CaCu}_2\text{O}_{8+x}$ Multifilamentary round wire

3.1. Background and motivation

Despite the recent successes with Ag/0.20wt%Mg sheathed Bi2212, the use of Ag/0.20wt%Mg for the outer sheath poses challenges and limitations, including increased difficulty in conductor manufacturing. The alloy has low strength in the un-reacted condition and loses ductility rapidly as it is drawn, necessitating frequent anneals. In this condition, the alloy can be extruded and cold-drawn to form tubing. During drawing, it work-hardens and loses ductility. Annealing restores ductility, but this must be done in an inert atmosphere, or MgO will precipitate on the grain boundaries and embrittle the alloy, making further cold-working impossible. Only during the final heat treatment is it desirable to form MgO precipitates through internal oxidation. The MgO dispersion formed by internal oxidation is resistant to coarsening and hardens the alloy even after full partial melt processing (PMP). In the fully processed condition, the tensile strength of the alloy is approximately four times greater than that of pure Ag. Most of the MgO precipitates after the Ag has re-crystallized and a significant amount of grain growth has occurred [1, 2].

Dispersion-strengthening (DS) is an effective method for producing a fine grain metallurgical structure that is resistant to softening during high temperature heat treatment. Compared to other methods for particle strengthening, such as blending or mixing hard particles with metal powders, dispersion-strengthening by internal oxidation heat treatment produces nanosize oxide precipitates that are distributed homogeneously within the Ag matrix grains. These precipitates refine the grain structure and impede dislocation movement. Therefore, an improved DS Ag alloy, which is internally oxidized prior to conductor fabrication, could produce a higher strength conductor after PMP.

In this chapter, a DS Ag/0.5wt%Al (DS Ag/0.50Al) alloy manufactured via powder metallurgy with an internal oxidization process is used for making double restack Bi2212/Ag0.50Al multifilamentary round wire (RW) conductor. The DS Ag/0.50wt%Al alloy is used as the outer sheath while pure Ag is used for the inner sheath of Bi2212 next to the filament. For making the DS Ag/0.50wt%Al alloy, first, the as-atomized Ag/0.50wt%Al metal powder is produced by powder metallurgy and annealed at 700°C for 4 hours under an argon atmosphere. After annealing, the powder is placed in a tray and heated at 675-700°C for 24 hours in the flow of 100% oxygen. The oxidized powders are then used for making DS Ag/0.50wt%Al solid alloy wires and sheets with the steps described at section 2.1.2. Next, the pre-oxidized and hardened DS Ag/0.50wt%Al alloy sheath is used for making double restack Bi2212/Ag0.50Al wire.

3.2. Experimental method

Microstructure, mechanical and electrical properties of fabricated DS Ag/0.50wt%Al solid alloy wires and sheets are studied using optical and field emission scanning electron microscopy (FESEM), room temperature (RT), 77 K and 4.0 K¹ tensile test, Vickers micro-hardness (HVN), electrical resistivity and transport measurements. The results are compared with pure Ag and Ag/0.20wt%Mg alloy sheets and wires. Several conditions are considered to compare the alloys' behaviors. Table 3-1 summarizes the samples and the various conditions; note that all alloy and conductor samples are tested before and after a heat treatment that simulates the Bi2212 partial melt process; temperature-time details are shown in Figure 2-4a. All annealing heat treatments are done under an argon atmosphere.

¹ Low temperature tensile tests were done at National Institute of Standards & Technology (NIST), Boulder, CO, where the boiling point of liquid He is 4.0 K.

Table 3-1: Various alloy sheet and wire samples and their processing conditions

Sample name	Heat treatment condition
Pure Ag	<ol style="list-style-type: none"> 1. Rolled + annealed at 375 °C for 20 min 2. Rolled + annealed at 375 °C for 20 min + PMP heat treated
Ag/0.20wt%Mg	<ol style="list-style-type: none"> 1. As-rolled 2. As-rolled + PMP heat treated 3. Rolled + annealed at 375 °C for 20 min 4. Rolled + annealed at 375 °C for 20 min + PMP heat treated
DS Ag/0.50wt%Al	<ol style="list-style-type: none"> 1. As-rolled 2. As-rolled + PMP heat treated 3. Rolled + annealed at 375 °C for 20 min 4. Rolled + annealed at 375 °C for 20 min + PMP heat treated 5. Rolled + annealed at 850 °C for 20 min + PMP heat treated

In addition to alloy wires and sheets, microstructure, RT, 77 K and 4.0 K tensile behaviors, critical current (I_c) and critical current density (J_c) measurements are done for Bi2212/Ag0.50Al and Bi2212/Ag0.20Mg round wire conductors. 50 cm short samples of Bi2212/Ag0.50Al wire with and without insulation and two single-layer spirals are also studied: Spiral I, which is 10 turns of wire totaling 1 m in length, and Spiral II, which is 20 turns of wire totaling 2 m in length. Spiral I is heat treated with the PMP shown in Figure 2-

4a and Spiral II uses a SMP heat treatment shown in Figure 2-4b. The turn-to-turn insulation used for both spirals is a 72 wt% Al_2O_3 , 28 wt% SiO_2 ceramic fiber braided onto the wire.

3.3. Results and Discussion

3.3.1. Part I: Alloy characterization

3.3.1.1. Microstructural observations

High-resolution FESEM images from the DS Ag/0.50wt%Al alloy before and after PMP heat treatment are illustrated in Figure 3-1. The dark gray, small nanoparticles are Al_2O_3 precipitates that are distributed uniformly in the Ag matrix. After PMP heat treatment (see figure 3-1b), the average Al_2O_3 nanoparticle size increased and the number of precipitates decreased. The Ag grain size before and after PMP is measured to be about 105 and 145 nm, subsequently. The Al_2O_3 precipitates size is nearly 55-85 nm before PMP. After PMP, there exist in two different sizes: One group is smaller with the average diameter of about 110 nm and the second group is larger with an average diameter of 400 nm. There is a degree of coarsening for both Ag grains and Al_2O_3 precipitates in the DS Ag/0.50wt%Al alloy during PMP heat treatment. Ideally, the powder particles should be uniformly exposed to the oxygen atmosphere during the internal oxidation heat treatment to form oxide precipitates. An oxygen flow over the top of the Ag/0.50wt%Al powder which is used in the first method for making the DS Ag/0.50wt%Al alloy, would likely result in an O_2 gradient through the powder bed and this may not be an ideal oxidation technique.

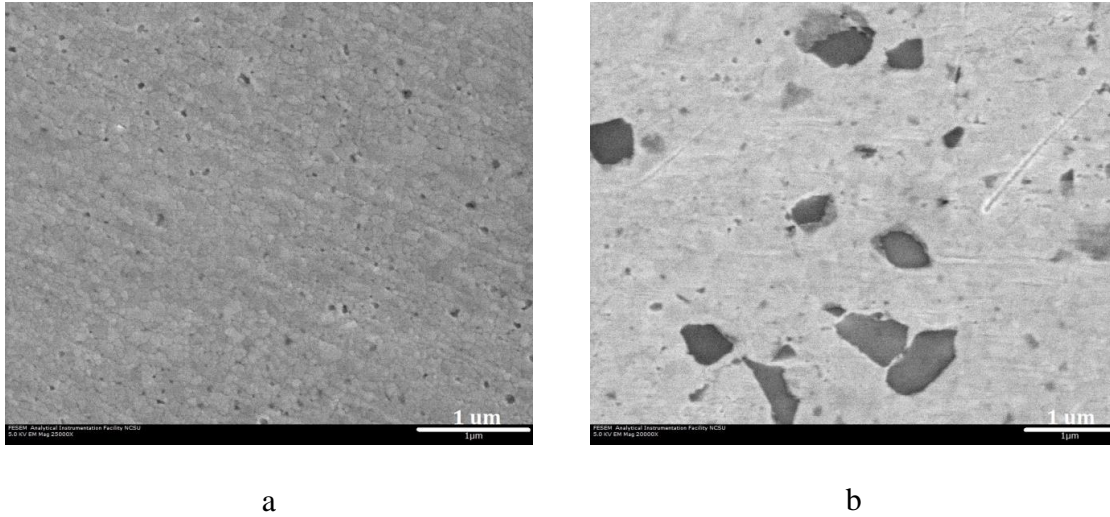


Figure 3-1: FESEM images of DS Ag/0.50wt%Al alloy (a) before and (b) after PMP heat treatment.

3.3.1.2. Mechanical properties

3.3.1.2.1. RT tensile test for alloy sheets

RT tensile tests have been performed for pure Ag, DS Ag/0.50wt%Al and Ag/0.20wt%Mg as a function of annealing condition to understand their mechanical properties before and after PMP. Figure 3-2 shows the tensile stress/strain behavior of as-rolled Ag/0.20wt%Mg before and after PMP. In this case, heat treatment significantly increases the tensile strength (UTS) and percent elongation (El %). This is due to the formation of MgO precipitates during PMP heat treatment under O₂ atmosphere and the strengthening effects of these small precipitates within the Ag matrix. Figure 3-3 plots the tensile stress/strain behaviors of pure Ag, Ag/0.20wt%Mg and DS Ag/0.50wt%Al alloy sheets that are annealed at 375°C under an

argon atmosphere. Also shown are results for the same alloy sheets that are PMP treated in O₂ after the argon annealing. For pure Ag, the toughness decreases during PMP which may be due to the diffusion of O₂ into the Ag, causing embrittlement. Ag/0.20wt%Mg in the annealed condition is soft, with ~36 % elongation to failure. After PMP heat treatment, the alloy is nearly twice as strong, but the elongation to failure is reduced to roughly 22%. Annealed DS Ag/0.50wt%Al alloy shows very high UTS, about 620 MPa. After PMP heat treatment, however, the UTS decreases but the failure strain is very high (35%). This is due to coarsening of the Al₂O₃ nanoparticles at high temperature, resulting in a decreased number of larger particles.

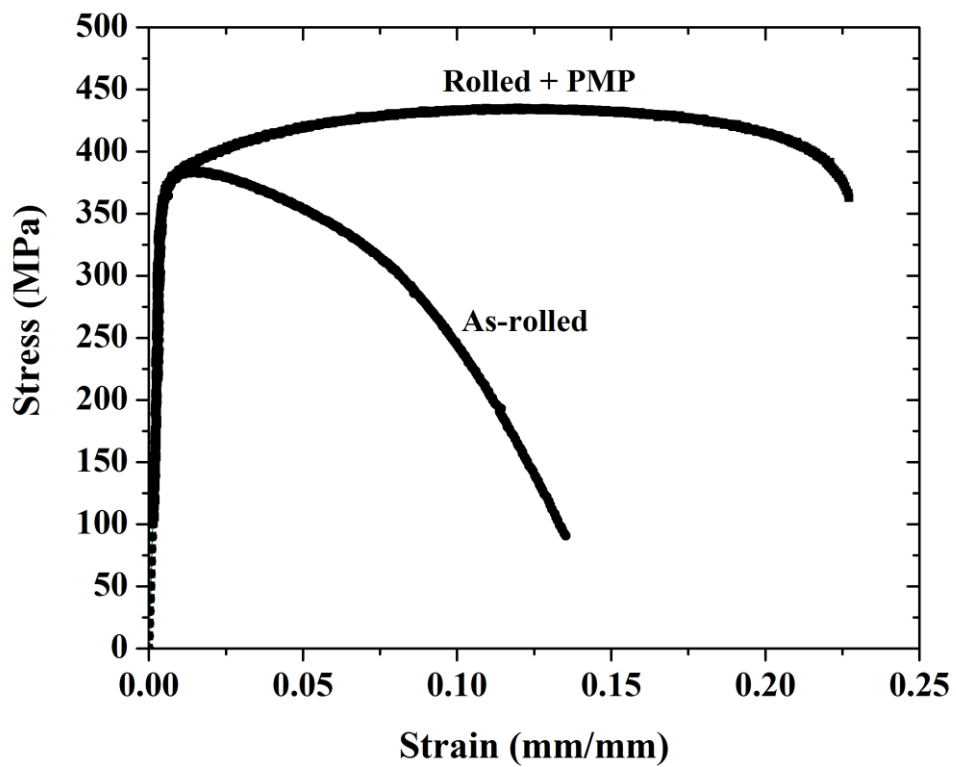


Figure 3-2: RT stress/strain behavior of as-rolled Ag/0.20wt%Mg alloy before and after PMP heat treatment.

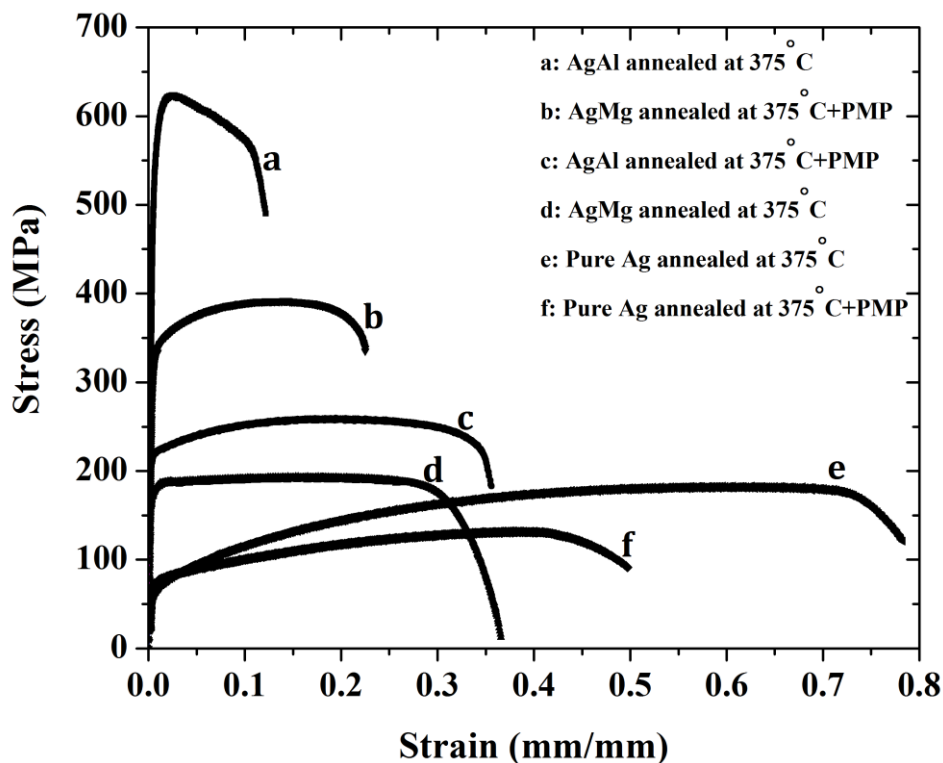


Figure 3-3: RT stress/strain behavior of annealed Ag/0.20wt%Mg, DS Ag/0.50wt%Al and pure Ag sheet alloys before and after PMP heat treatment.

Table 3-2 summarizes the mechanical properties of all tested samples at RT. While annealed DS Ag/0.50wt%Al alloy shows very high ultimate tensile strength (UTS) and yield strength (YS) in comparison to those of Ag/0.20wt%Mg alloy, after PMP heat treatment, the Ag/0.20wt%Mg shows higher UTS and YS than those of DS Ag/0.50wt%Al, due to coarsening of Al_2O_3 precipitates within the Ag matrix in the DS Ag/0.50wt%Al alloy. A

more detailed investigation of thermo-mechanical processing parameters is needed to develop improved resistance to softening during PMP.

Table 3-2: RT tensile test results for pure Ag, Ag/0.20wt%Mg and DS Ag/0.50wt%Al sheet alloys

Mechanical Parameters	Pure Ag			
	E (GPa)	YS (MPa)	UTS (MPa)	EI %
Rolled + annealed at 375 °C for 20 min	80	62 ± 1.5	182 ± 2	78.3 ± 0.3
Rolled + annealed at 375 °C for 20 min + PMP heat treated	80	70 ± 3	131 ± 5	49.7 ± 0.2

Mechanical Parameters	Ag/0.20wt%Mg			
	E (GPa)	YS (MPa)	UTS (MPa)	EI %
As-rolled	80	353 ± 3	381 ± 2	12.1 ± 0.5
Rolled + PMP heat treated	80	356 ± 4	430 ± 10	23.7 ± 0.8
Rolled + annealed at 375 °C for 20 min	80	160 ± 2	192 ± 1	36 ± 0.4
Rolled + annealed at 375 °C for 20 min + PMP heat treated	80	310 ± 4	396 ± 1	21.9 ± 0.9

Mechanical Parameters	DS Ag/0.50wt%Al			
	E (GPa)	YS (MPa)	UTS (MPa)	EI %
Rolled + annealed at 375 °C for 20 min	85	532 ± 1	620 ± 3.5	12.2 ± 2
Rolled + annealed at 375 °C for 20 min + PMP heat treated	85	210 ± 2	268 ± 2.8	37 ± 1.5

3.3.1.2.2. DS Ag/0.50wt%Al solid alloy wire tensile behavior at RT, 4.0K

The RT tensile properties of DS Ag/0.50wt%Al solid alloy wires are summarized in Table 3-3. The strength remains high after drawing and annealing up to 850°C but, like the alloy sheet, significantly decreases after PMP.

The 4.0 K tensile stress/strain behaviors of three groups of DS Ag/0.50wt%Al solid alloy wires with various heat treatment conditions are shown in Figure 3-4. The DS Ag/0.50wt%Al solid wire shows very high YS and UTS in the annealed condition at 4.0 K, 748 MPa and ~850 MPa, respectively. After PMP, the mechanical strength decreases and the El% increases; results are tabulated in Table 3-4. The trend in strength is the same as that observed at RT. Note that the annealing temperature has no significant effect on the low-temperature mechanical properties; there is little difference between annealing at 850°C in comparison to 375°C. Interestingly, there is still significant ductility at 4.0 K, a temperature at which Ag and Ag/0.20wt%Mg have little measurable ductility. This is likely due to the much finer grain size in the DS Ag/0.50wt%Al alloy.

Table 3-3: RT tensile properties for DS Ag/0.50wt%Al solid alloy wires with various heat treatments

Sample conditions	E (GPa)	YS (MPa)	UTS (MPa)	El %
As-drawn	85	470	578	4
Rolled + annealed at 375 °C for 20 min	85	511	617	6
Rolled + annealed at 850 °C for 20 min	85	457	589	5
Rolled + annealed at 375 °C for 20 min + PMP heat treated	85	207	249	43

3.3.1.2.3. Vickers micro-hardness (HVN) measurements

The Vickers micro-hardness (HVN) test is an indicator of mechanical properties of mild strength alloys and sheets. Here, HVN measurements are used to better understand the mechanical properties of the DS Ag/0.50wt%Al alloy and to further compare it to Ag/0.20wt%Mg alloy. The HVN results are shown in Table 3-5. The annealed Ag/0.20wt%Mg alloy has an HVN of 40, whereas that of the annealed DS Ag/0.50wt%Al alloy is 168, consistent with the mechanical properties of both alloys at RT. After PMP, the Ag/0.20wt%Mg HVN increased due to the formation of MgO, whereas in the DS Ag/0.50wt%Al alloy, HVN decreased after PMP, which is again consistent with tensile properties.

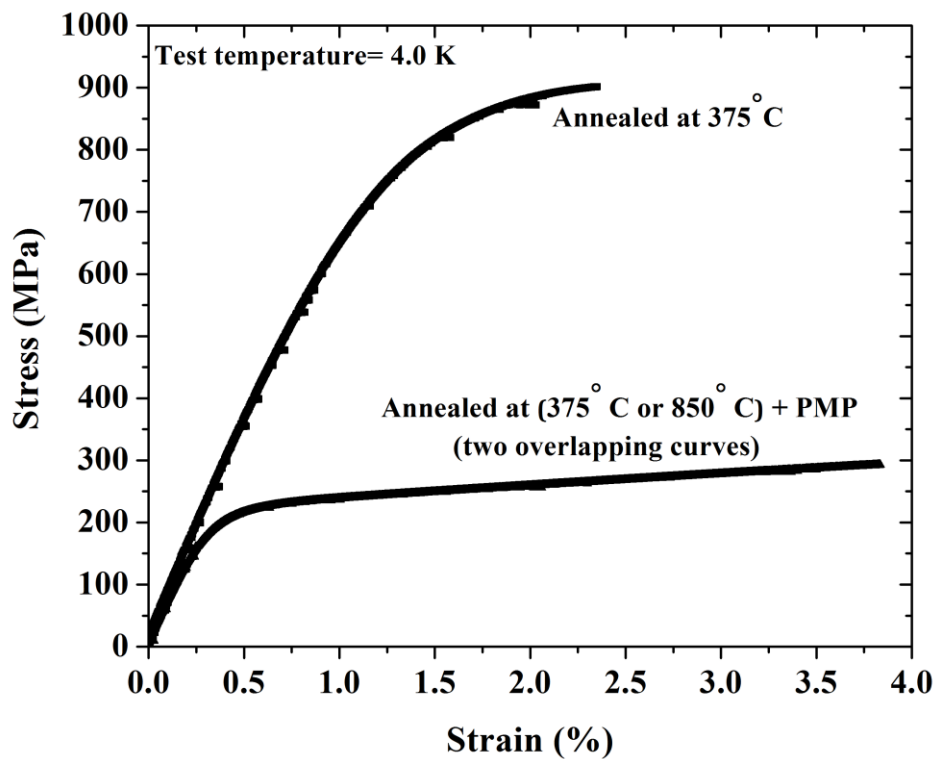


Figure 3-4: Stress/strain behavior of three groups of DS Ag/0.50wt%Al solid alloy wires at 4.0 K. One sample was annealed at 375 °C for 20 min; and two other samples, one annealed at 375 °C and the other at 850 °C before being partial-melt processed. The results from the latter two overlap on the graph.

Table 3-4: Tensile behaviors of DS Ag/0.50wt%Al solid alloy wires at 4.0 K with various heat treatments

Sample conditions	E (GPa)	YS (MPa)	UTS (MPa)	El %
Rolled + annealed at 375 °C for 20 min	68	748	850	2.40
Rolled + annealed at 375 °C for 20 min + PMP heat treated	59	221	295	3.60
Rolled + annealed at 850 °C for 20 min + PMP heat treated	65	220	295	3.82

Table 3-5: Vickers micro-hardness (HVN) for all alloy sheets

Vickers Micro-hardness – HVN\pmSTD (0.25 N, 15 s)			
Sample conditions	Ag	Ag/0.20wt%Mg	DS Ag/0.50wt%Al
As-rolled	-	100 \pm 5	165 \pm 4
Rolled + PMP heat treated	-	127 \pm 4	94 \pm 5
Rolled + annealed at 375 °C for 20 min	38 \pm 3	40 \pm 4	168 \pm 3
Rolled + annealed at 375 °C for 20 min + PMP heat treated	31 \pm 2	116 \pm 7	87 \pm 3

3.3.1.2.4. Tensile samples fractography

Fracture surfaces of tensile specimens tested at RT have been examined using SEM. Figure 3-5 illustrates the fracture surfaces for DS Ag/0.50wt%Al and Ag/0.20wt%Mg alloys after PMP heat treatments. The DS Ag/0.50wt%Al fracture surface shows microvoids characteristic of ductile fracture in a fine-grained microstructure containing dispersed particles (see Figure 3-5a) [3]. Fracture in the Ag/0.20wt%Mg alloy exhibits grain boundary cavitation indicative of low ductility fracture (see Figure 3-5b) [4]. This microstructure is susceptible to intergranular failure at low stress levels and during thermal cycling. These behaviors indicate that DS Ag/0.50wt%Al alloy is tougher than the more brittle Ag/0.20wt%Mg alloy.

3.3.1.3. Electrical properties

3.3.1.3.1. Resistivity measurements

The electrical resistivity is measured as a function of temperature for pure Ag and DS Ag/0.50wt%Al solid alloy wires in three different annealing conditions. Table 3-6 summarizes the data at RT, 77 K and 4.2 K. In general, for both pure Ag and DS Ag/0.50wt%Al wires, the electrical resistivity decreases with decreasing temperature. This is due to lower atomic vibrations and smaller phonon scattering at lower temperatures. After PMP, the defect density is reduced, resulting in reduced electron-defects scattering and decreased resistivity. Interestingly, for DS Ag/0.50wt%Al, there is no significant difference

in electrical resistivity in as-drawn and annealed wires at RT and 77 K both before and after PMP. After PMP, all samples' resistivity decreased. After PMP, the electrical resistivity for DS Ag/0.50wt%Al at RT is reduced by about 33 %, at 77 K by three orders of magnitude, and at 4.2 K by several orders of magnitude. Furthermore, there is no difference in the resistivity before and after PMP heat treatment for as-drawn DS Ag/0.50wt%Al wire, in comparison with those that are annealed under argon at 375 °C and 850 °C at RT and 77 K.

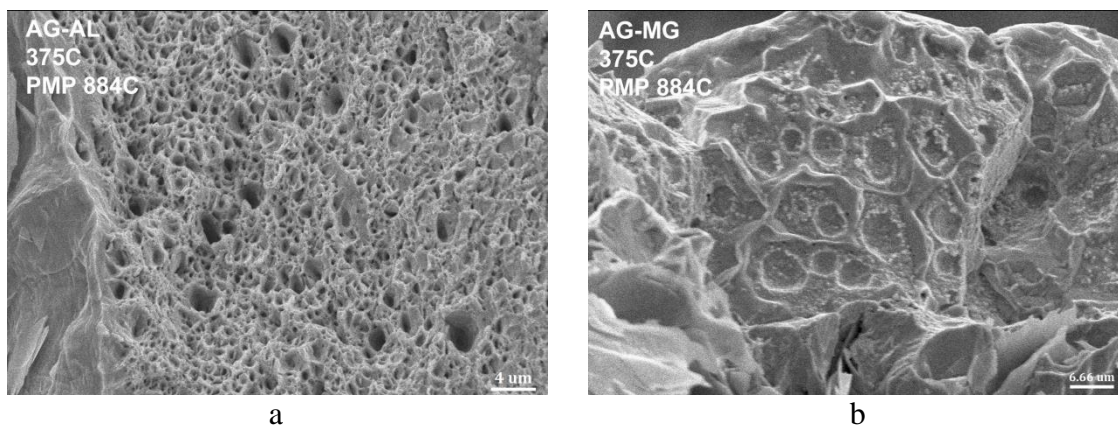


Figure 3-5: SEM images of fracture surfaces of (a) DS Ag/0.50wt%Al and (b) Ag/0.20wt%Mg alloys after PMP heat treatment. The images show ductile behavior of DS Ag/0.50wt%Al in comparison to brittle fracture of Ag/0.20wt%Mg. Note that the magnifications are not the same; optimum magnifications were chosen in order to best highlight the microstructural features.

Table 3-6: Electrical resistivity as a function of temperature for pure Ag and DS Ag/0.50wt%Al solid alloy wires

Sample condition	Electrical Resistivity ρ ($\Omega \cdot m$) $\times 10^{-9}$					
	Before PMP			After PMP		
	RT	77 K	4.2 K	RT	77 K	4.2 K
Pure Ag	15.71	3.14	0.24	15.71	2.75	0.026
As-drawn DS Ag/0.50wt%Al alloy wire	29.41	12.25	7.35	19.61	4.90	1.59
DS Ag/0.50wt%Al wire - rolled + annealed at 375 °C for 20 min	29.41	12.25	6.13	19.61	4.90	1.47
DS Ag/0.50wt%Al wire - rolled + annealed at 850 °C for 20 min	26.96	12.25	4.90	19.61	4.90	1.72

3.3.2. Part II: Bi2212/Ag0.50Al multifilamentary RW conductor

3.3.2.1. Bi2212/Ag0.50Al microstructure

Optical micrographs from cross sections of the Bi2212/Ag0.50Al wire before and after PMP with a peak temperature of 884°C are shown in Figure 3-6. The filaments show some non-uniformity and distortion before PMP. During conductor manufacturing, the harder sheath results in greater deformation of the oxide cores than seen in Bi2212/Ag0.20Mg. The filament size is less than the target size of 15 μm . We have previously found that it is difficult

to maintain uniformity if the filament size is below about 15 μm [5]. After PMP, the filament structure becomes more irregular, with significant interfilamentary bridging and the existence of non-superconducting phases and voids, typical of Bi2212 wires.

Figure 3-7 shows a portion of the conductor that is etched to reveal the grain structure in the silver and the DS Ag/0.50wt%Al outer sheath before (see Figures 3-7a and b) and after PMP heat treatment (see Figures 3-7c and e). The grain size for the DS Ag/0.50wt%Al sheath is the limit for optical micrographs. Figures 3-7c and d are optical micrographs, and the small black spots show very fine grain sizes of DS Ag/0.50wt%Al sheath in the reacted condition after PMP. Figure 3-7e and f, which are high resolution SEM micrographs, show these fine grain structures more clearly. The sheath retains its fine grain size even after PMP (see Figures 3-7 c-f). Thus, the loss of strength is not due to grain growth, but coarsening of the oxide precipitates. For comparison, Figure 3-8a and b show the grain size of the outer alloy sheath in a Bi2212/Ag/0.20Mg wire after PMP. There is almost an order of magnitude difference in grain size between the two sheath materials.

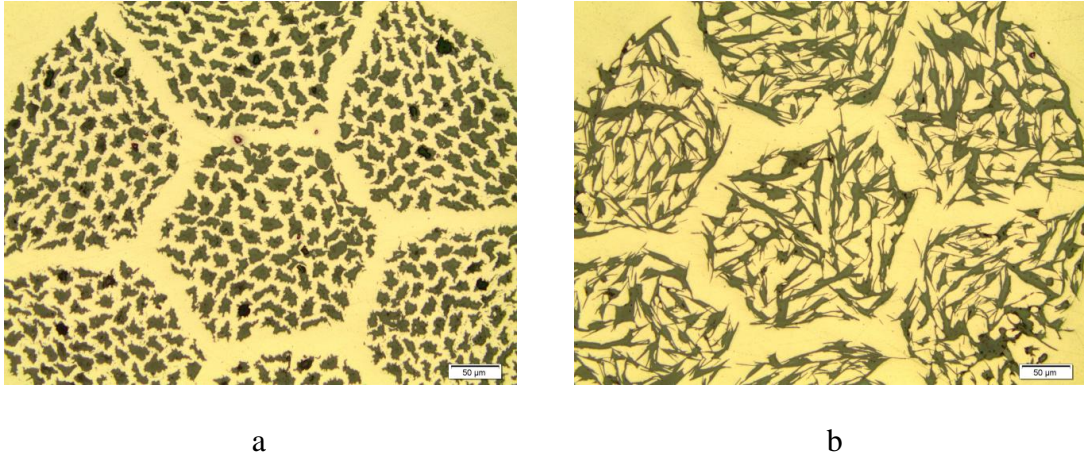
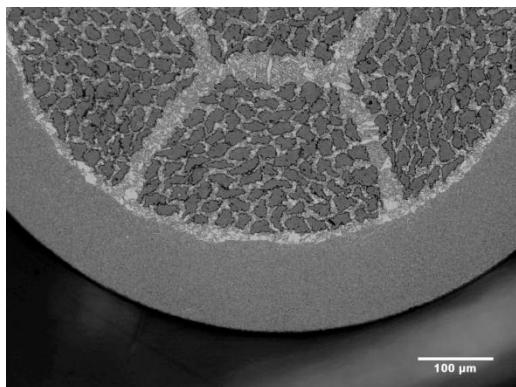


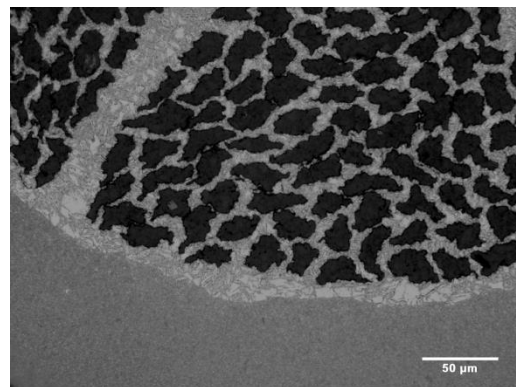
Figure 3-6: Optical images of Bi2212/Ag0.50Al multifilamentary wire (a) before and (b) after PMP heat treatment.

After PMP, the grain size in the DS Ag/0.5wt%Al outer alloy sheath in Bi2212/Ag0.50Al wire is measured to be about 1-1.5 μm while that of Ag/0.20wt%Mg alloy in Bi2212/Ag0.20Mg wire outer alloy sheath is about 13-15 μm . There is almost an order of magnitude in grain size between the two alloys.

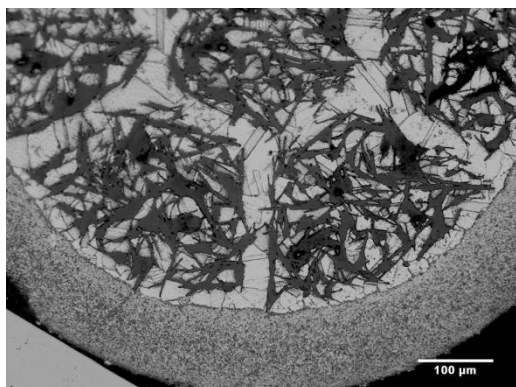
Figure 3-7: Cross-sectional images of Bi2212/Ag0.50Al wire showing grain sizes in the alloy sheath before and after PMP. (a , b) Optical micrographs of etched Bi2212/Ag0.50Al green wire (before PMP), (c , d) optical micrographs of etched Bi2212/Ag0.50Al wire after PMP, (e , f) High magnification SEM images showing the grain structure of DS Ag/0.50wt%Al alloy in the Bi2212/Ag0.50Al wire outer alloy sheath after PMP.



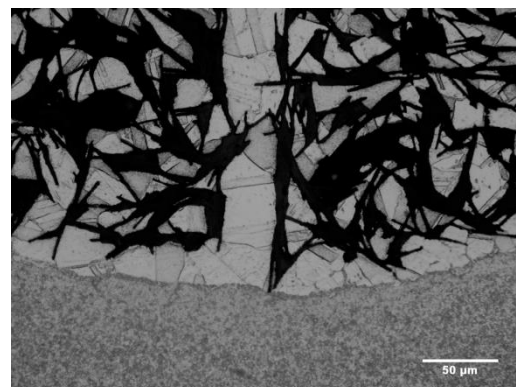
a



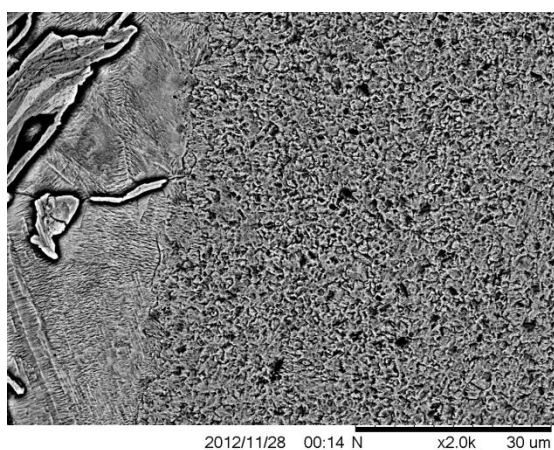
b



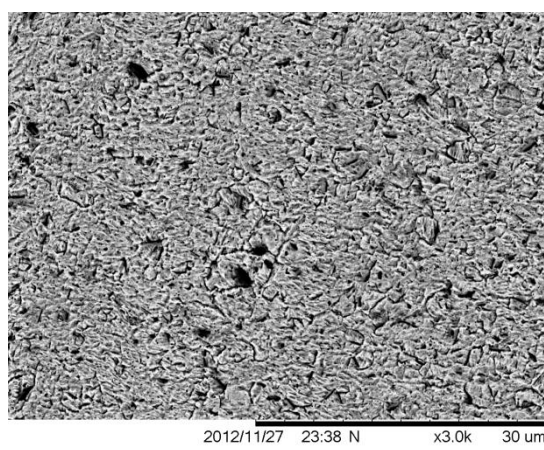
c



d



e



f

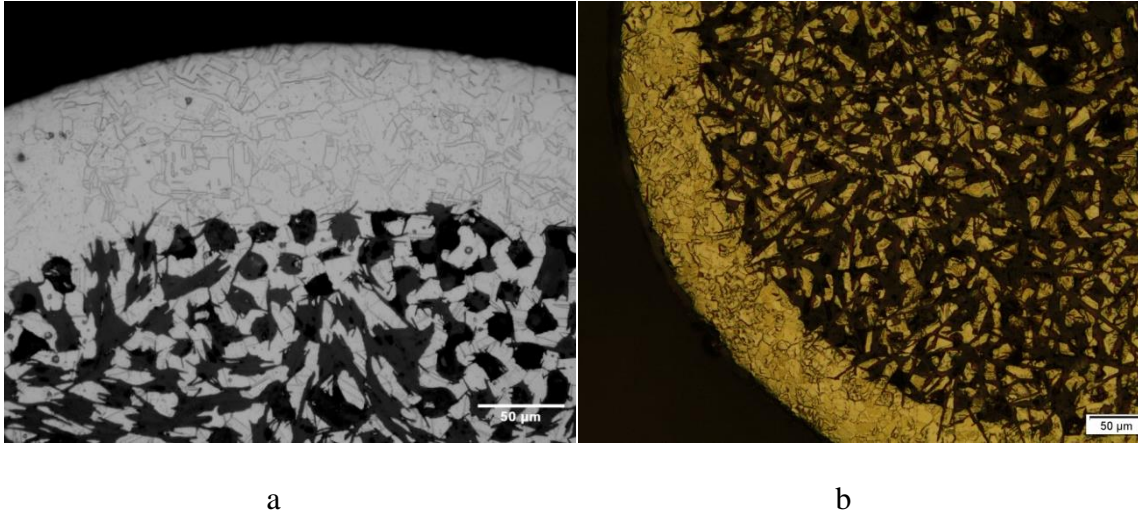


Figure 3-8: a) Cross-sectional optical micrograph of Bi2212/Ag0.20Mg wire showing the Ag/0.20wt%Mg alloy sheath grain size after PMP, and b) optical micrograph from the same Ag/0.20wt%Mg outer alloy sheath in an etched sample. The grain size is measured to be about 13-15 μm .

3.3.2.2. Tensile behavior of Bi2212/Ag0.50Al RW conductor at RT, 77 K, 4.0K

RT tensile behaviors for Bi2212/Ag0.50Al and Bi2212/Ag0.20Mg wires before and after PMP have been measured, with results shown in Figure 3-9 and summarized in Table 3-7. The Bi2212/Ag0.50Al green wire shows very high tensile strength and a noticeable elongation before fracture. After PMP, the YS and UTS of the Bi2212/Ag0.50Al wire not only are very close to those of the Bi2212/Ag0.20Mg wire, but also exhibits much higher toughness, with $> 2\%$ elongation to failure. Regarding Table 3-7, the Bi2212/Ag0.50Al has very high mechanical strength in the green condition when compared with that of

Bi2212/Ag0.20Mg. After PMP, it has comparable YS and UTS with Bi2212/Ag0.20Mg but with higher elongation and toughness.

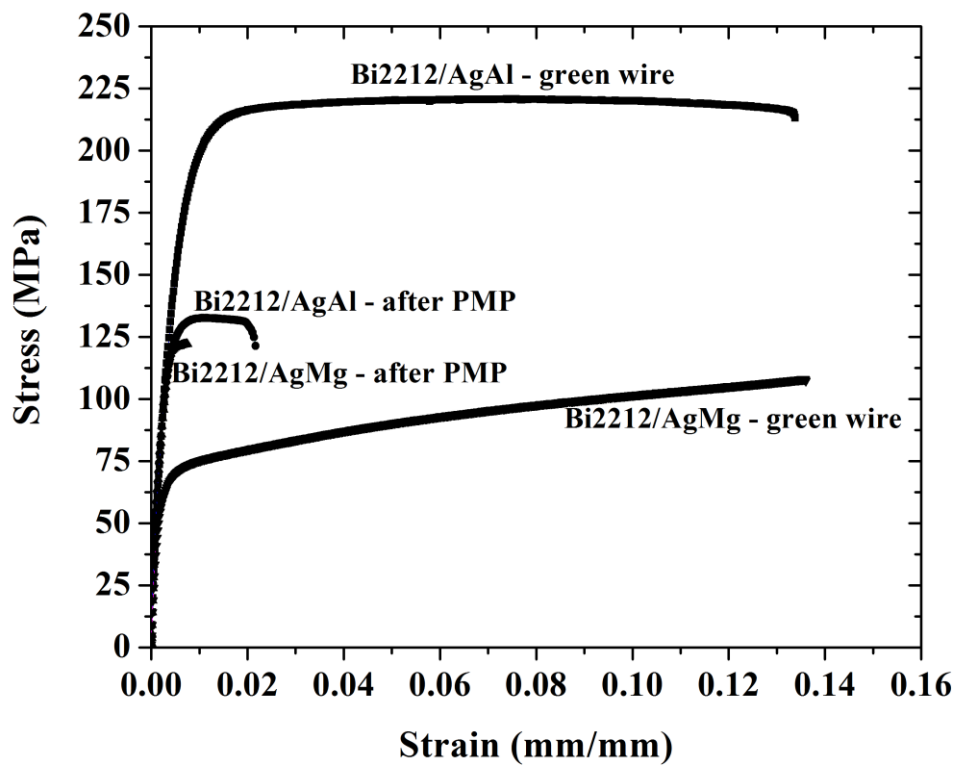


Figure 3-9: RT stress/strain behavior for Bi2212/Ag0.20Mg and Bi2212/Ag0.50Al wires before and after PMP heat treatment.

Table 3-7: RT tensile properties of Bi2212/Ag0.20Mg and Bi2212/Ag0.50Al wires before and after PMP heat treatment

Condition	Bi2212/Ag0.50Al				Bi2212/Ag0.20Mg			
	E (GPa)	YS (MPa)	UTS (MPa)	EI %	E (GPa)	YS (MPa)	UTS (MPa)	EI %
Green Wire (before PMP)	48	130	220	13.38	42	62.5	107	-
After PMP heat treatment	56	125	135	2.17	56	110	122	0.80

Tensile behaviors of Bi2212/Ag0.50Al wires after PMP heat treatment are also measured at 77 K and 4.0 K. The stress/strain plots are shown in Figure 3-10 and the strengths data are listed in Table 3-8. Bi2212/Ag0.50Al wire shows noticeable UTS and about four times higher elongation percent comparing to the Bi2212/Ag0.20Mg tensile data at RT. While Bi2212/Ag0.20Mg is very brittle at RT with EI% of about 0.8, the EI% of Bi2212/Ag0.50Al is nearly ~3 at 4.0 K. Furthermore, Bi2212/Ag0.50Al wire has comparable YS at 4.0 K with that of Bi2212/Ag0.20Mg at RT.

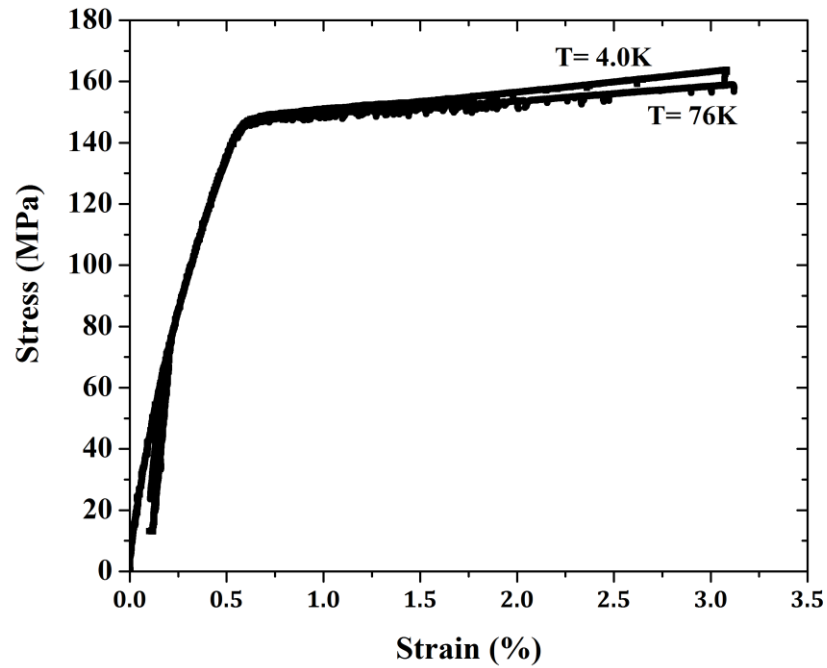


Figure 3-10: Stress/strain behavior for Bi2212/Ag0.50Al wires at 77 K and 4.0 K after PMP heat treatment.

Table 3-8: Tensile properties of Bi2212/Ag0.50Al wires after PMP heat treatment at 77 K and 4.0 K along with that of Bi2212/Ag0.20Mg at RT

Sample / test temperature	E (GPa)	YS (MPa)	UTS (MPa)	El %
Bi2212/Ag0.50Al – 77 K	67	110	158	3.12
Bi2212/Ag0.50Al – 4.0 K	66	110	163	3.07
Bi2212/Ag0.20Mg – RT	56	110	122	0.80

3.3.2.3. I_c measurements

Transport measurement results on Bi2212/Ag0.50Al wires after PMP heat treatment at zero magnetic field are presented in terms of I_c and J_c in Table 3-9, where J_c is calculated by dividing I_c by the wire cross-sectional area and filling factor, as measured after deformation but before heat treatment. For comparison, a Bi2212/Ag0.20Mg conductor with similar Bi2212 fill-factor is also included. The results show that the DS Ag/0.50wt%Al sheathed conductor performs better than the Ag/0.20wt%Mg sheathed wire, i.e., nearly 50 % in J_c , indicating that the Al_2O_3 precipitates in the sheath have neither any significant effect on oxygen solubility or oxygen diffusion through the sheath, nor any detrimental reactions with the Bi2212 filaments.

Table 3-9: Short sample I_c (A), n-value and J_c (A/mm²) results of Bi2212/Ag0.50Al and Bi2212/Ag0.20Mg wires at self-field after PMP heat treatment

Conductor type	Short samples	I_c (A)	n - value	J_c (A/mm ²)
Bi2212/Ag0.50Al RW	without insulation	328	20.4	3060
	with insulation	283	19.8	2640
Bi2212/Ag0.20Mg RW	without insulation	269	18.6	2050

3.3.2.4. Coil studies

Figure 3-11 shows photographs of the Bi2212/Ag0.50Al spirals before and after heat treatment. Although leakage is often seen in similar spirals wound with Bi2212/Ag0.20Mg [6, 7], here no leakage was observed after PMP heat-treatment. The DS Ag/0.50wt%Al alloy has an ultra-fine grain size after PMP, which is nearly an order of magnitude smaller than that of Ag/0.20wt%Mg, which may increase resistance to leakage. Alternatively, this could be evidence that leakage is influenced by interactions with Mg [7]. Figure 3-12 shows the I_c and n -value results measured at 4.2 K (self-field) including end-to-end (ETE) measurements, and measurements on segments cut along the length of the spirals. The I_c versus section plots represent transport on every two turns of conductor. For example, for the ten-turn spiral I, the x-axis sections represent turns 1 and 2, 3 and 4, 5 and 6, 7 and 8, and turns 9 and 10. These two plots show that the electrical behavior is uniform over the length of the conductor and roughly the same as the short sample results in Table 3-9.

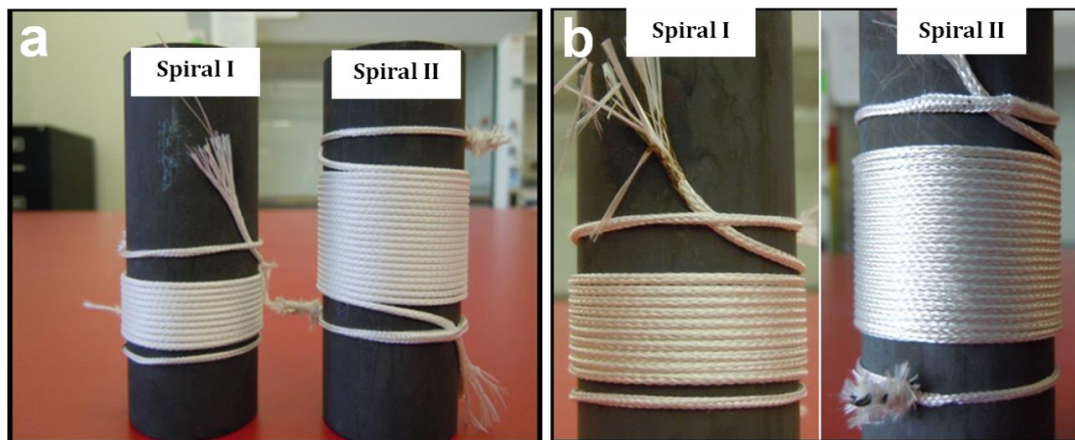


Figure 3-11: Bi2212/Ag0.50Al single layer spirals (a) before and (b) after heat treatment. Spiral I is composed of 10 turns of wire (wire length of 1 m) and Spiral II is composed of 20 turns of wire (wire length of 2 m). Spiral I is heat treated using the partial melt process and Spiral II is heat treated using the split melt process (SMP).

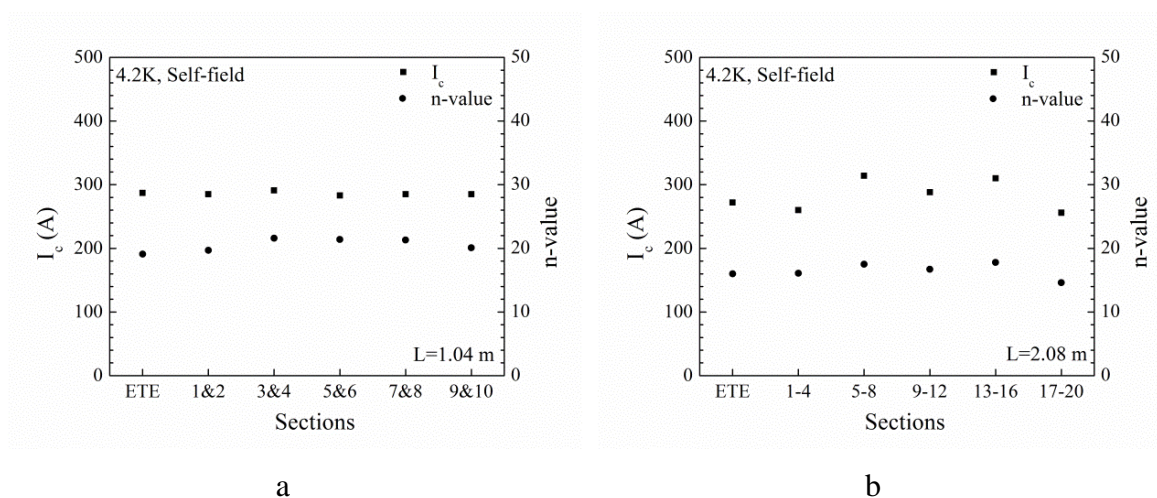


Figure 3-12: I_c and n-value for (a) spiral I and (b) spiral II. End to end (ETE) defined in the text.

3.4. Summary

This chapter presents results on the DS Ag/0.50wt%Al alloy as an alloy sheath option for Bi2212 wire. Studies have evaluated DS Ag/0.50wt%Al solid alloy wires and sheets and Bi2212/Ag0.50Al multifilamentary composites. The DS Ag/0.50wt%Al solid alloy wire showed high YS and UTS in the annealed condition at both RT and 4.0 K. The Ag/0.50wt%Al alloy also showed significant ductility at 4.0 K, i.e., a temperature at which Ag and Ag/0.20wt%Mg have little measurable ductility. Transport measurements showed that the Bi2212/Ag0.50Al wires outperform Bi2212/Ag0.20Mg wires by nearly 50%, indicating that the Al₂O₃ precipitates in the outer alloy sheath have neither any significant effect on oxygen solubility or oxygen diffusion through the sheath, nor any detrimental reactions with the Bi2212 filaments. Although leakage is often seen in similar spirals wound with Bi2212/Ag0.20Mg, no leakage has been observed after PMP and SMP heat treatments of Bi2212/Ag0.50Al spirals. Furthermore, tensile studies showed that the Bi2212/Ag0.50Al green wire has very high strength, which may be beneficial for Bi2212 compaction. After PMP, the Bi2212/Ag0.50Al wire not only has YS and UTS that are slightly higher than those of Bi2212/Ag0.20Mg wire but also exhibits > 2% elongation, which is several times higher than that of Bi2212/Ag0.20Mg. In step I, we have studied only one DS Ag/0.50wt%Al alloy composition; the results indicate that Ag/0.50wt%Al alloys have the potential for achieving significant improvement in Bi2212 electrical and mechanical behavior.

3.5. References cited

- [1] W. T. Nachtrab and P. R. Roberts, "A Review of Powder Metal-Extrusion Technology," *Advances in Powder Metallurgy & Particulate Materials - 1992, Vol 4*, pp. 321-335, 1992.
- [2] R. Navarro, "Silver alloys used in composite BSCCO tapes: development of electrical and mechanical properties during manufacture," *Superconductor Science & Technology*, vol. 13, pp. R147-R170, Dec 2000.
- [3] A. K. Vasudévan and R. D. Doherty, "Grain boundary ductile fracture in precipitation hardened aluminum alloys," *Acta Metallurgica*, vol. 35, pp. 1193-1219, 1987.
- [4] P. Onck and E. v. d. Giessen, "Growth of an initially sharp crack by grain boundary cavitation," *Journal of the Mechanics and Physics of Solids*, vol. 47, pp. 99-139, 1998.
- [5] W. T. Nachtrab, *et al.*, "The Effect of Filament Diameter on $J(e)$ in High Filament Count Bi2212/Ag Round Wire," *IEEE Transactions on Applied Superconductivity*, vol. 19, pp. 3061-3066, Jun 2009.
- [6] X. F. Lu, *et al.*, "Correlation Between Pressure Dependence of Critical Temperature and the Reversible Strain Effect on the Critical Current and Pinning Force in $\text{Bi}_2\text{Sr}_2\text{CaCu}_2\text{O}_{8+x}$ Wires," *IEEE Transactions on Applied Superconductivity*, vol. 22, pp. 8400307-8400307, 2012.
- [7] P. Majewski, *et al.*, "Diffusion of Cu into the Ag sheath of BPSCCO tapes," *Physica C: Superconductivity*, vol. 325, pp. 8-12, 1999.

CHAPTER 4

Step II: Oxide dispersion strengthened silver aluminum alloys optimized for $\text{Bi}_2\text{Sr}_2\text{CaCu}_2\text{O}_{8+x}$ round wire

4.1. Background and motivation

In the first step, as explained in the previous chapter, a dispersion-strengthened (DS) Ag/0.50wt%Al alloy sheath made by powder metallurgy was used as the outer sheath of a double-restack Bi2212/Ag/Ag0.50Al round wire [1]. Ag/0.50wt%Al metal powder, which was oxidized at 675°C for 24 hours in flowing pure oxygen, was used to form the DS Ag/0.50wt%Al alloy. The microstructural and mechanical properties were compared with those of Ag/0.20wt%Mg. In the annealed condition, the Ag/0.20wt%Mg alloy was soft at room temperature (RT), with ~36% elongation to failure and ultimate tensile strength (UTS) of 192 MPa. After partial melt processing (PMP), the Ag/0.20wt%Mg alloy was nearly twice as strong as pre-PMP with UTS of 396 MPa, due primarily to the formation of MgO precipitates during PMP heat treatment in oxygen, but the elongation to failure was reduced to roughly 22%. Before PMP, the annealed DS Ag/0.50wt%Al alloy showed very high UTS, about 620 MPa. After PMP, however, the UTS decreased to 268 MPa, although the failure strain remained high (~35%). This was a result of coarsening of the Al_2O_3 precipitates at high temperature during PMP in oxygen, resulting in a reduced number of larger Al_2O_3 precipitates. The annealed Ag/0.20wt%Mg alloy had a Vickers micro-hardness (HVN) of 40,

whereas that of the annealed DS Ag/0.50wt%Al alloy was 168, consistent with the tensile properties of both alloys at RT. After PMP, the Ag/0.20wt%Mg HVN increased to 116, whereas in the DS Ag/0.50wt%Al, HVN decreased to 84, also consistent with the tensile properties. Microstructural studies showed that the loss of strength in the DS Ag/0.50wt%Al was mainly due to coarsening of the Al_2O_3 precipitates [1-4]. Thus, although Ag/Al shows promise for improving Bi2212 wires, the internal oxidation treatment of the DS Ag/Al alloy requires optimization for strength and toughness post-PMP [1].

This chapter reports on detailed studies of the relationships between the processing and oxidation of Ag/Al alloys with various Al contents and their microstructure, mechanical and electrical properties. A series of Ag/Al alloys are studied and the internal oxidation time and temperature are varied to optimize the strength, ductility and microstructure post-PMP. The alloy properties are measured before and after PMP heat treatment and compared with Ag/0.20wt%Mg.

4.2. Experimental method

Ag/Al alloys with various Al content (0.50, 0.75, 1.00, and 1.25 wt%) are made via powder metallurgy and hardened via an internal oxidation heat treatment in oxygen. The Ag/Al metal powder is created by induction melting and inert gas atomization to a mesh size of ~450. As-atomized Ag/Al powder is then annealed under an argon atmosphere at 600, 650, 700, 725 and 750°C for 45 min to find the suitable annealing temperature for creating single grain

Ag/Al powder. Annealing at 700°C for 4 hours under an argon atmosphere is finally chosen and is performed for all fabricated Ag/Al powder. Note that each powder particle is initially polycrystalline and is converted to a single-grain powder during annealing. The annealed Ag/Al powder is then inserted into Cu extrusion cans which are evacuated, sealed and hot extruded at 650°C. Next, the Cu can is removed from the Ag/Al rod by etching with a ferric chloride solution. The extruded Ag/Al rods are then cold drawn into 0.80 mm Ag/Al alloy wires. Ag/Al alloy sheets are made by rolling the wire. Figure 2-1 shows the step-by-step fabrication process for creating the Ag/Al alloy.

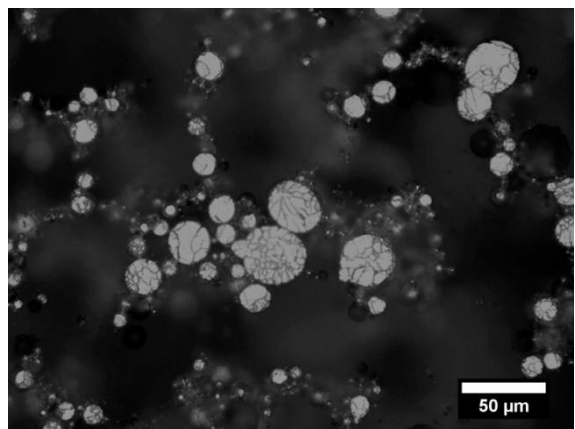
Ag/Al alloy sheets and wires are internally oxidized at 600, 650, 675, 700, 725, 750, 800 and 900 °C for 1, 2, 4 and 8 hours in pure oxygen to form DS Ag/Al alloys. During internal oxidation, heating and cooling are performed under an argon atmosphere; all oxidation procedures are isothermal. Two of the alloy compositions, Ag/0.50wt%Al and Ag/0.75wt%Al, are also heat treated in pure argon at 675°C for 4 hours for subsequent microstructural studies. The Ag/Al alloys behavior is compared with Ag/0.20wt%Mg alloy. Microstructure, mechanical and electrical behavior of the Ag/Al and Ag/0.20wt%Mg alloy samples are tested before and after a heat treatment that simulates the Bi2212 PMP; time-temperature details of the internal oxidation and PMP treatment are presented in Figure 2-4a.

4.3. Results

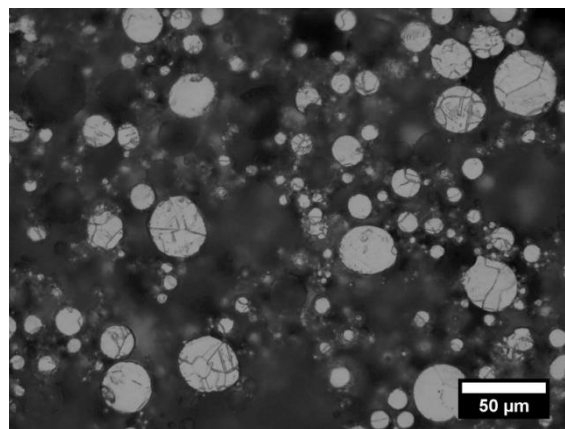
4.3.1. Silver/aluminum alloy synthesis

Particle size analyses on Ag/Al powders indicate $d_{90} < 30 \mu\text{m}$ and $d_{50} < 16 \mu\text{m}$, where d_{90} and d_{50} are defined as the diameters such that 90% and 50% of the particles are smaller than these values. Figure 4-1 shows the grain structure of the polycrystalline as-atomized Ag/0.50wt%Al powder pre- and post-annealing at 600, 650, 700, 725 and 750°C for 45 min. The annealing treatment promotes Ag grain growth and converts the polycrystalline Ag/Al powder into nearly single grain powder particles. As seen in Figure 4-1, higher annealing temperatures produce a greater fraction of single grain particles. Above 700°C, however, the powder begins to sinter. Sintering is detrimental at this stage of the processing, so a cycle of 700°C for no more than 4 hours is utilized. Figure 4-1g shows the grain structure after this annealing treatment. Although there are a few polygrain particles, the fraction of single grain particles is high. Subsequently, this annealing treatment is used as the standard annealing treatment for all the Ag/Al powders.

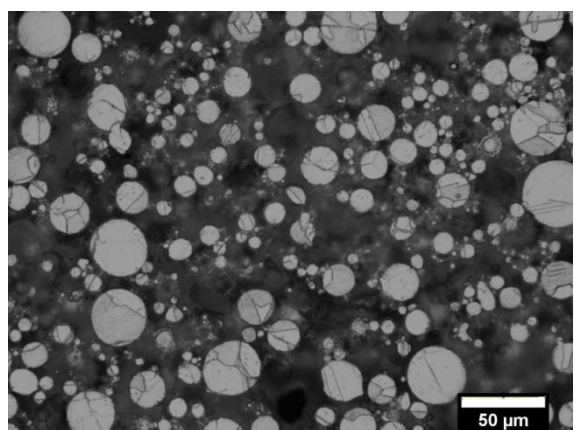
Figure 4-1: Optical micrographs of a) as-atomized Ag/0.50wt% Al powder particles, and the powder annealed under an argon atmosphere at b) 600°C for 45 min, c) 650°C for 45 min, d) 700°C for 45 min, e) 725°C for 45 min, f) 750°C for 45 min and g) 700°C for 4 hours.



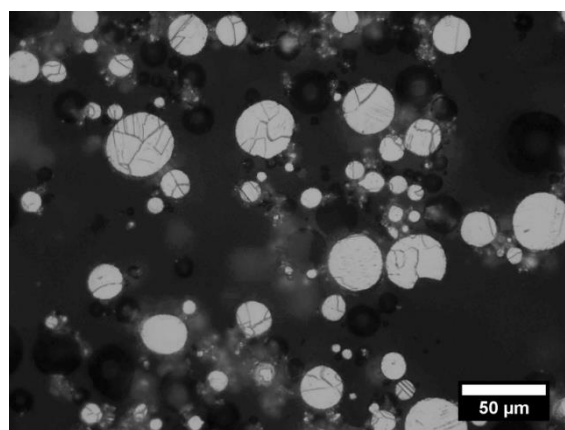
a



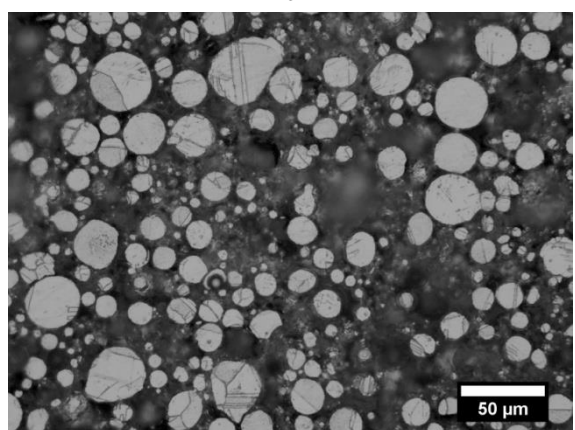
B



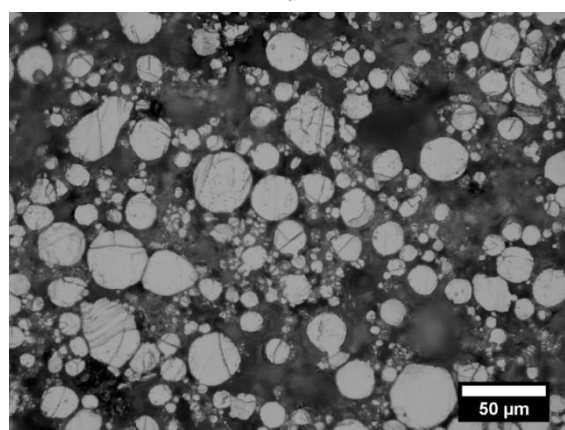
c



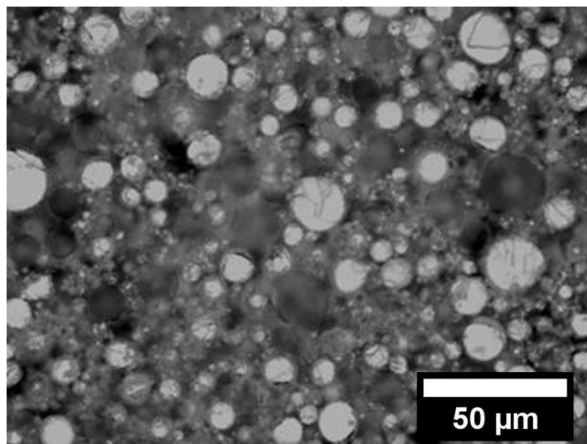
d



e



f



g

4.3.2. Mechanical properties

4.3.2.1. Hardness measurements

Pre-PMP, Ag/0.20wt%Mg has a HVN of 40. Post-PMP in oxygen, the Ag/0.20wt%Mg HVN increases to 116 due to the formation of MgO precipitates [1, 2, 5-7]. Table 4-1 summarizes the HVN for four Ag/Al alloys oxidized at eight different temperatures for 1, 2, 3 and 4 hours. Before oxidation, Ag/0.50wt%Al, Ag/0.75wt%Al, Ag/1.00wt%Al and Ag/1.25wt%Al alloys are soft with HVNs of 55, 60, 68, and 73, respectively. After oxidation, HVN increases by about 250% for all DS Ag/Al alloys. HVN increases with increasing oxidation time for each oxidation temperature studied in detail except for 900 °C. At 900 °C, after 4 and 8 hours of oxidation, HVN decreases due to significant Ag grain growth.

The Ag/Al alloys oxidized at 600, 650, 675 and 700°C show the highest HVN and the HVN values start to decrease at temperature above 700°C. These oxidized samples are selected for PMP heat treatment and investigating their HVN changes post-PMP. Ag grain growth along with size, spacing and distribution of Al₂O₃ precipitates formed at the higher oxidation temperature may cause this HVN decrease [3, 8-10]. Table 4-2 summarizes the HVN results for Ag/0.50wt%Al, Ag/0.75wt%Al, Ag/1.00wt%Al alloys oxidized at 600, 650, 675 and 700°C for 2, 4, and 8 hours pre- and post-PMP. For DS Ag/0.50wt%Al, DS Ag/0.75wt%Al and DS Ag/1.0wt%Al alloys oxidized at 600, 650, 675 and 700°C, the HVN values decreased by nearly 5%, 1%, 3% and 4% post-PMP, respectively. Figure 4-2 summarizes the HVN

values measured for DS Ag/Al alloys oxidized for 4 hours pre- and post-PMP. The DS Ag/0.50wt%Al, DS Ag/0.75wt%Al and DS Ag/1.00wt%Al alloys oxidized at 600, 650, 675 and 700°C, maintain high strength post-PMP, with reductions in HVN values of 5% or less. Thus, after PMP the DS Ag/Al alloys show nearly 50% higher HVN than Ag/0.20wt%Mg.

HVN results for the Ag/0.50wt%Al and Ag/0.75wt%Al alloys heat treated in pure argon at 675°C for 4 hours are tabulated in Table 4-3. These results indicate that for samples heat treated under argon overpressure, the HVN measured pre-PMP is lower than in non-oxidized samples; this is due to Ag grain growth. The formation of Al₂O₃ is prevented by the use of an inert atmosphere, so oxide strengthening is not achieved. The HVN values for samples measured post-PMP after argon annealing are comparable with the internally oxidized ones. The highest strength is achieved, however, for the internally oxidized samples, despite a 4% decrease in HVN post-PMP. In light of this decrease, the internally oxidized post-PMP samples are still stronger in comparison to argon heat treated samples post-PMP due to a higher Ag grain-boundary density.

Table 4-1: HVN for non-oxidized and internally oxidized alloys versus oxidation temperatures and times										
Alloy comps.	t (h)	Non-oxidized	600°C	650°C	675°C	700°C	725°C	750°C	800°C	900°C
Ag/0.50 wt% Al	1	55 ± 4	150 ± 8			162 ± 10			158 ± 4	155 ± 3
	2		155 ± 8	173 ± 5	172 ± 6	170 ± 2	170 ± 5	168 ± 5	157 ± 4	148 ± 5
	4		161 ± 9	175 ± 8	183 ± 4	176 ± 9	171 ± 5	172 ± 2	160 ± 6	145 ± 3
	8		163 ± 4			175 ± 5			157 ± 7	140 ± 6
Ag/0.75 wt% Al	1	60 ± 3	203 ± 7			202 ± 5			184 ± 8	178 ± 2
	2		209 ± 8	203 ± 4	202 ± 6	207 ± 7	200 ± 6	197 ± 8	187 ± 9	173 ± 4
	4		214 ± 8	207 ± 8	214 ± 7	211 ± 6	198 ± 7	199 ± 3	191 ± 5	172 ± 4
	8		216 ± 8			207 ± 6			197 ± 9	165 ± 4
Ag/1.00 wt% Al	1	68 ± 5	217 ± 5			230 ± 5			201 ± 5	183 ± 2
	2		218 ± 9	217 ± 9	230 ± 6	223 ± 7	214 ± 2	219 ± 7	200 ± 6	175 ± 1
	4		226 ± 7	231 ± 9	231 ± 9	222 ± 6	214 ± 8	220 ± 5	205 ± 6	168 ± 2
	8		235 ± 4			226 ± 5			203 ± 7	166 ± 1
Ag/1.25 wt% Al	1	73 ± 3	238 ± 1			240 ± 7			215 ± 8	185 ± 3
	2		240 ± 2	257 ± 8	242 ± 8	239 ± 9	234 ± 5	233 ± 7	220 ± 2	181 ± 1
	4		244 ± 2	247 ± 9	246 ± 9	238 ± 5	234 ± 7	233 ± 3	221 ± 1	175 ± 2
	8		235 ± 5			244 ± 5			219 ± 2	169 ± 2

Alloy Comp.	t(h)	600°C		650°C		675°C		700°C	
		Pre-	post	pre-	post	pre-	post	pre-	post
Ag/0.50 wt% Al	2	155±8	147 ± 5	173 ± 5	169 ± 7	172 ± 6	168 ± 6	170 ± 2	164 ± 9
	4	161±9	153 ± 4	175 ± 8	176 ± 3	183 ± 4	174 ± 4	176 ± 9	167 ± 5
	8	163±4	154 ± 5	-	-	-	-	175 ± 5	156 ± 6
Ag/0.75 wt% Al	2	209±8	199 ± 9	203 ± 4	203 ± 5	202 ± 6	197 ± 8	207 ± 7	198 ± 7
	4	214 ± 8	207 ± 1	207 ± 8	202 ± 8	214 ± 7	208 ± 5	211 ± 6	197 ± 6
	8	216 ± 8	211 ± 9	-	-	-	-	207 ± 6	201 ± 5
Ag/1.00 wt% Al	4	226 ± 9	220 ± 4	231 ± 9	231 ± 9	231 ± 9	226 ± 8	222± 6	216 ± 6
	8	235 ± 4	231 ± 5	-	-	-	-	226 ± 5	220 ± 2

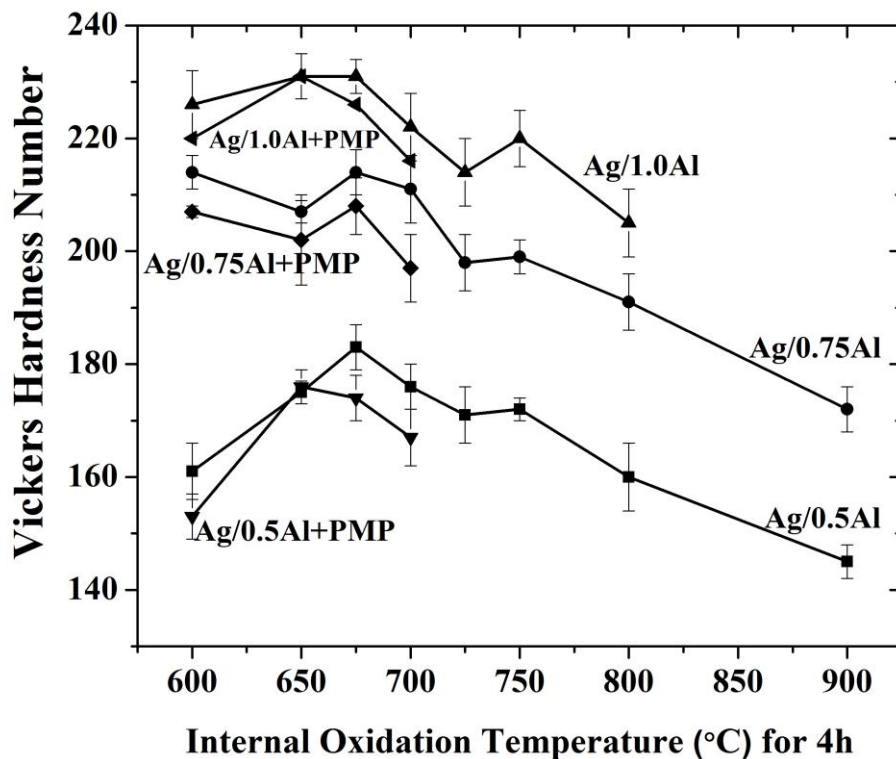


Figure 4-2: HVN versus oxidation temperature (held for 4 hours) for Ag/Al alloys with and without PMP heat treatment.

4.3.2.2. Room temperature tensile behavior

Figure 4-3 compares the RT tensile properties of internally oxidized Ag/0.50wt%Al solid alloy wires pre- and post-PMP at various times and temperatures. The yield strength (YS) and UTS for oxidized wires pre-PMP are presented in Figure 4-3a. The alloy oxidized at 700°C for 4 hours shows the highest YS, 466 MPa, whereas the UTS values are virtually

independent of oxidation time. After PMP, its mechanical strength decreases slightly to a YS of 426 MPa and UTS of 470 MPa (Figure 4-3b), but the El% of this wire increases from 0.8% to 8.0%. Figure 4-3c compares the change in strength for all oxidized samples due to PMP. Although internal oxidation at 700°C for 4 hours results in the highest YS pre- and post-PMP, there is a large decrease in both the YS and UTS due to PMP; thus internal oxidation at 700°C is not beneficial. Alternatively, internal oxidation at 675°C for 4 hours gives significantly more stable mechanical behavior. Prior to PMP, the Ag/0.50wt%Al oxidized at 675°C for 4 hours has a YS of 418 MPa, UTS of 425 MPa and El% of 0.35. Post-PMP, the YS is 415 MPa, UTS increases to 463 MPa and the El% increases to 11%. Figure 4-3d compares the El% of all samples pre- and post-PMP. All DS Ag/0.50wt%Al samples have an elastic modulus of $E \sim 85$ GPa. For comparison, Ag/0.2wt%Mg has an $E \sim 80$ GPa, YS of 310 MPa, UTS of 396 MPa and El% of 22% post-PMP [1].

4.3.3. Microstructural observations

SEM micrographs for the etched microstructures of the Ag/0.50wt%Al alloy sheets heat treated under various conditions are seen in Figure 4-4. The non-oxidized Ag/0.50wt%Al has an average grain size of ~ 3.32 μm . After internal oxidation, the grain size increases to ~ 5.72 μm . The Ag/0.50wt%Al alloy which is PMP treated without an oxidation treatment shows a grain size of ~ 5.58 μm . Finally, the internally oxidized and PMP-treated Ag/0.50wt%Al has a grain size of 5.28 μm . The Ag/0.50wt%Al alloy sheet heat treated in pure argon at 675°C for 4 hours pre-PMP shows a grain size of ~ 7.20 μm . The samples heat treated in argon have the

largest grain size since the oxide formation is prohibited under an inert atmosphere. Similar results are obtained with the microstructure of the Ag/0.75wt%Al alloy.

Figure 4-5 illustrates ion channeling contrast images for DS Ag/0.50wt%Al alloy that is internally oxidized at 675°C for 4 hours. The tiny dark gray color particles are small Al₂O₃ precipitates. They are seen within grains and on grain boundaries. The dark and light gray color bands are twins and stacking faults in the FCC matrix of Ag.

Table 4-3: Comparison of HVN for Ag/0.50wt%Al and Ag/0.75wt%Al alloys heat treated in various atmospheres						
Alloy Composition	Non-oxidized		Heat treated in argon at 675°C for 4 hours		Internally oxidized at 675°C for 4 hours	
	Pre-PMP	Post-PMP	Pre-PMP	Post-PMP	Pre-PMP	Post-PMP
Ag/0.50wt% Al	55 ± 4	160 ± 3	44 ± 1	168 ± 6	183 ± 4	174 ± 4
Ag/0.75wt% Al	60 ± 3	200 ± 2	45 ± 8	202 ± 9	214 ± 7	208 ± 5

4.3.4. Electrical resistivity

The electrical resistivity as a function of temperature is presented in Figure 4-6. The non-oxidized Ag/0.50wt%Al and Ag/0.75wt%Al alloys show the highest resistivity at low temperature. The resistivity decreases after both internal oxidation and PMP for Ag/Al

alloys. Post-PMP, the Ag/0.50wt%Al and Ag/0.75wt%Al alloys show 85% and 50% lower resistivity than Ag/0.20wt%Mg at room temperature. Furthermore, the Ag/0.50wt%Al alloy has comparable resistivity to Ag/0.20wt%Mg for $T < 55$ K post-PMP and shows much lower resistivity than Ag/0.20wt%Mg at $T > 55$ K. The Ag/0.75wt%Al alloy shows slightly higher resistivity than Ag/0.20wt%Mg alloy at $T < 110$ K, but it has much lower resistivity than Ag/0.20wt%Mg at $T > 110$ K.

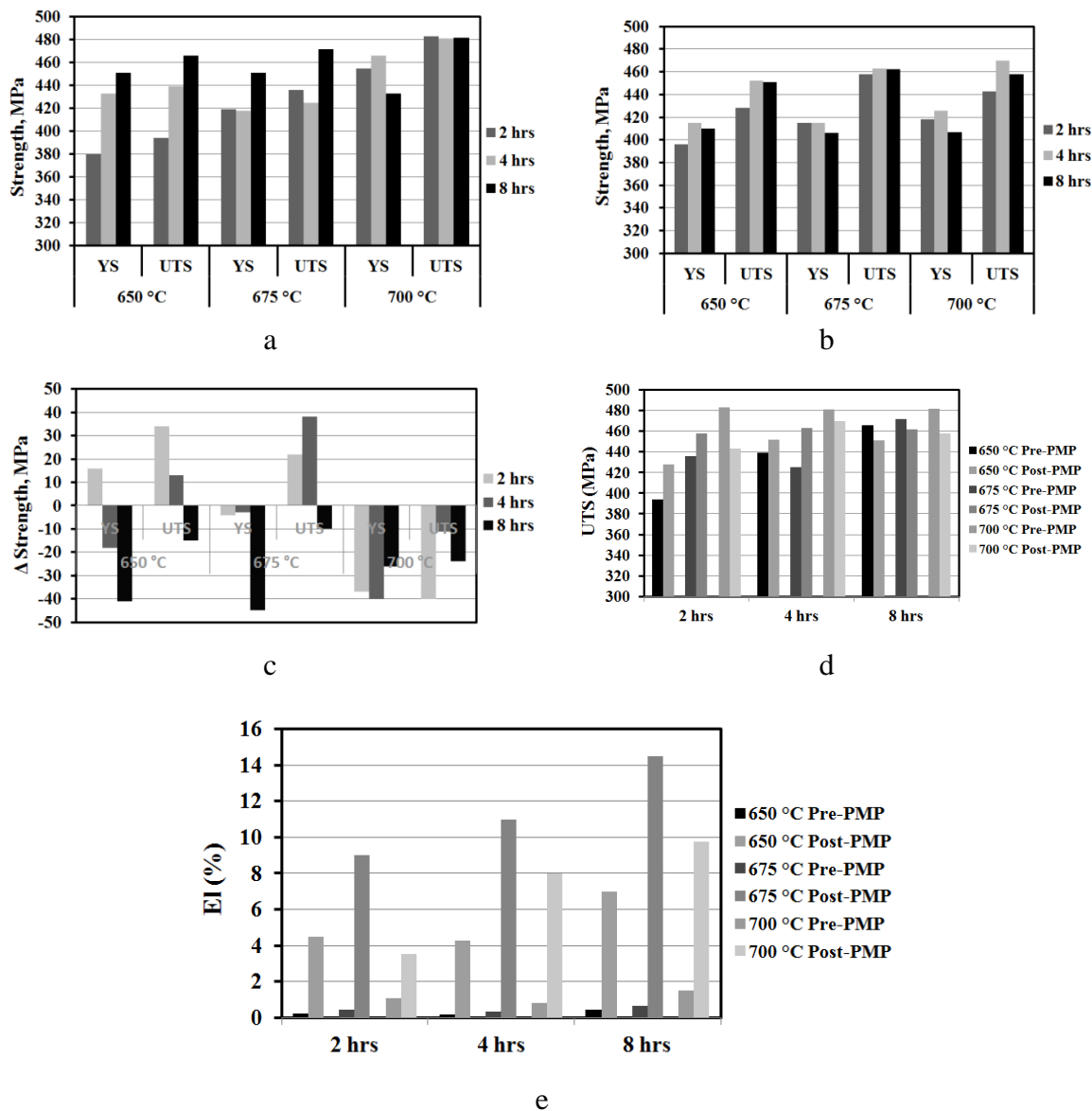


Figure 4-3: RT tensile data for Ag/0.50wt%Al solid alloy wires. a) YS and UTS after internal oxidation in pure oxygen, b) YS and UTS post-PMP for internally oxidized alloy wires, c) strength changes for DS Ag/0.50wt%Al alloy wire during PMP, d) a comparison of UTS for internally oxidized alloy wires pre- and post-PMP, and e) a comparison of El% for internally oxidized alloy wires pre- and post-PMP.

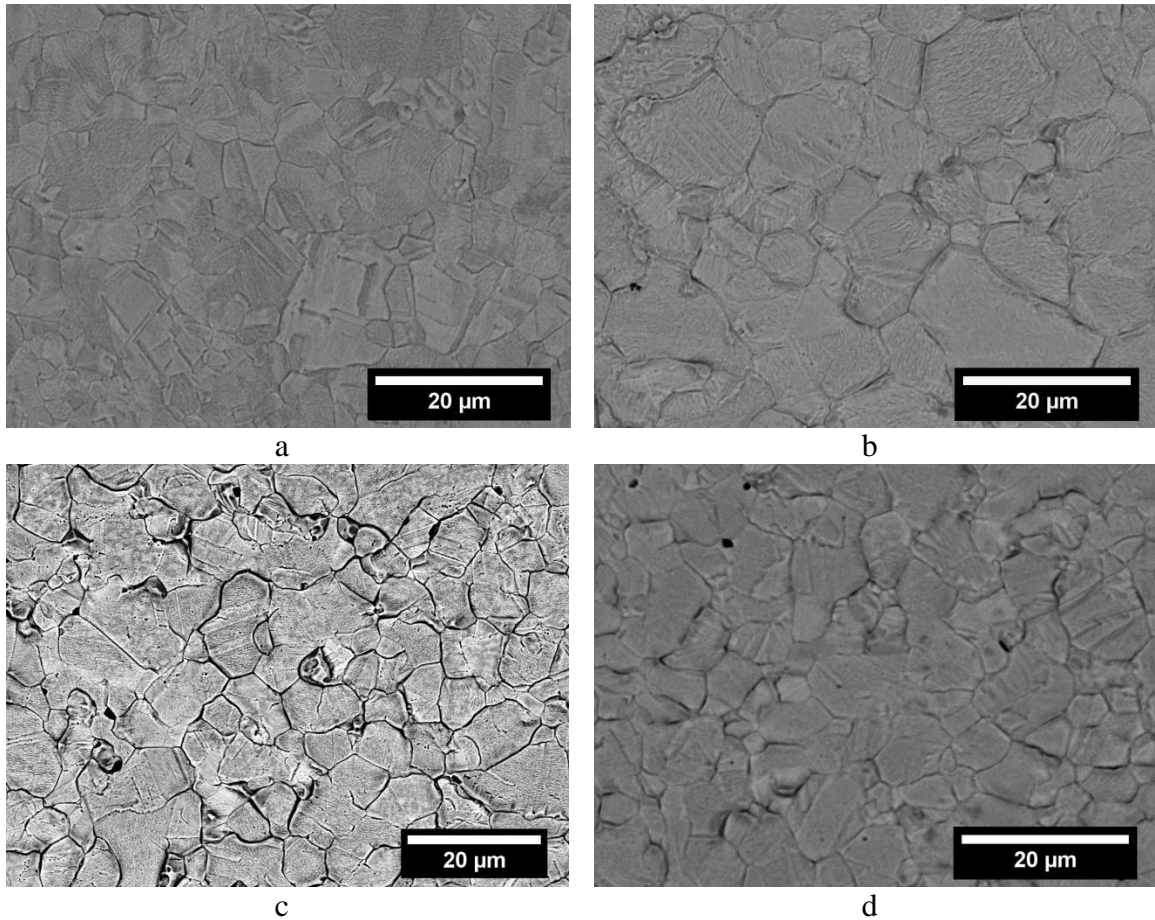


Figure 4-4: SEM images of the grain structure of the Ag/0.50wt%Al alloy after various heat treatments: a) non-oxidized (HVN of 55 and grain size of 3.32 μm), b) internally oxidized at 675°C for 4 hours (HVN of 183 and grain size of 5.72 μm), c) non-oxidized alloy post-PMP (HVN of 160 and grain size of 5.58 μm), and d) oxidized alloy post-PMP (HVN of 174 and grain size of 5.28 μm). Similar results are obtained with the microstructure of the Ag/0.75wt%Al alloy.

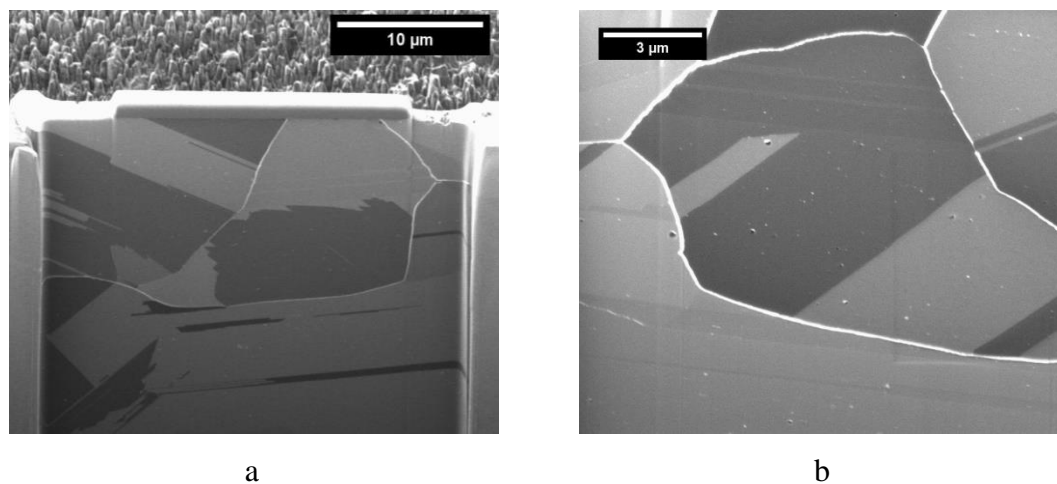


Figure 4-5: a) Low and b) higher magnification ion channeling contrast micrographs showing the dispersion of nanosize Al₂O₃ precipitates in the Ag matrix for the DS Ag/0.50wt%Al alloy oxidized at 675°C for 4 hours. The dark and light gray color bands/stripes are twins in the Ag matrix. The white and occasionally-black precipitates are Al₂O₃.

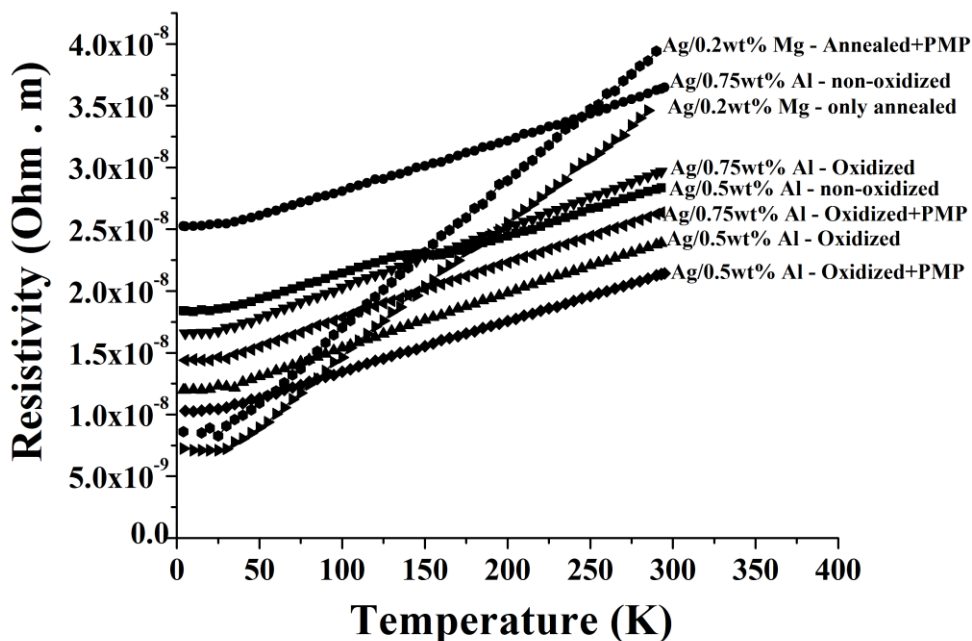


Figure 4-6: Electrical resistivity versus temperature for Ag/0.50wt% Al, Ag/0.75wt% Al and Ag/0.20wt% Mg alloys pre- and post-PMP.

4.4. Discussion

For DS Ag/Al alloys, microstructural parameters including Ag grain size and Al_2O_3 precipitate quantity, spacing and size, affect the mechanical and electrical properties. A polycrystalline Ag/Al alloy with small, equiaxed grains contains a higher grain boundary density than a coarse grain structure. Grain boundaries are obstacles to dislocation motion, so changing the grain size influences dislocation movement and thus the YS. In general, Al_2O_3 precipitates harden the Ag matrix. A dispersion of fine Al_2O_3 precipitates results in a fine

grain microstructure that is resistant to softening during PMP. In the Ag matrix, grain boundaries are preferential diffusion paths for oxygen and promote Al_2O_3 precipitate nucleation. Thus, grain boundary precipitates tend to be larger than those within the grains and have higher mobility, coarsening rapidly during PMP. This destabilizes the oxide precipitate distribution and causes a loss of strength [1]. Thus, small and uniformly dispersed Al_2O_3 precipitates are beneficial for mechanical properties. Note that 4 hours of annealing of the Ag/Al powder at 700°C promotes grain growth and converts the polycrystalline Ag/Al powder into a single grain. By reducing the grain boundary density in the Ag/Al powders, fewer grain boundary Al_2O_3 precipitates form during subsequent internal oxidation and the DS Ag/Al alloy retains its fine grain size and high HVN post-PMP. Ag/Al alloys oxidized at higher temperatures exhibit larger grain size. Furthermore, as seen in Table 4-1, for alloys that are oxidized at temperatures higher than 725°C , the HVN decreases gradually and the alloy becomes softer; this is due to rapid Ag grain growth at higher temperatures. In addition, size, spacing and distribution of Al_2O_3 precipitates formed at the higher oxidation temperature may cause the HVN decrease.

Comparing the non-oxidized sample in Figure 4-4a to those in Figure 4-4(b-d), the effect of Al_2O_3 precipitate formation on the HVN of DS Ag/0.50wt%Al alloy becomes apparent. The most important effect is that the alloy retains its fine grain structure after internal oxidation and PMP. The non-oxidized alloy is soft, but after oxidation, regardless of PMP, the grain size increases from $\sim 3.32 \mu\text{m}$ to $\sim 5.5 \mu\text{m}$. The oxide precipitates play an important role in

impeding dislocation movement and initial grain growth is observed until impeded by oxide precipitate formation. When subject to PMP, the oxidized DS Ag/0.50wt%Al alloy does not show grain growth and a slight decrease in HVN is observed, indicative of precipitate coarsening. Similar results are obtained with the microstructure and HVN of the Ag/0.75wt%Al alloy.

In addition to size and distribution, the stability of Al_2O_3 precipitates during internal oxidation and hence the strength of the DS Ag/Al alloy post-PMP is dependent on the temperature and time of the oxidizing treatment. A larger than expected decrease in strength and HVN is observed for the DS Ag/0.50wt%Al alloy oxidized using a non-optimized internal oxidation treatment [1]. This is likely due to incomplete oxidation of Ag/Al powders or inappropriate internal oxidation treatment time, both of which result in excess oxygen in the microstructure. Excess oxygen causes rapid Al_2O_3 precipitate coarsening post-PMP and decreases the alloy strength and HVN [1]. In a review of internal oxidation of Ag/Al alloys, Meijering [11] stated that a completely oxidized sample would decrease in hardness to a lesser extent than a partially oxidized one. For DS Ag/0.50wt%Al alloy wire processed with a non-optimized internal oxidation treatment, the highest YS and UTS are reported to be 207 and 249 MPa, respectively [1]. Through optimization of the oxygenation process, the DS Ag/0.50wt%Al alloy maintains a high YS and UTS post-PMP, improving by approximately 100%.

Electrical resistivity is a measure to show the existence of a second phase, e.g. oxide precipitates. Internal oxidation of Ag/Al alloys decreases the electrical resistivity which is interpreted to be due to the formation of Al_2O_3 oxide precipitates, therefore resulting in a purer Ag matrix. High resistivity of DS Ag/Al alloys indicates that the Al_2O_3 oxide dispersion is very fine, being more like Al/O clusters than well-defined oxide precipitates [10-13]. The non-oxidized Ag/Al sample consists of a solid solution of Al in the Ag matrix. Both Ag and Al have a face-centered cubic crystal structure with slightly different lattice parameters. Substitution of Al in Ag positions in the structure creates lattice distortions and strain field centers in the microstructure. These centers have the potential for both electron and phonon scattering and hence increase the resistivity. Higher alloying content, such as Ag/0.75wt%Al, increases the resistivity as well.

In solid solution alloys; before internal oxidation heat treatment, Al and Mg elements present in the Ag matrix act as scattering centers for electrons resulting in high resistivity and their removal from matrix as oxide precipitates is expected to result in a resistivity decrease, not an increase. This is the case for Ag/Al alloys after oxidation and post-PMP, but the post-PMP Ag/0.20wt%Mg alloy resistivity increases compared to annealed Ag/0.20wt%Mg (Figure 4-6). This anomalous resistivity increase is due to the formation of small MgO clusters with excess oxygen [5, 8, 14].

4.5. Summary

The fabrication, processing and properties of DS Ag/Al alloys as a potential sheath material for Bi2212 RW are studied. The Ag/Al alloy with various Al content is made via powder metallurgy and internally oxidized. The mechanical, microstructural and electrical properties of Ag/Al alloy at various conditions is measured and compared pre- and post-PMP. The internal oxidation heat treatment is optimized to maximize the strength and modulus of DS Ag/Al alloy post-PMP. The Ag/Al alloy oxidized at 675-700°C for 4 hours gives the highest tensile strength and HVN post-PMP. The HVN, tensile and grain size measurements show that the alloy can retain its fine grain size and strength during PMP treatment in oxygen. Compared to Ag/0.20wt%Mg, the post-PMP mechanical properties are significantly increased.

4.6. References cited

- [1] A. Kajbafvala, *et al.*, "Dispersion-Strengthened Silver Alumina for Sheathing Bi₂Sr₂CaCu₂O_{8+x} Multifilamentary Wire," *IEEE Transactions on Applied Superconductivity*, vol. 22, p. 8400210, Feb 2012.
- [2] R. E. Koritala, *et al.*, "Microstructure and mechanical properties of internally oxidized Ag/1.12 at.% Mg," *AIP Conference Proceedings*, vol. 614, pp. 768-776, 2002.

- [3] B. Tian, *et al.*, "Microstructure and properties at elevated temperature of a nano- Al_2O_3 particles dispersion-strengthened copper base composite," *Materials Science and Engineering: A*, vol. 435–436, pp. 705-710, 2006.
- [4] A. Gatti and R. Fullman, "A Study of the Recrystallization Kinetics and Tensile Properties of an Internally Oxidized Solid-Solution Aluminum-Silver Alloy," *Trans. AIME*, vol. 215, pp. 762-269, 1958.
- [5] B. C. Prorok, *et al.*, "Oxygen diffusion and internal oxidation of Mg in Ag/1.12at.%Mg," *Physica C: Superconductivity*, vol. 370, pp. 31-38, 2002.
- [6] B. C. Prorok, *et al.*, "Hardness and microstructure of internally oxidized silver alloys," *IEEE Transactions on Applied Superconductivity*, vol. 10, pp. 1178-1181, 2000.
- [7] M. O. Rikel and W. Goldacker, "Kinetics and mechanism of low-temperature internal oxidation of Ag-2 and 4 at.% Mg alloys," *Journal of Materials Research*, vol. 14, pp. 2436-2445, Jun 1999.
- [8] J. Takada, *et al.*, "Internal oxidation of dilute silver alloys," *Oxidation of Metals*, vol. 37, pp. 13-22, 1992/02/01 1992.
- [9] J. Koo and D. Yoon, "The dependence of normal and abnormal grain growth in silver on annealing temperature and atmosphere," *Metallurgical and Materials Transactions A*, vol. 32, pp. 469-475, 2001/03/01 2001.

- [10] P. R. Swann, *et al.*, "Aluminum-Oxygen Clusters in Internally Oxidized Silver-Aluminum Alloys," *Transactions of the Metallurgical Society of AIME*, vol. 230, pp. 1306-1309, 1964.
- [11] J. L. Meijering, *Advances in Materials Research* vol. 5: John Wiley & Sons, 1971.
- [12] G. Nihoul and A. Charai, "Theoretical study of phase contrast images for small coherent precipitates inside a matrix," *Philosophical Magazine A*, vol. 52, pp. 407-418, 1985/09/01 1985.
- [13] L. Guobin, *et al.*, "Fabrication of the nanometer Al₂O₃/Cu composite by internal oxidation," *Journal of Materials Processing Technology*, vol. 170, pp. 336-340, 2005.
- [14] B. M. Semega, *et al.*, "Mechanical properties of internally oxidized silver alloys," *Journal of Alloys and Compounds*, vol. 188, pp. 268-271, 1992.

CHAPTER 5

Step III: $\text{Bi}_2\text{Sr}_2\text{CaCu}_2\text{O}_{8+x}$ round wires with high-strength oxide dispersion strengthened Ag/Al alloy sheath

5.1. Background and motivation

In the previous chapter, the fabrication, processing and properties of Ag/Al alloys with various Al content are studied. The Ag/Al alloys are made via powder metallurgy and hardened by an internally oxidation heat treatment. The internal oxidation is optimized to maximize the strength of the dispersion-strengthened (DS) Ag/Al alloy after the PMP heat treatment. The Ag/Al alloys oxidized at 675-700°C for 4 hours gave the highest tensile strength and Vickers micro-hardness (HVN) after PMP. The HVN, tensile test and grain size measurements showed that the DS Ag/Al alloy retained its fine grain size and strength after the PMP heat treatment in oxygen.

This chapter reports on the behavior of double-restack Bi2212/Ag/AgAl multifilamentary round wire (RW) conductors made by various Ag/Al alloy compositions. Microstructure, mechanical and electrical properties are studied and compared in various conditions during processing including as-drawn (green wire and non-oxidized), after internal oxidation, and after PMP heat treatment. The Bi2212/Ag/AgAl wire behavior is compared with that of a double-restack Bi2212/Ag/AgMg wire.

5.2. Experimental method

Double-restack Bi2212 multifilamentary wires are fabricated using the powder-in-tube method. Ag/Al alloys with various Al content (0.50, 0.75, 1.00, and 1.25 wt%) are made by powder metallurgy and used as the outer alloy sheath material; pure Ag is used as the primary and first restack sheath. All Bi2212 conductors are made using the same Nexans precursor powder. Table 5-1 summarizes the wire specifications. After deformation, the Bi2212/Ag/AgAl wires are internally oxidized in 1 bar flowing 100% oxygen in a quartz tube furnace at 675°C for 4 hours to form the DS Ag/Al alloys in the outer sheath; this internal oxidation heat treatment time and temperature are chosen based on our previous Ag/Al alloy processing optimization in chapter 4. Note that heating and cooling are performed under an argon atmosphere. All conductors are heat treated using an identical PMP heat treatment; the PMP time-temperature profile is presented in Figure 2-4. Thus, the PMP time-temperature profile is not optimized separately for each alloy. Microstructures, mechanical and transport properties of Bi2212 wires are studied. A double restack Bi2212/Ag0.20Mg with the same geometry is used for comparison. The SC % is measured to be ~23% for Bi2212/AgAl wires and ~27% for Bi2212/Ag0.20Mg wire.

Microstructure, mechanical and electrical properties of all Bi2212/ AgAl wires and the reference Bi2212/Ag0.20Mg wire is studied at various conditions, including green wire (as-drawn), after internal oxidation only, after PMP heat treatment only, and after an internal oxidation and PMP heat treatment. Combined high resolutions transmission electron

microscope (HRTEM) and high-angle annular dark-field scanning transmission electron microscope (HAADF/STEM) equipped with an energy dispersive x-ray spectrometer (EDS) are used to investigate size, shape and distribution of MgO and Al₂O₃ precipitates.

Table 5-1: Conductors specifications. All wires are double-restack with an outer diameter of 0.8 mm			
Sample code	Inner sheath material	Outer alloy sheath	Average filament size (μm)
Bi2212/Ag0.20Mg	Pure Ag	Ag/0.20wt%Mg	16.0
Bi2212/Ag0.50Al	Pure Ag	Ag/0.50wt%Al	16.5
Bi2212/Ag0.75Al	Pure Ag	Ag/0.75wt%Al	16.3
Bi2212/Ag1.00Al	Pure Ag	Ag/1.00wt%Al	16.4
Bi2212/Ag1.25Al	Pure Ag	Ag/1.25wt%Al	16.0

5.3. Results

5.3.1. Microstructure

5.3.1.1. Grain size measurements

Figure 5-1 shows cross-sectional optical micrographs for all as-drawn (green) wires. Small white areas in Figure 5-1a are the Ag grains within the Ag/0.20wt%Mg outer alloy sheath. In

the Ag/Al alloy sheaths (Figures 5-1 b-e); the Ag grain size is smaller than the resolution limit of the optical microscope. Figure 5-2 shows SEM micrographs of the Ag/0.50wt%Al and the Ag/0.20wt%Mg outer alloy sheaths before PMP; Ag/0.75wt%Al, Ag/1.00wt%Al, and Ag/1.25wt%Al alloy sheaths show grain sizes similar to that of Ag/0.50wt%Al. The Ag/0.20wt%Mg alloy sheath in green wire has an average grain size of 2.35 μm , whereas that of the Ag/Al alloys is about 0.65 μm .

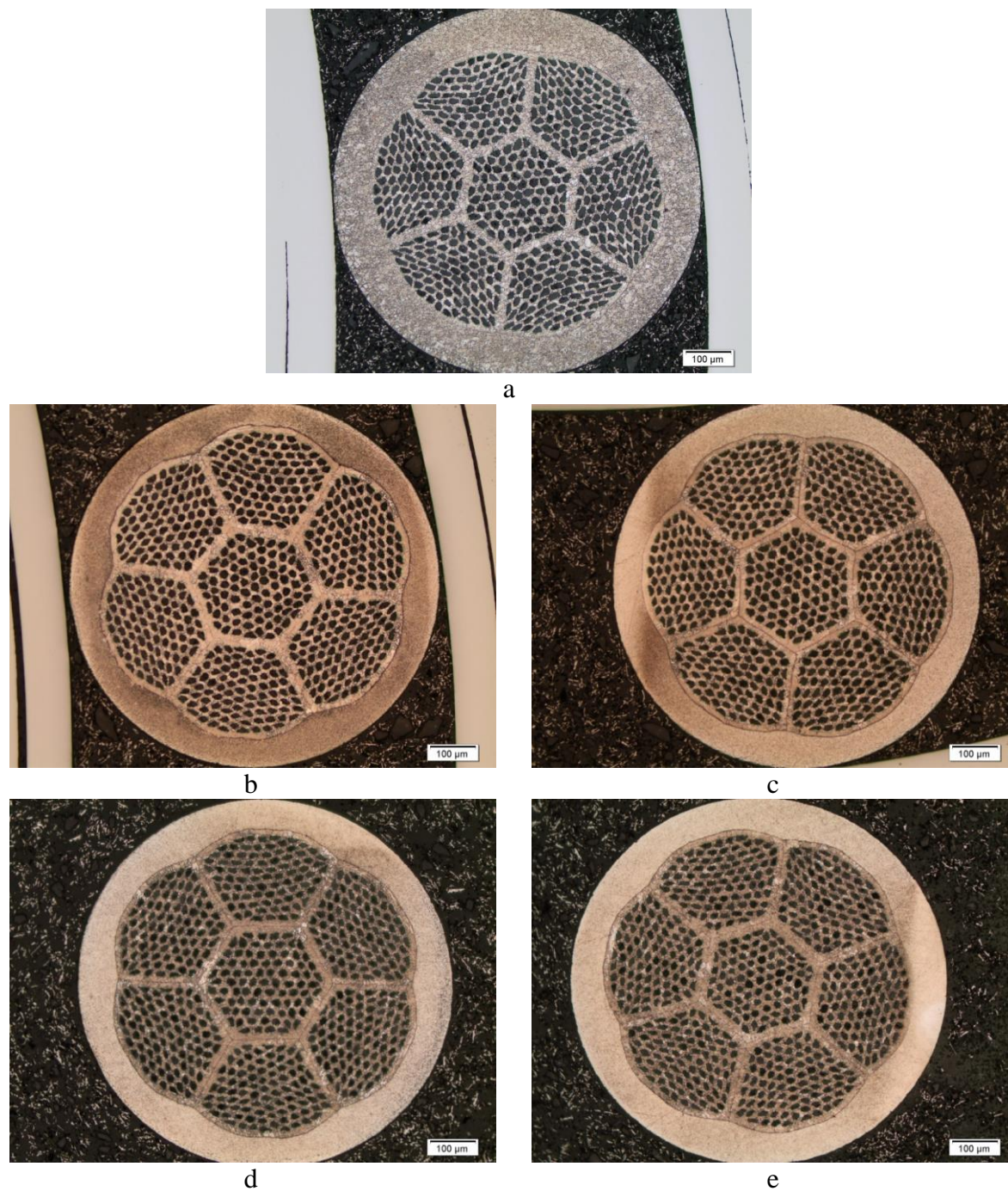


Figure 5-1: Optical micrographs from etched cross-sections of a) Bi2212/Ag0.20Mg, b) Bi2212/Ag0.50Al, c) Bi2212/Ag0.75Al, d) Bi2212/Ag1.00Al, and e) Bi2212/Ag1.25Al green wires.

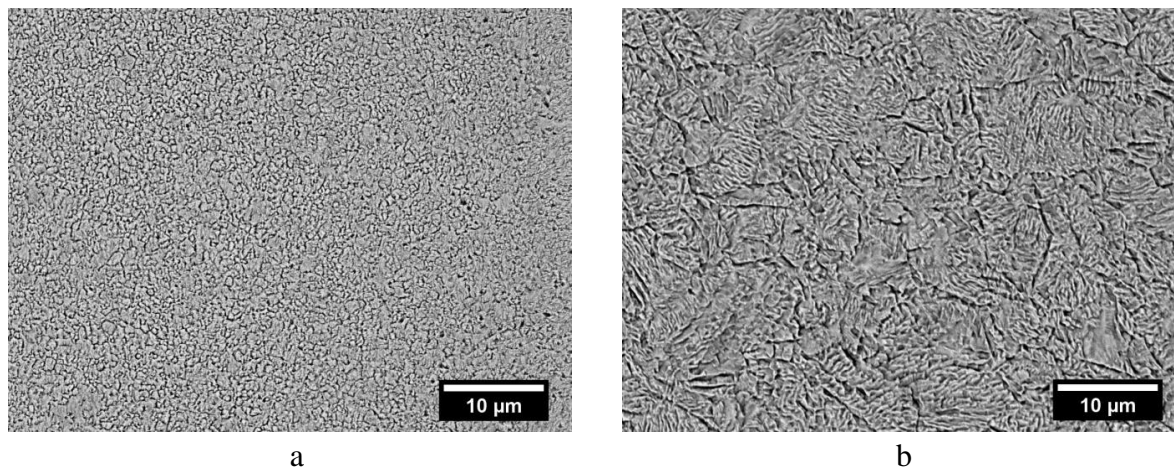


Figure 5-2: SEM micrographs of a) Ag/0.50wt%Al outer alloy sheath in Bi2212/Ag0.50Al, and b) Ag/0.20wt%Mg outer alloy sheath in Bi2212/Ag0.20Mg green wires.

Figure 5-3 illustrates optical micrographs for all Bi2212/AgAl wires after internal oxidation at 675°C for 4 hours. The average grain sizes of the Ag/0.50wt%Al, Ag/0.75wt%Al, Ag/1.00wt%Al, and Ag/1.25wt%Al outer alloy sheathes are 11.7, 11.3, 10.5 and 9.7 μm, respectively. The corresponding wires which are internally oxidized and PMP heat treated have grain sizes of 9.7, 9.5, 8.3, and 8.6 μm, respectively. These are seen in Figure 5-4.

Figure 5-5 shows the optical micrographs for all Bi2212/AgAl and Bi2212/Ag0.20Mg wires after PMP (without prior internal oxidation). All Ag/Al outer alloy sheathes have an average grain size of about 7.5 μm in this condition, whereas the Ag/0.20wt% Mg grain size is nearly 8.2 μm.

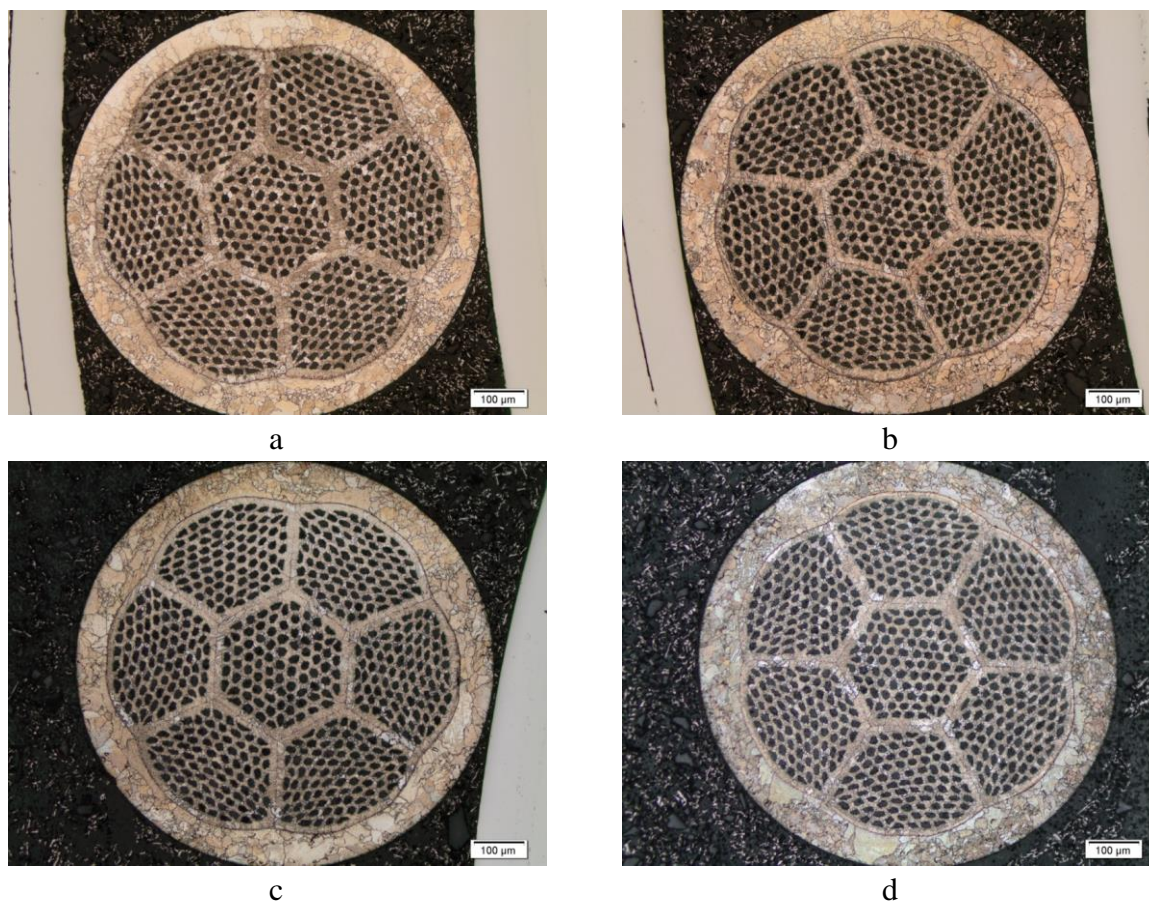


Figure 5-3: Optical micrographs from etched cross-section of a) Bi2212/Ag0.5Al, b) Bi2212/Ag0.75Al, c) Bi2212/Ag1.00Al, and d) Bi2212/Ag1.25Al, internally oxidized at 675°C for 4 hours. The grain size for the Ag/Al outer alloy sheathes of these wires is measured to be 11.7, 11.3, 10.5, and 9.7 μm, respectively.

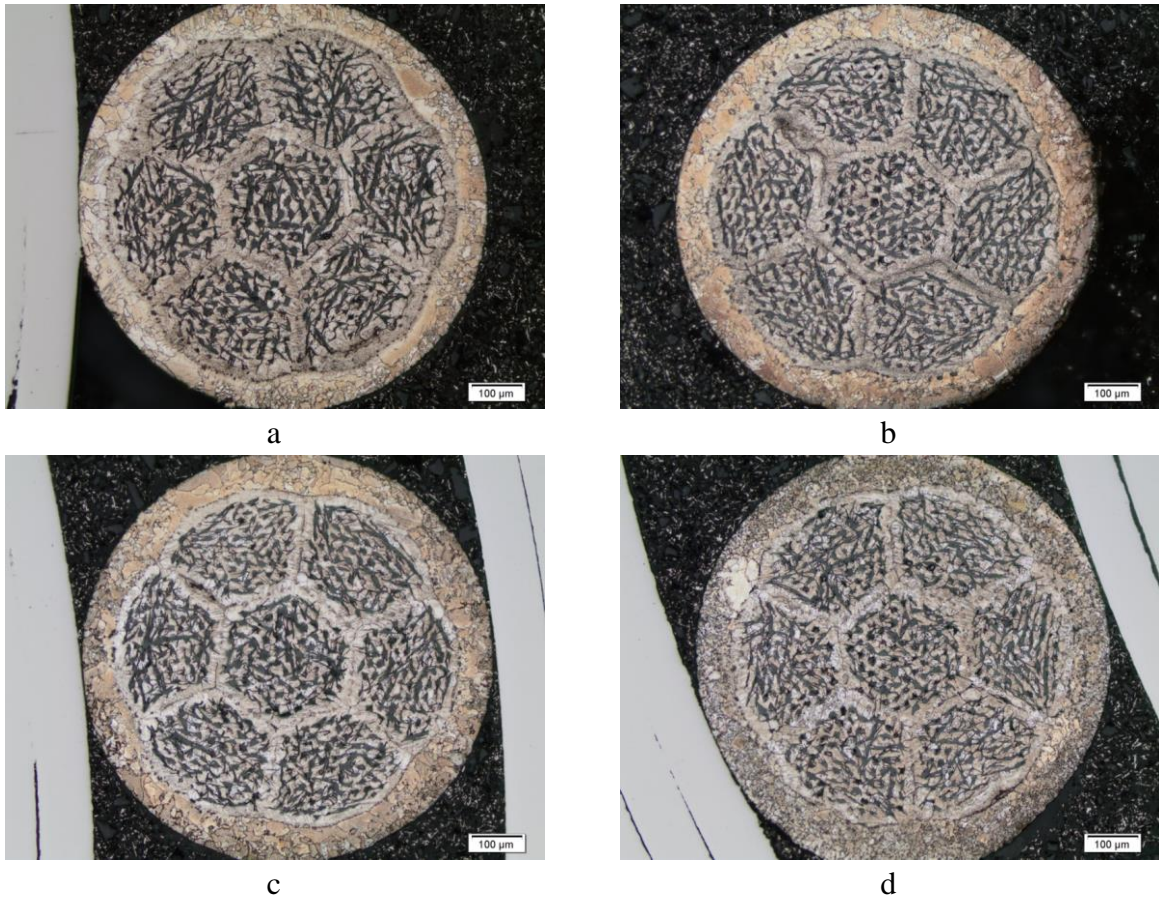


Figure 5-4: Optical micrographs from etched cross-section of a) Bi2212/Ag0.50Al, b) Bi2212/Ag0.75Al, c) Bi2212/Ag1.00Al, and d) Bi2212/Ag1.25Al after internal oxidation and PMP heat treatment. The grain size for the Ag/Al outer alloy sheathes of these wires is measured to be 9.7, 9.5, 8.3, and 8.6 μm , respectively.

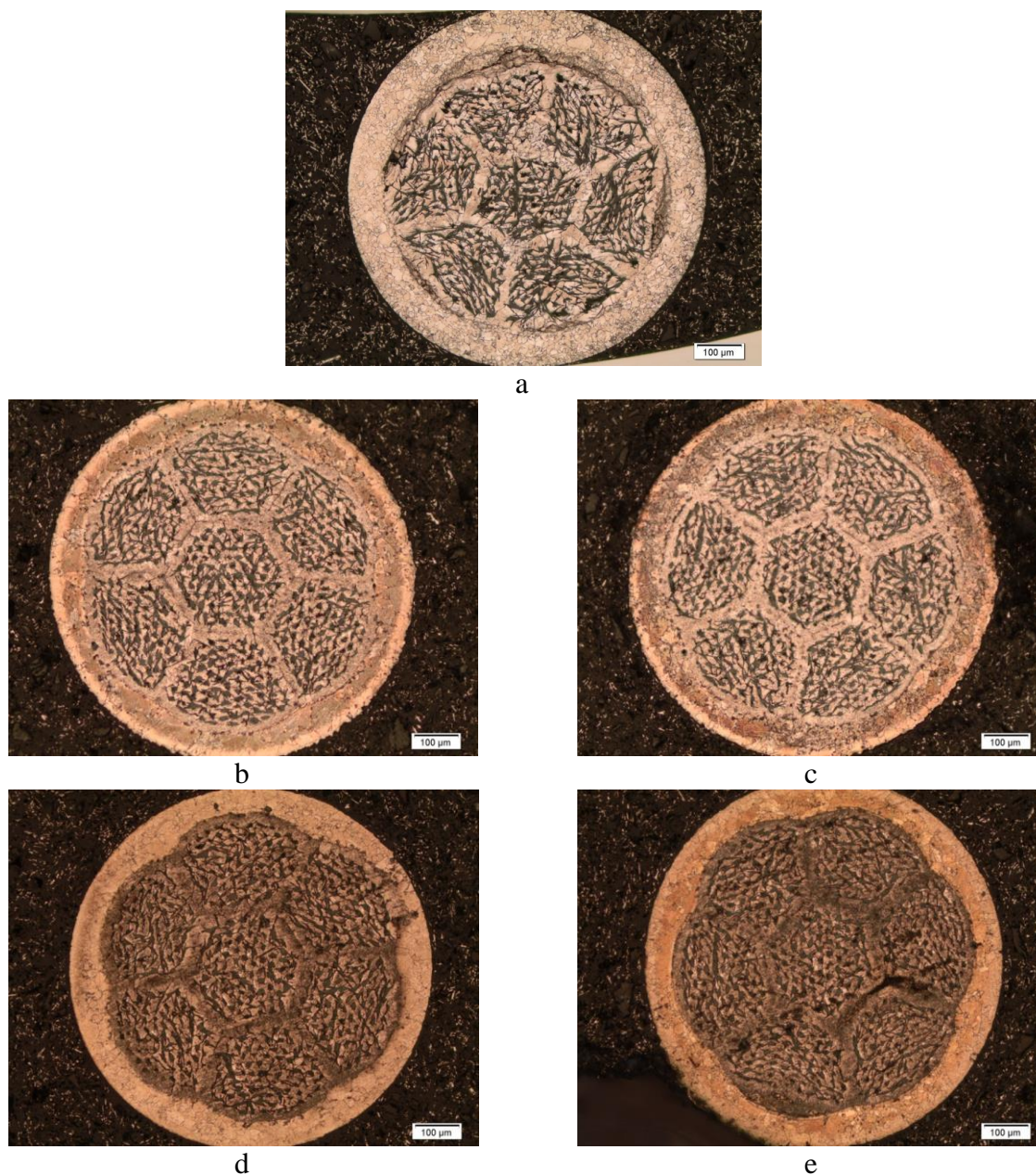


Figure 5-5: Optical micrographs from etched cross-section of a) Bi2212/Ag0.20Mg, b) Bi2212/Ag0.50Al, c) Bi2212/Ag0.75Al, d) Bi2212/Ag1.00Al, and e) Bi2212/Ag1.25Al green wires after PMP. The grain size for the Ag/Al outer alloy sheathes is measured to be 7.6, 7.4, 7.8, and 7.3 μm , respectively. The Ag/0.20wt%Mg outer alloy sheath in Bi2212/Ag0.20Mg has a grain size of $\sim 8.2 \mu\text{m}$.

5.3.1.2. Oxide precipitates size, distribution and chemical composition

A HAADF STEM image is formed only by very high angle, incoherently scattered electrons which their intensity is highly sensitive to variations in the atomic number of atoms (Z) in the sample (Z -contrast image) [1-3]. This type of image shows little or no diffraction contrast, that comes from Bragg scattered electrons and is a typical imaging technique in high resolution transmission electron microscopy (HRTEM). HAADF STEM image intensity is approximately proportional to Z^2 . This is a useful tool for imaging dislocations, precipitates and grain boundary segregations [4]. All of HAADF STEM images in this study are captures along [110] zone axis of Ag.

Figure 5-6a shows HAADF STEM image of the Ag/0.20wt%Mg alloy sheath lifted-out from outer alloy sheath of Bi2212/Ag0.20Mg wire after PMP. The sample contains a few Ag grains with a grain boundary elongating from side to side. Dark spherical precipitates are formed on the Ag matrix grain boundaries. Figure 5-6b and c are higher resolution HAADF STEM micrographs from the area which is highlighted by the box in Figure 5-6a. Figure 5-7 depicts HAADF STEM and HRTEM micrographs of the Ag/0.20wt%Mg alloy sheet after PMP showing dark gray spherical precipitates dispersed in the Ag matrix. The intuitive Z^2 interpretation typically employed in HAADF STEM imaging suggests that the white matrix area contains significantly heavier elements (i.e. Ag) than the darker spherical precipitates. Furthermore, the light contrast around each precipice in Figure 5-7 corresponds to the misfit strain field induced by the precipitates in the Ag matrix [5-7].

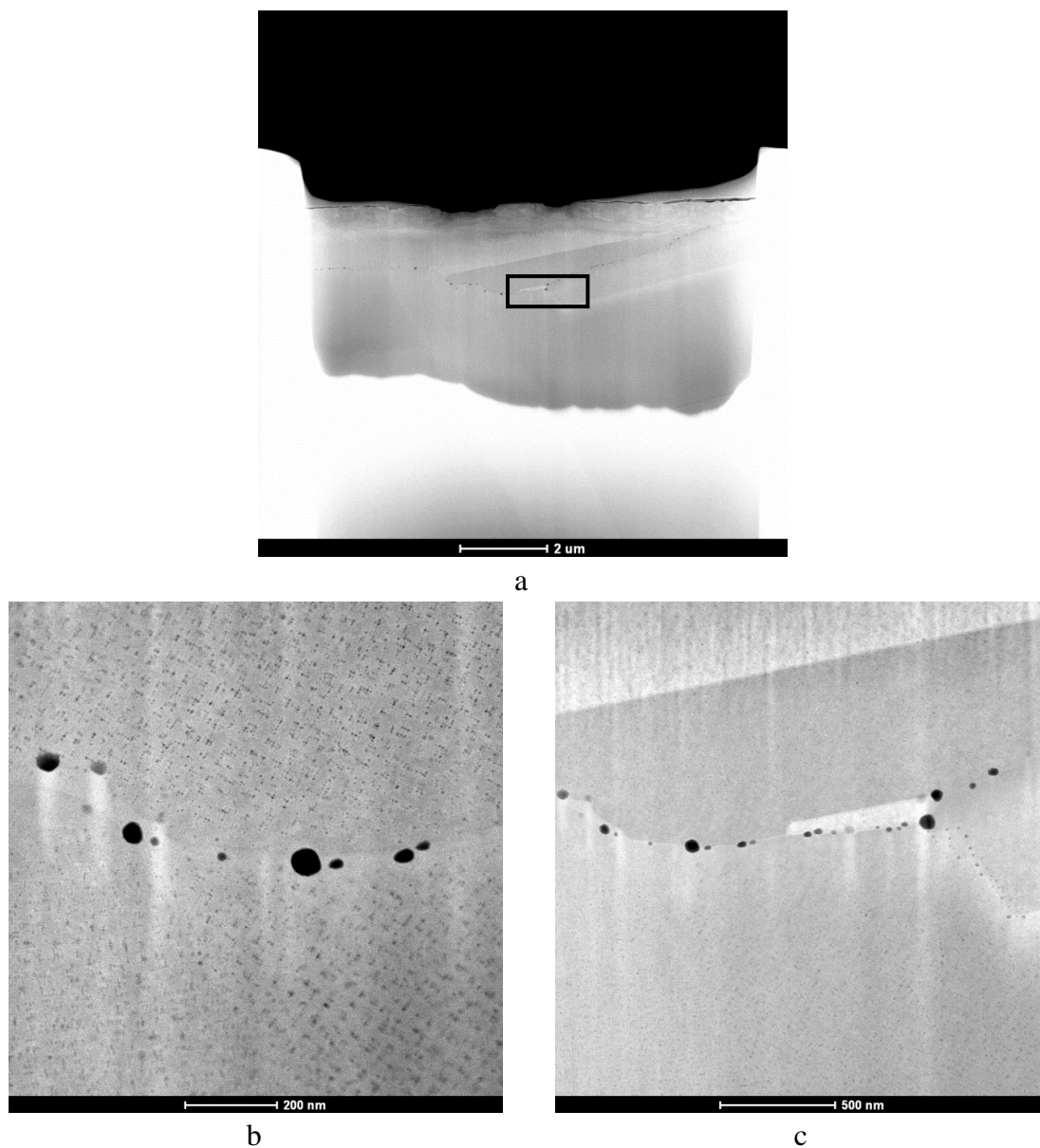
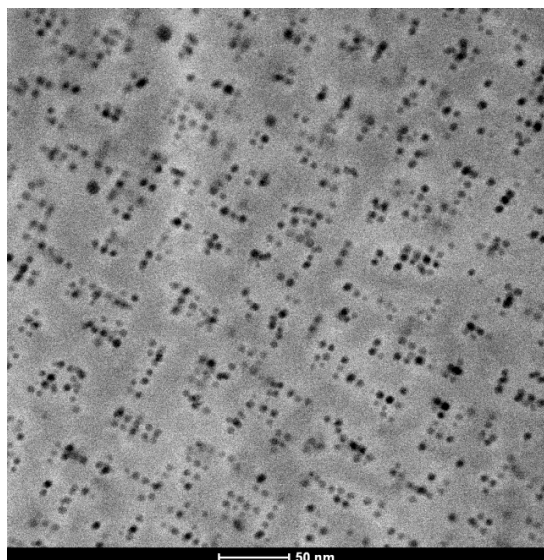
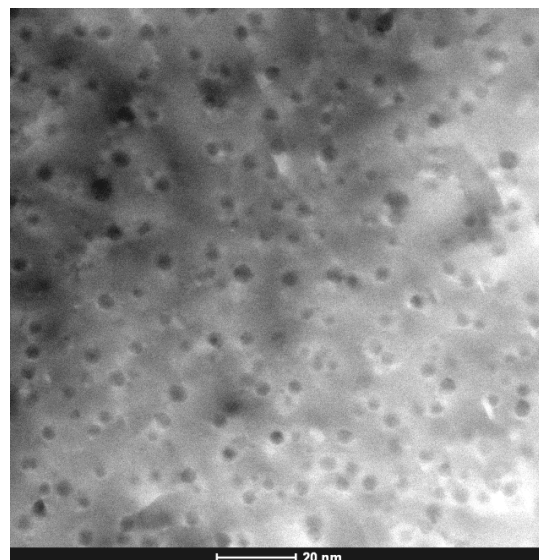


Figure 5-6: HAADF STEM images of the Ag/0.20wt%Mg alloy sheath lifted-out from outer alloy sheath of Bi2212/Ag0.20Mg wire after PMP, a) low magnification, and (b,c) higher magnification micrographs from highlighted box in a.

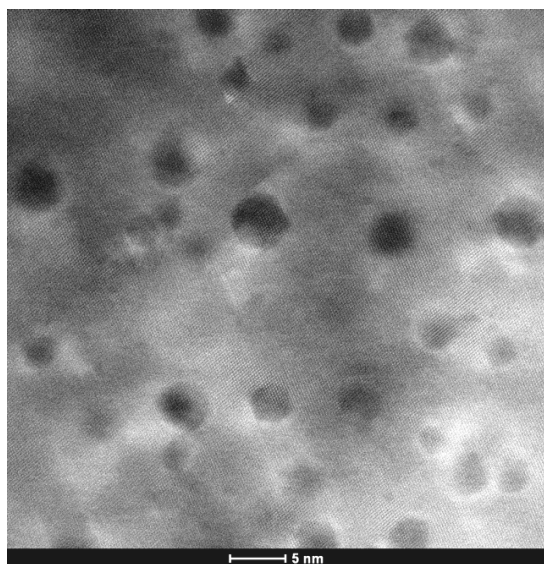
Figure 5-7: HAADF STEM micrographs of the Ag/0.20wt%Mg alloy sheet after PMP heat treatment showing, (a-c) small MgO precipitates dispersed inside the Ag matrix, and d) a higher magnification HAADF STEM image of a single hexagonal shape MgO precipitate having misfit dislocations at its interface with the Ag matrix, (e,f) HRTEM images of Ag/0.20wt%Mg alloy sheet after PMP heat treatment.



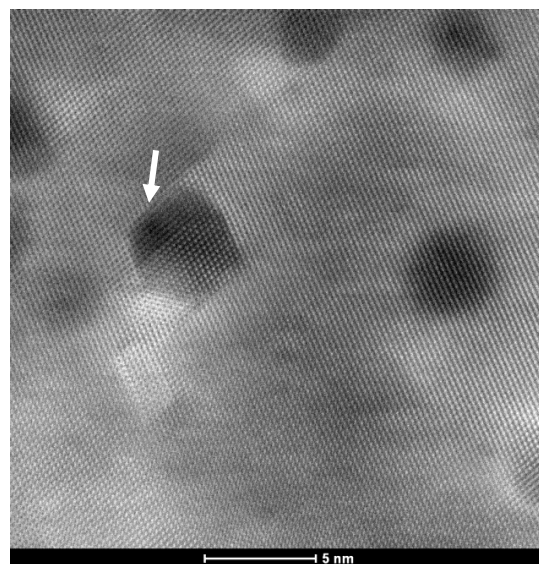
a



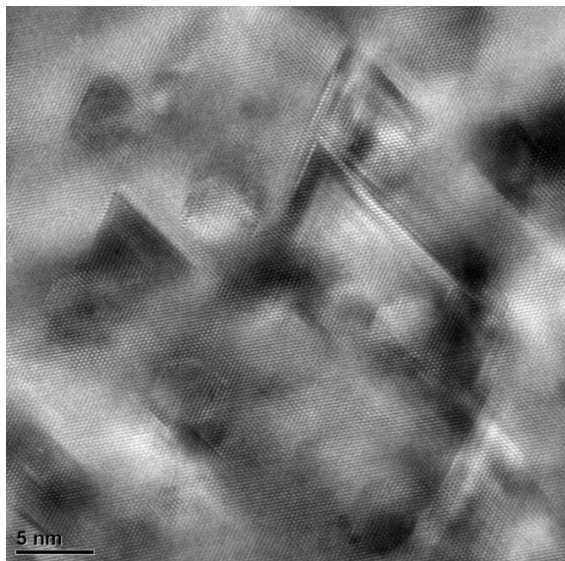
b



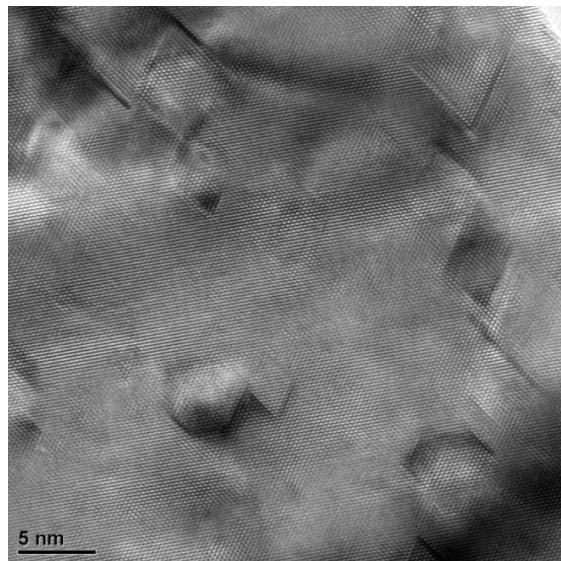
c



d



e



f

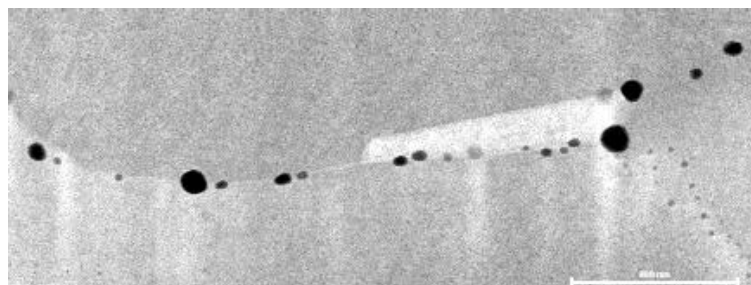
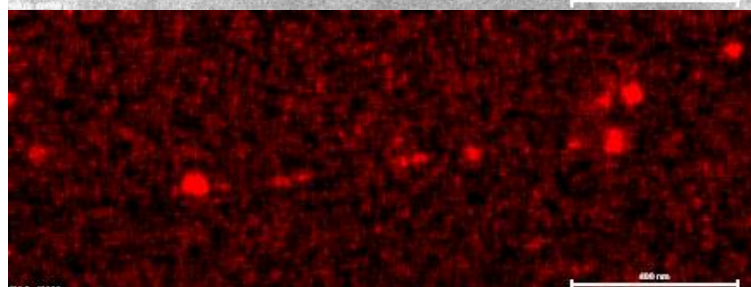
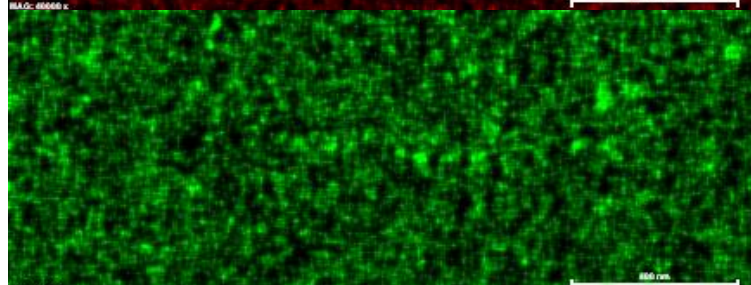
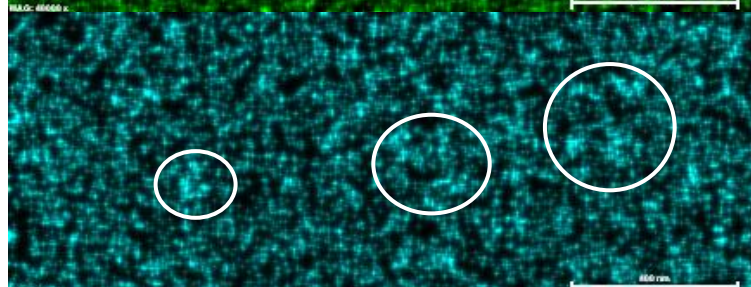
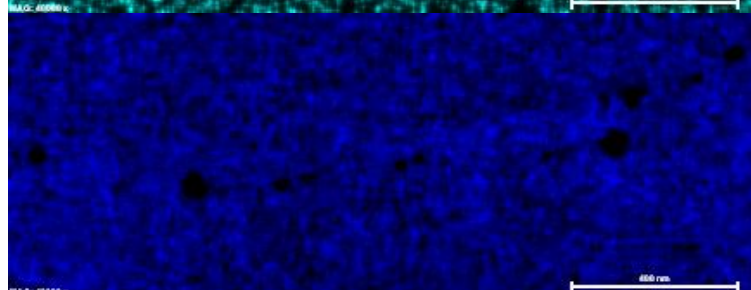
Further analysis of atomic distribution to examine the elemental composition of the formed oxide precipitates required chemical analysis by EDS. The EDS maps present in Figure 5-8a demonstrates the HAADF STEM image along with the Mg, O, Cu and Ag chemical distributions for the precipitates formed on the Ag matrix grain boundaries (highlighted box in Figure 5-6a) and inside Ag grains. Combined micrographs of HAADF STEM and Mg chemical distribution, HAADF STEM, Mg and Ag chemical distributions, and finally Ag and Mg chemical distributions are presented in Figure 5-8b. Figure 5-9 depicts the EDS mappings of dark gray spherical precipitates dispersed in the Ag matrix of Ag/0.20wt%Mg alloy sheet after PMP (presented in Figure 5-7)

Figure 5-8 demonstrates that the large spherical precipitates forming on the Ag grain boundaries are rich in Mg and O and deplete in Ag. The EDS maps of the nanosize spherical precipitates dispersed inside the Ag grains presented in Figure 5-9 also show that the spherical dark gray precipitates are MgO. Furthermore, as can be seen in Figure 5-8a, Cu presents in the Ag/0.20wt%Mg outer alloy sheath of Bi2212/Ag0.20Mg wire and the Cu concentration is slightly higher around large MgO precipitates on the Ag grain boundaries. The Mg available in the Ag/0.20wt%Mg outer alloy sheath of Bi2212/Ag0.20Mg wire reacts with Cu that diffuses from the Bi2212 filament cores into the matrix, forming $Mg_{1-x}Cu_xO$ compounds, depleting Cu from the Bi2212 cores and reducing critical current density (J_c) [8, 9].

The large intergranular MgO precipitates formed on Ag grain boundaries have sizes in the range of ~40-75 nm (Figure 5-6b and c), whereas the spherical MgO precipitates formed inside Ag grains have sizes in the range of ~4-6 nm (Figure 5-7). MgO precipitates with sizes less than 5 nm have coherent interfaces with the Ag matrix [5]. These coherent MgO precipitates exhibit a spherical shape; they induce a matrix isotropic deformation due mainly to the lattice misfit between the Ag and the MgO (~3%). The sphericity of the precipitates evolves towards a polyhedral one as the size increases and misfit interfacial dislocations appear for larger hexagonal-shape MgO precipitates (as seen in Figure 5-7d). The faceting of these MgO precipitates as the one indicated in Figure 5-7d implies formation of precipitates that approach the MgO crystallite. Both Ag and MgO have similar crystal structures of face centered cubic (FCC) and NaCl type, respectively. The interplanar spacing of the (111) planes are 0.242 nm for MgO and 0.235 nm for Ag, respectively. In general, the hexagonal-shape MgO precipitates are mainly faceted along the (111) and the (100) planes. This crystallographic orientation seems to have a lower interfacial Ag/MgO energy [10, 11].

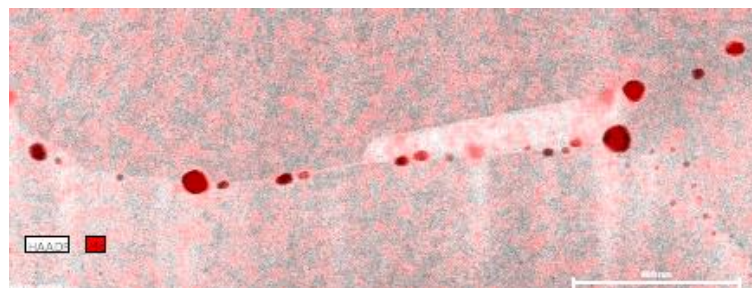
Figure 5-8: a) EDS maps demonstrate the HAADF STEM image along with the Mg, O, Cu, and Ag chemical distributions of the large MgO precipitates formed on the Ag grain boundaries, b) Combined EDS maps with the HAADF STEM image in Figure 8a.

HAADF STEM

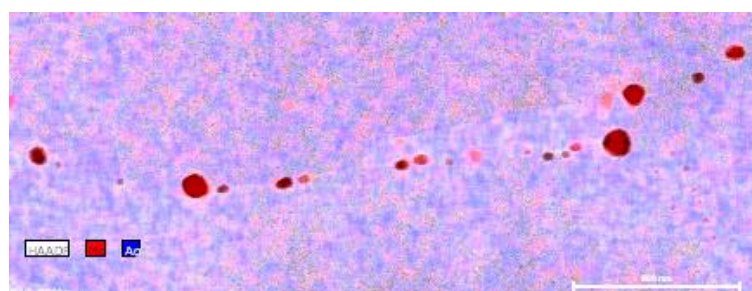
Mg chemical
distributionO chemical
distributionCu chemical
distributionAg chemical
distribution

a

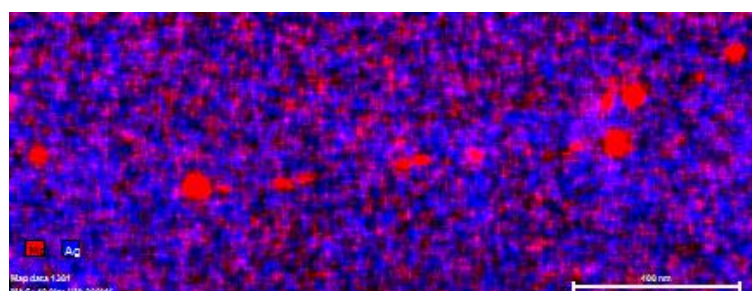
HAADF STEM
&
Mg distribution



HAADF STEM
&
Mg and Ag
distributions



Ag and Mg
distributions



b

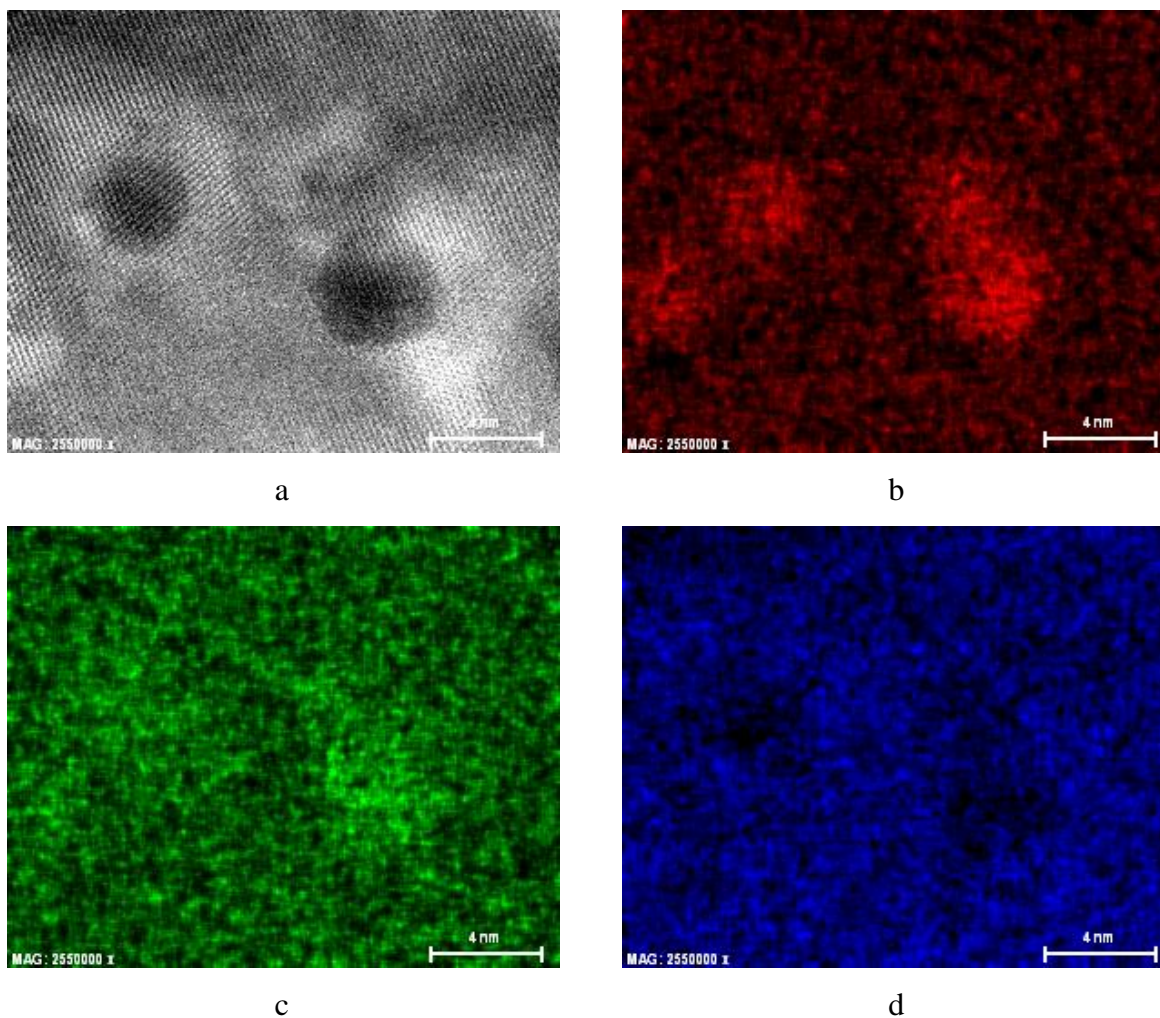


Figure 5-9: a) HAADF STEM image of the dark gray spherical nanosize MgO precipitates formed inside Ag grains of Ag/0.20wt%Mg alloy sheet after PMP, b) EDS map of Mg chemical distribution, c) EDS map of O chemical distribution, and d) EDS map of Ag chemical distribution.

Among Ag/Al alloys, the Ag/0.75wt%Al is selected and the size, shape and distribution of Al_2O_3 precipitates is studied at various conditions including as-received (without any heat treatment), after internal oxidation at 675°C for 4 hours, and after internal oxidation at 675°C for 4 hours and a PMP heat treatment.

Figure 5-10 shows HAADF STEM and HRTEM micrographs of as-received Ag/0.75wt%Al alloy sheet. The (111) plane of Ag along [110] zone axis contains no precipitate. The HRTEM image in Figure 5-10d shows various defects including stacking fault present in the (111) plane of Ag. Figure 5-11a-d demonstrates HAADF STEM micrographs of Ag/0.75wt%Al alloy sheet which is internally oxidized at 675°C for 4 hours. Furthermore, the HRTEM images of the oxidized Ag/0.75wt%Al alloy sheet are presented in Figure 5-11e-g. Dark gray Al_2O_3 precipitates are dispersed homogeneously in the (111) plane of Ag matrix having average size of $\sim 2\text{-}5$ nm. No segregation of Al_2O_3 precipitates is observed on Ag matrix grain boundaries (Figure 5-11a). HRTEM images in Figure 5-11e-g show the diffraction contrast caused by the misfit strain field around each precipitate. Figure 5-12 shows the HAADF STEM and HRTEM micrographs of Ag/0.75wt%Al alloy sheet which is internally oxidized at 675°C for 4 hours after PMP. The Al_2O_3 precipitates maintain their size, spacing and shape after PMP heat treatment. They have average size of $\sim 2\text{-}5$ nm and mostly exhibit coherent interfaces with the Ag matrix same as the Al_2O_3 precipitates in the only oxidized Ag/0.75wt%Al alloy sheet before PMP shown in Figure 5-11.

For the type of coherent Al_2O_3 precipitates formed in the Ag/Al alloys after internal oxidation, although Ashley and Smith [12] have reported the oxide in internally oxidized Cu/Al alloys to be of the $\gamma\text{-Al}_2\text{O}_3$ type, here, electron diffraction techniques have failed to reveal a crystal structure other than pure Ag in the internally oxidized Ag/Al alloys. Thus, for the formation of these precipitates, the model of Wriedt and Darken [13] will be adopted, in which it is assumed that the O atoms diffuse to the substitutionally dissolved Al atoms in the Ag matrix and take up the six octahedral interstices surrounding it. An Al atom diffusing to an adjacent substitutional site undergoes a similar oxidation until a well defined oxide particle is formed. During this process, only a relatively small volume change occurs which can be accommodated elastically by the Ag matrix. Therefore, these nanosize Al_2O_3 precipitates have coherent interfaces with the Ag matrix.

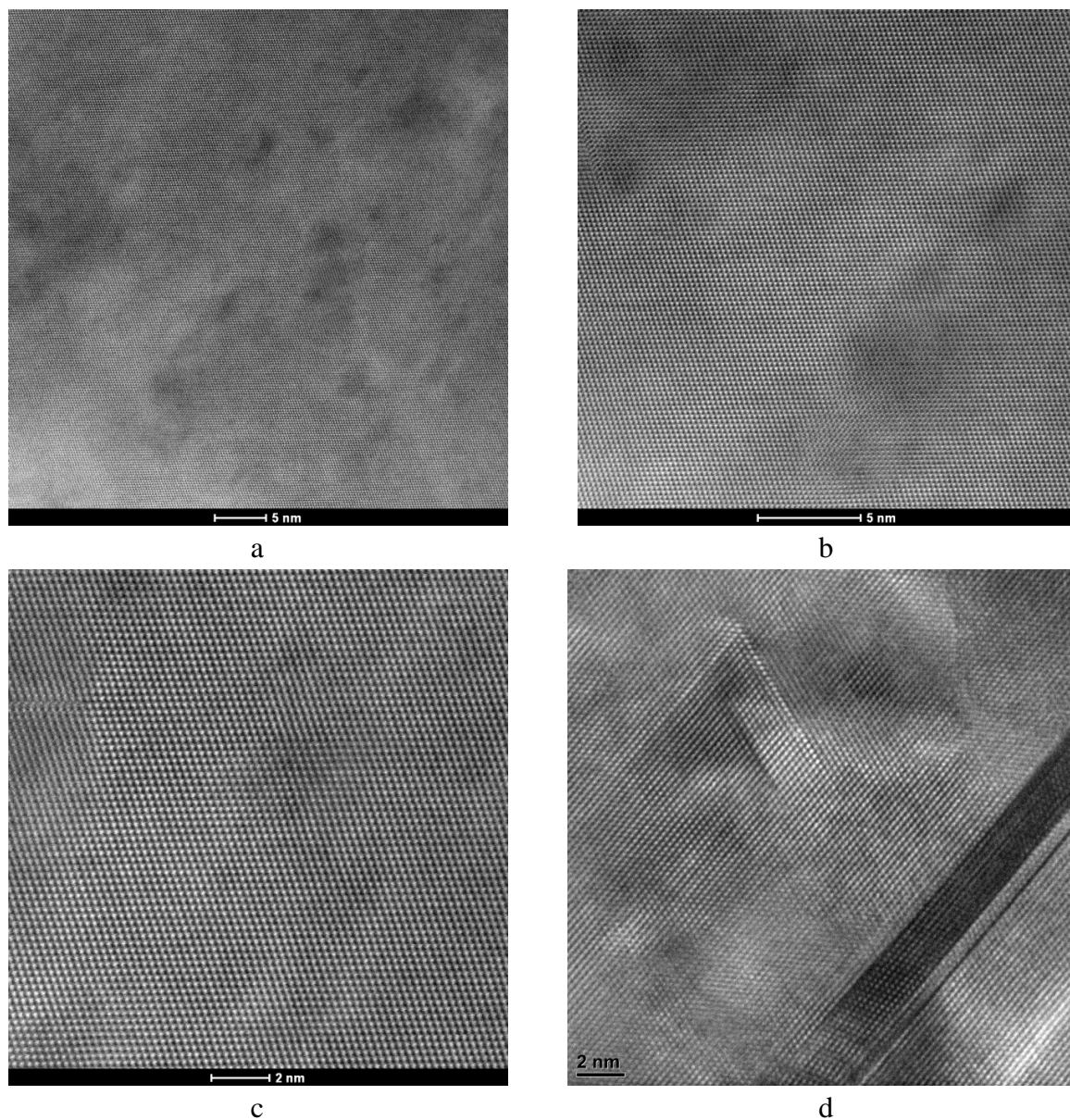
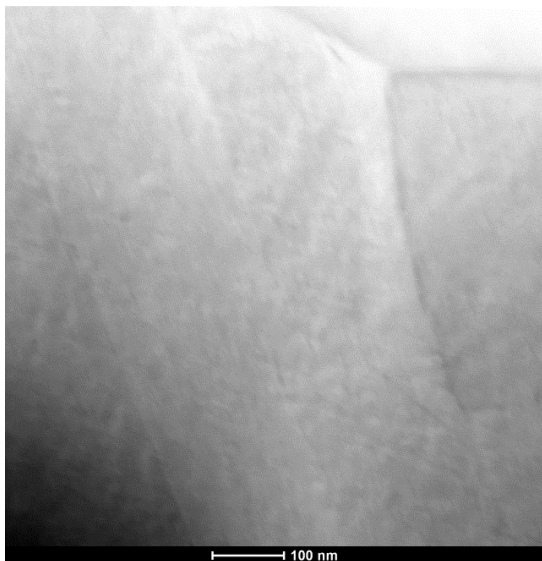
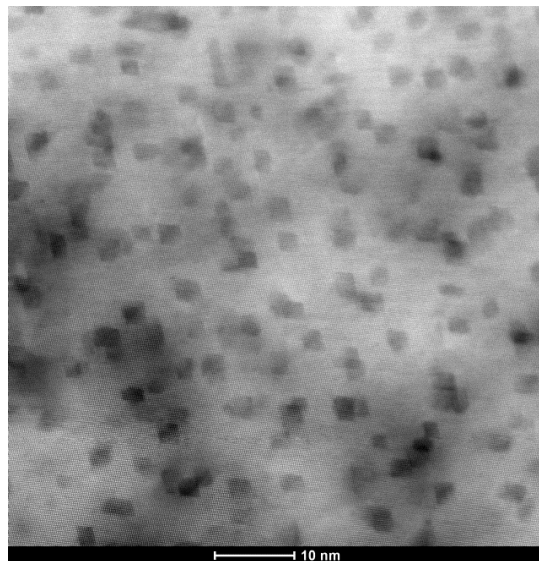


Figure 5-10: (a-c) HAADF STEM micrographs of as-received Ag/0.75wt%Al alloy sheet, and d) HRTEM image of as-received Ag/0.75wt%Al alloy sheet showing diffraction contrast of various defects, e.g. stacking faults in the (111) plane of Ag.

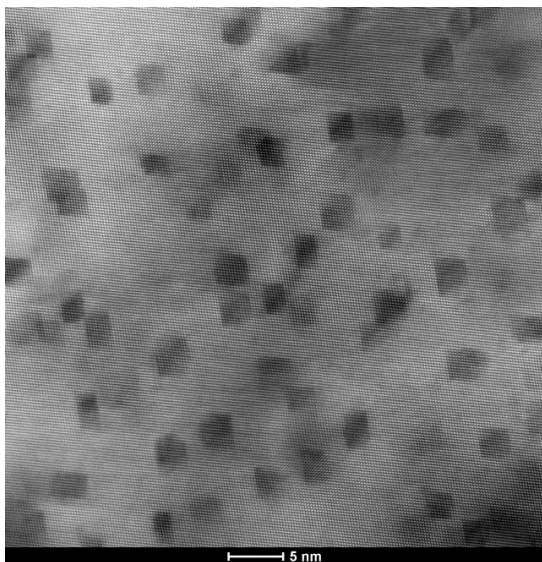
Figure 5-11: (a-d) HAADF STEM micrographs of Ag/0.75wt%Al alloy sheet internally oxidized at 675°C for 4 hours, and (e-g) HRTEM images of Ag/0.75wt%Al alloy sheet internally oxidized at 675°C for 4 hours showing diffraction contrast of various defects and misfit strain fields around each precipitate.



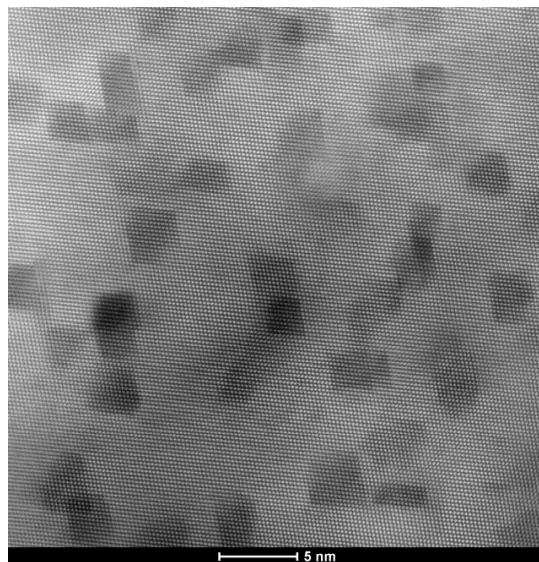
a



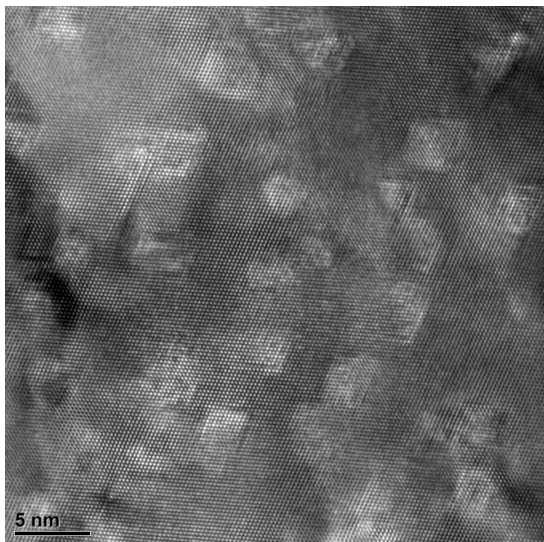
b



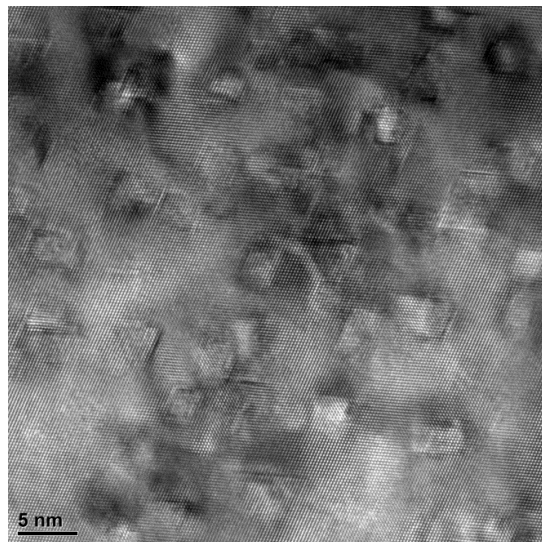
c



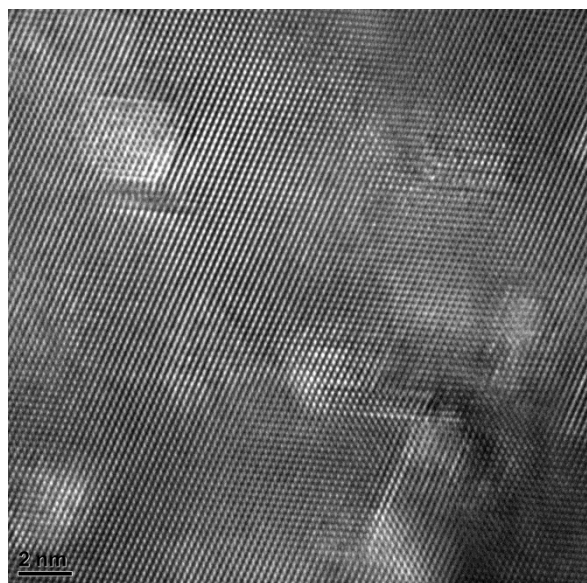
d



e



f



g

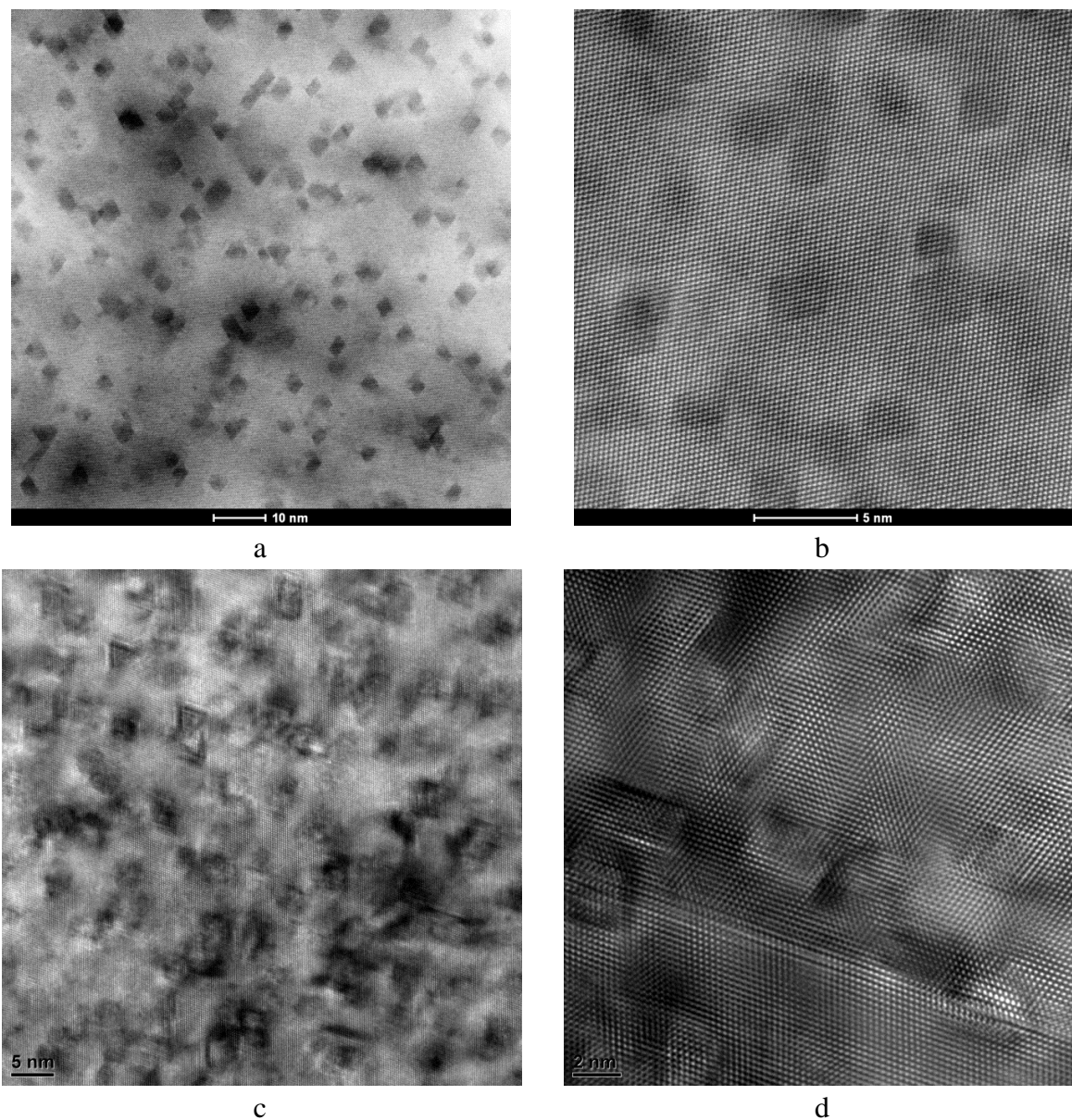
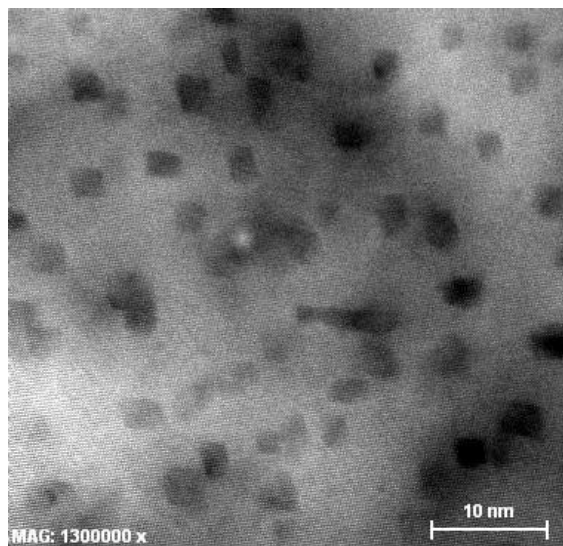


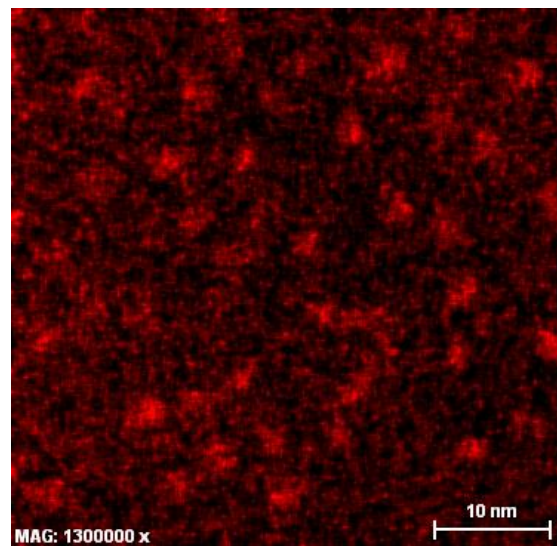
Figure 5-12: (a,b) HAADF STEM micrographs of Ag/0.75wt%Al alloy sheet internally oxidized at 675°C for 4 hours after PMP, and (c,d) HRTEM images of Ag/0.75wt%Al alloy sheet internally oxidized at 675°C for 4 hours after PMP.

EDS elemental mapping is used to examine the chemical composition of precipitates in the Ag/Al alloy sheet. Figure 5-13 shows the EDS maps of the precipitates in the internally oxidized Ag/0.75wt%Al alloy sheath after PMP heat treatment including HAADF STEM images along with Al, O and Ag chemical distributions. The EDS mappings confirm that the dark gray precipitates in Figures 5-11 and 5-12 are Al_2O_3 . The Al_2O_3 precipitates are dispersed homogenously in the Ag matrix. No segregation of larger Al_2O_3 precipitates is found on the Ag matrix grain boundaries as it was the case for MgO (see Figure 5-8). Combined micrographs of HAADF STEM and Al chemical distribution, and a combined image of Ag and Al chemical distributions is also presented in Figure 5-13.

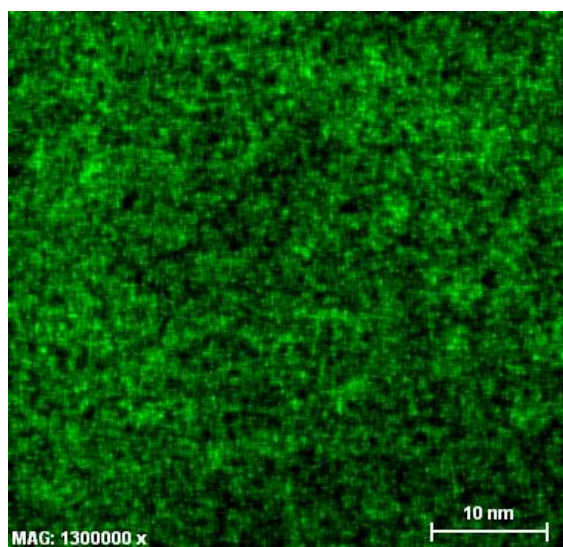
Figure 5-13: a) HAADF STEM micrographs of Ag/0.75wt%Al alloy sheet internally oxidized at 675°C for 4 hours after PMP, b) EDS map of Al chemical distribution, c) EDS map of O chemical distribution, d) EDS map of Ag chemical distribution, e) combined HAADF STEM image and EDS map of Al chemical distribution, and f) combined EDS maps of Ag and Al chemical distributions.



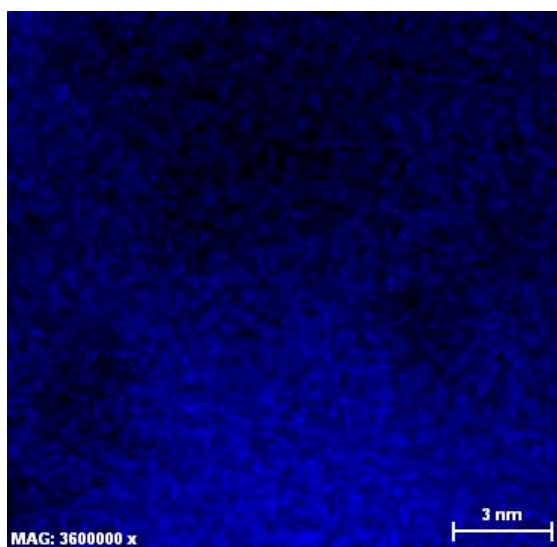
a



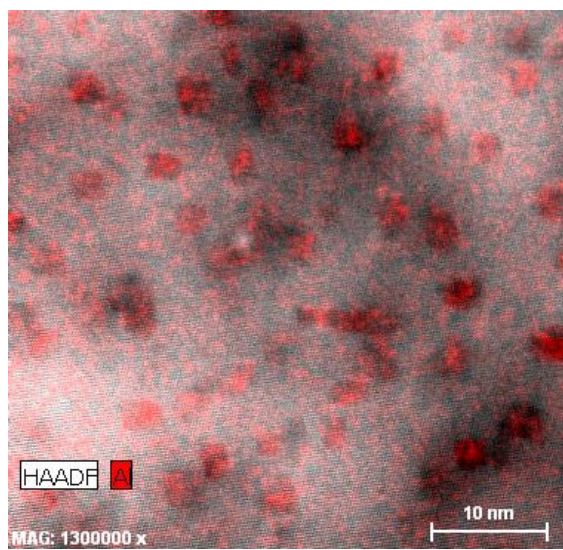
b



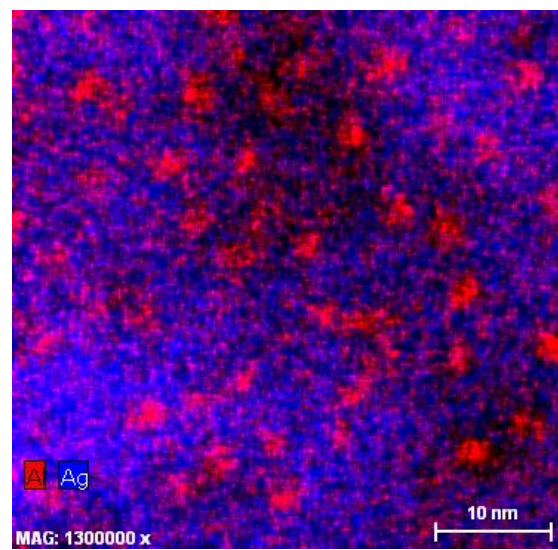
c



d



e



f

5.3.1.3. Tracking of Cu diffusion using high resolutions EDS mapping

As mentioned earlier, the Mg available in the Ag/0.20wt%Mg outer alloy sheath of Bi2212/Ag0.20Mg wire is a sink for Cu from Bi2212 filament core. Mg reacts with Cu that diffuses out from the Bi2212 cores during heat treatment into the Ag/0.20wt%Mg alloy matrix, forming $Mg_{1-x}Cu_xO$ compounds, depleting Cu from the Bi2212 cores and reducing critical current density (J_c) [8, 9].

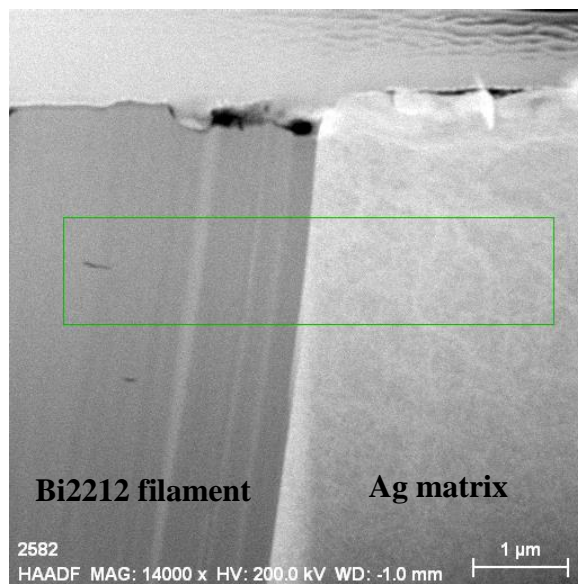
TEM samples are lifted-out from the nearest Bi2212 single filament to the outer alloy sheath in the Bi2212/Ag0.2Mg and Bi2212/Ag0.75Al wires to study the elemental distributions using high resolution EDS mappings. These samples are lifted-out from the interface of Bi2212 filament with the Ag matrix in a way that half of the sample comes from Bi2212 filament and the other half is extracted from Ag matrix. Next, EDS mappings and line scans are performed to trace Cu and other elements diffusion during PMP heat treatment.

Figure 5-14 shows HAADF STEM micrograph along with EDS maps for Ag, Cu, O, Mg, Bi, Sr, and Ca chemical distributions of the sample lifted-out from the interface of Bi2212 filament and Ag matrix in the Bi2212/Ag0.20Mg wire after PMP. Figure 5-15 illustrates the EDS line scan for Cu and Ag chemical distributions and the EDS spectrum which is acquired only from the Ag matrix.

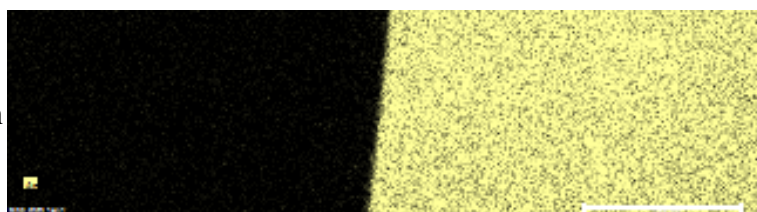
Figure 5-16 shows HAADF STEM micrograph along with EDS maps for Ag, Cu, O, Al, Bi, Sr, and Ca chemical distributions of the sample lifted-out from the interface of Bi2212 filament and Ag matrix in the Bi2212/Ag0.75Al wire after PMP. Figure 5-17 illustrates the EDS line scan for Cu and Ag chemical distributions and the EDS spectrum which is acquired only from the Ag matrix.

Figure 5-14: a) HAADF STEM micrograph of Bi2212 filament interface with Ag matrix in the Bi2212/Ag0.20Mg wire after PMP along with EDS maps of Ag, Cu, O, Mg, Bi, Sr, and Ca chemical distributions.

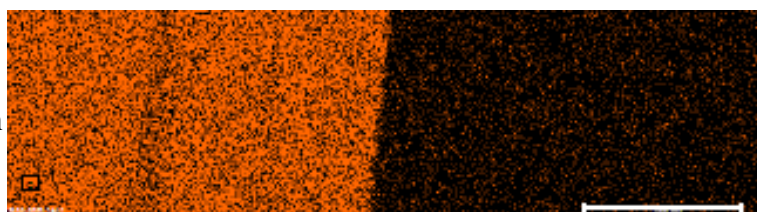
HAADF STEM



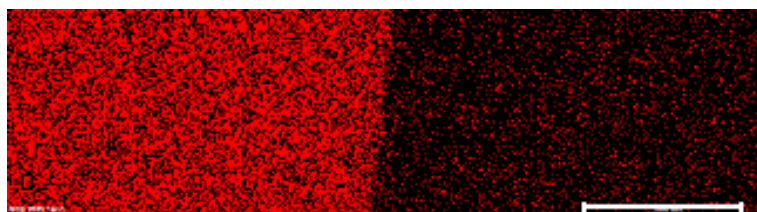
Ag distribution



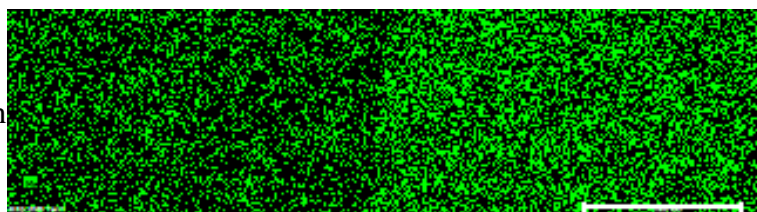
Cu distribution

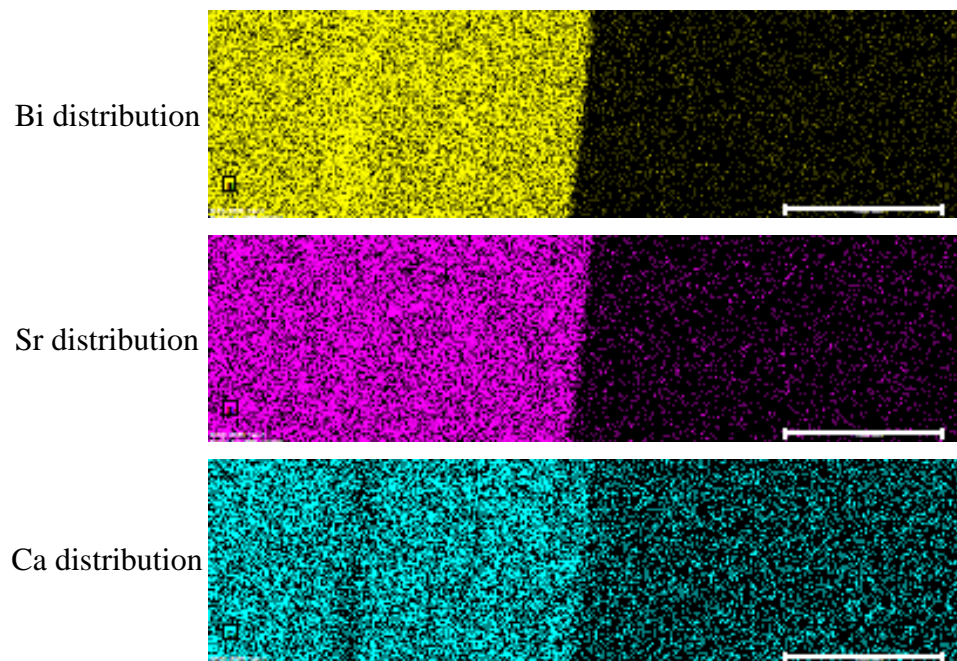


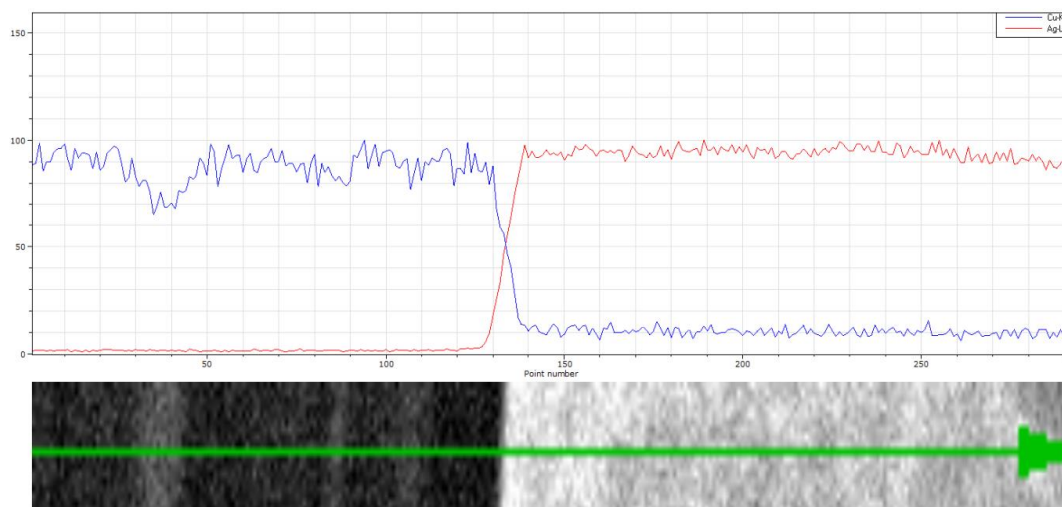
O distribution



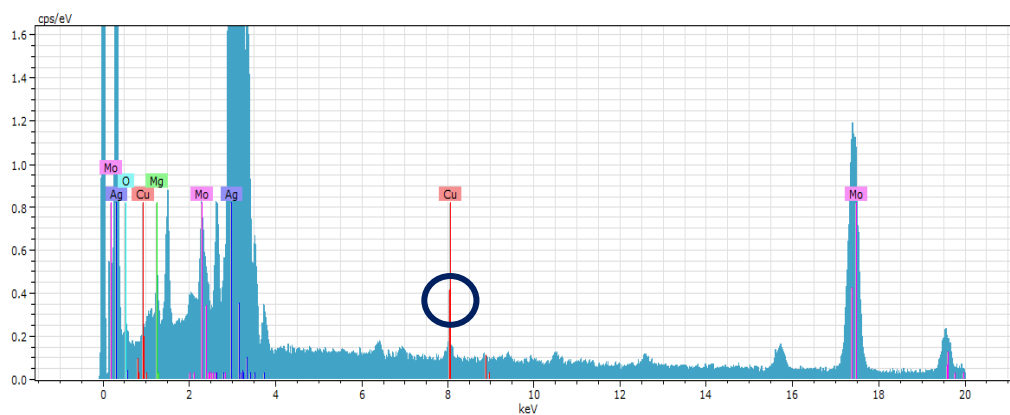
Mg distribution







a



b

Figure 5-15: a) EDS line scan showing Cu chemical distribution throughout the entire sample, and b) EDS spectrum acquired only from the Ag matrix showing the amount of Cu diffused out of Bi2212/Ag0.20Mg filament core during PMP.

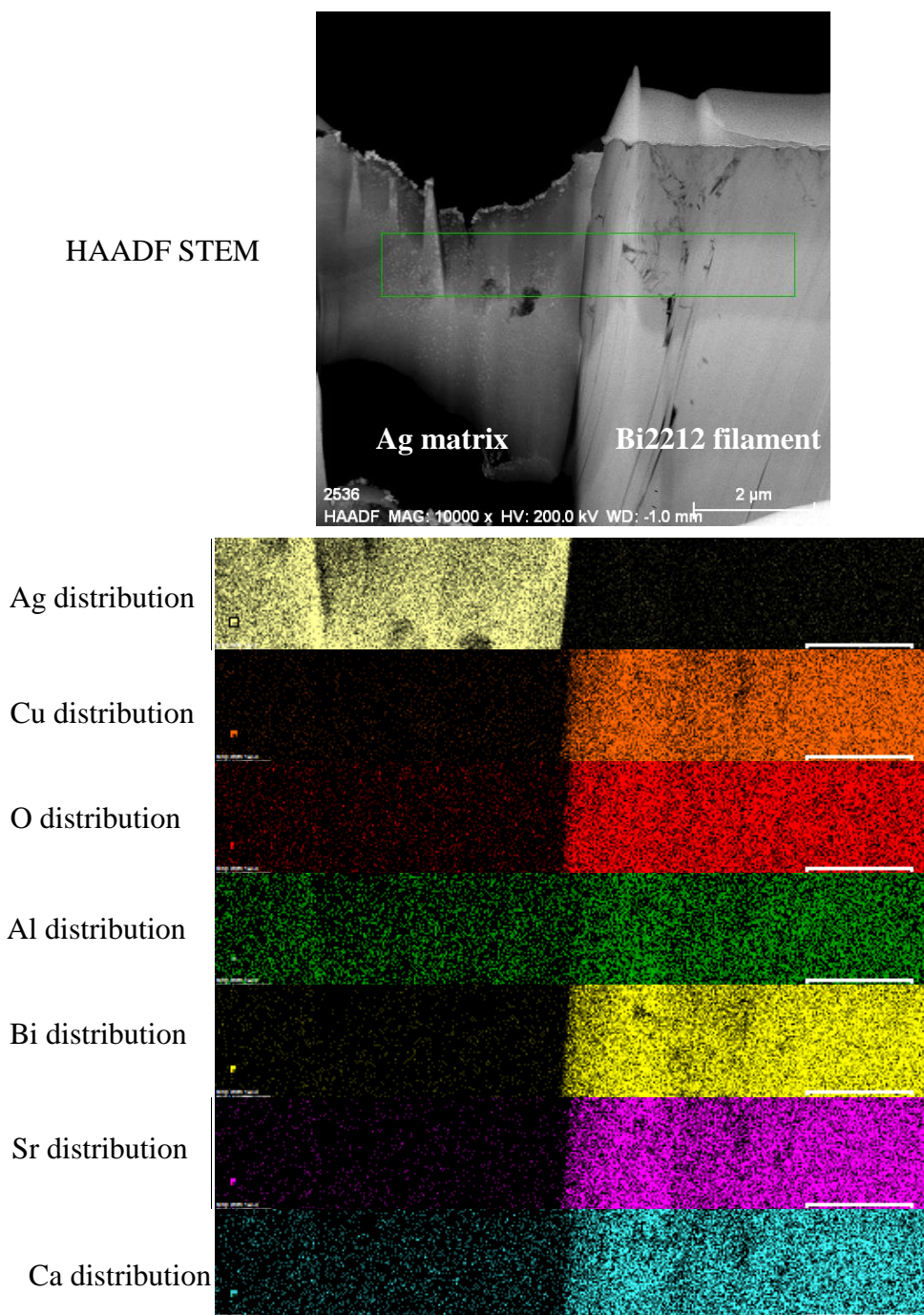
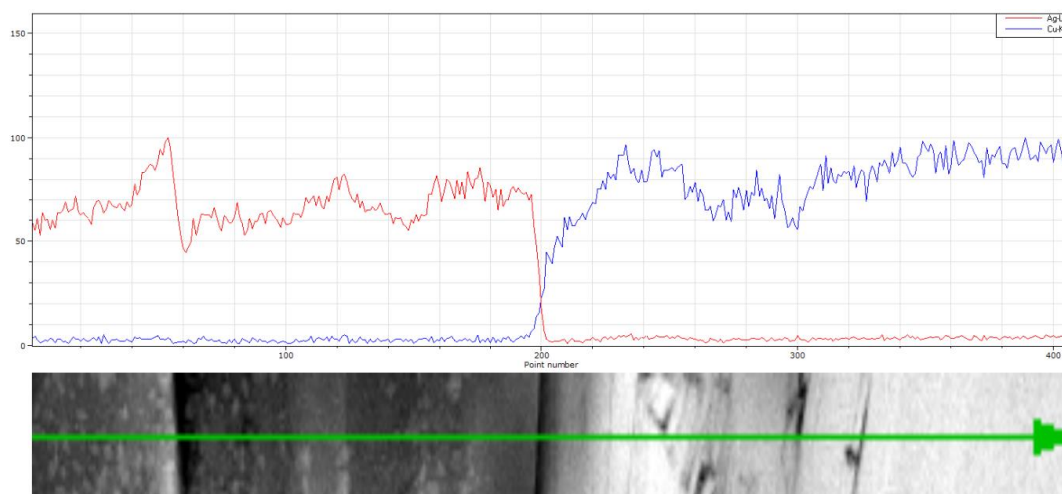
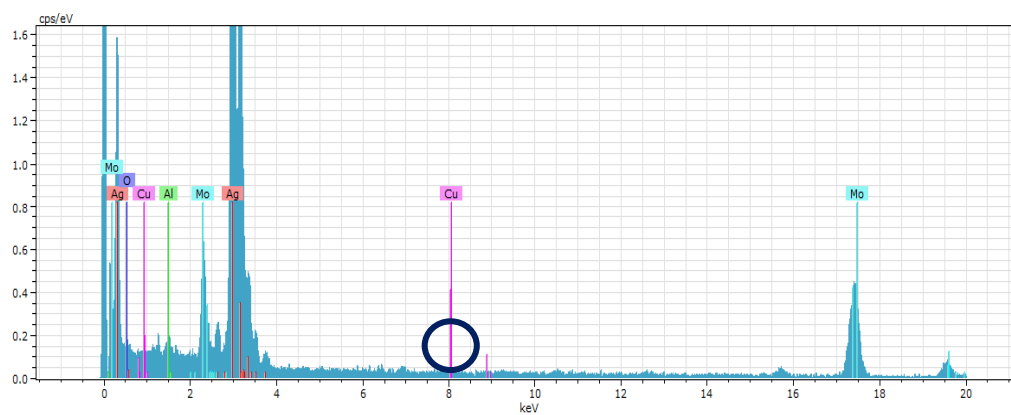


Figure 5-16: a) HAADF STEM micrograph of Bi2212 filament interface with Ag matrix in the Bi2212/Ag0.75Al wire after PMP along with EDS maps of Ag, Cu, O, Al, Bi, Sr, and Ca chemical distributions.



a



b

Figure 5-17: a) EDS line scan showing Cu chemical distribution throughout the entire sample, and b) EDS spectrum acquired only from the Ag matrix showing the amount of Cu diffused out of Bi2212/Ag0.75Al filament core during PMP.

5.3.2. Mechanical behavior

5.3.2.1. Hardness measurement

Table 5-2 summarizes the HVN measured on the outer alloy sheathes of Bi2212 wires at various conditions. The outer alloy sheathes in the green wires of Bi2212/Ag0.20Mg, Bi2212/Ag0.50Al, Bi2212/Ag0.75Al, Bi2212/Ag1.00Al, and Bi2212/Ag1.25Al are soft with HVNs of 58, 85, 89, 91, and 93, respectively. After internal oxidation, the Ag/Al outer alloy sheath transforms to DS Ag/Al alloy by formation of nanosize Al_2O_3 precipitates dispersed in the Ag matrix and the HVN increases for all Bi2212/AgAl wires by about 120%. The HVN values after oxidation are consistent with the Al content in the Ag/Al alloy. With increasing Al content, the Al_2O_3 precipitate content increases resulting in an increased HVN.

Bi2212/AgAl wires which are PMP heat treated without prior oxidation show nearly 100% increase in HVN relative to green wires. After PMP, the HVN of wires that were first internally oxidized decreases by about 10% relative to the wires that were only oxidized. This is due to some degree of Al_2O_3 precipitates coarsening during PMP, reducing the number of oxide precipitates in the Ag matrix and increasing the grain size.

In the case of Bi2212/Ag0.20Mg, the Ag/0.20wt%Mg outer alloy sheath strengthening occurs during PMP in oxygen. A dispersion of nanosize MgO precipitates forms in the Ag matrix and the HVN increases to 102. After PMP, the Bi2212/Ag0.50Al, Bi2212/Ag0.75Al,

Bi2212/Ag1.00Al, Bi2212/Ag1.25Al wires have 62%, 79%, 96% and 110% higher HVN than the Bi2212/Ag0.20Mg wire.

Table 5-2: HVN measured on the outer alloy sheath of Bi2212 wires at various heat treatment conditions					
Condition	Bi2212/ Ag0.2Mg	Bi2212/ Ag0.5Al	Bi2212/ Ag0.75Al	Bi2212/ Ag1.0Al	Bi2212/ Ag1.25Al
As-drawn	58 ± 5	85 ± 1	89 ± 1	91 ± 1	93 ± 1
Oxidized	-	180 ± 5	190 ± 5	215 ± 4	232 ± 3
As-drawn + PMP	102 ± 5	165 ± 6	182 ± 6	200 ± 4	218 ± 4
Oxidized+ PMP	-	160 ± 4	170 ± 8	188 ± 4	202 ± 4

5.3.2.2. Tensile behavior

Table 5-3 summarizes the room temperature tensile test results, including Young's modulus (E), yield strength (YS), ultimate tensile strength (UTS) and elongation to failure (El%) for all wires tested. Bi2212/Ag0.50Al and Bi2212/Ag0.75Al green wires have YS of 110 MPa which is 57% higher than that of Bi2212/Ag0.20Mg. These two wires also have UTS of ~163 MPa, which is 22% higher than that of Bi2212/Ag0.20Mg green wire. Bi2212/Ag1.00Al and Bi2212/Ag1.25Al green wires have YS of 120 MPa and average UTS of 175 MPa; i.e. 72%

and 31% higher than green Bi2212/Ag0.20Mg wire. All Bi2212/AgAl green wires have elongation to failure of about 18% which is close to that of Bi2212/Ag0.20Mg green wire.

Internal oxidation strengthens the outer alloy sheathes of Bi2212/AgAl wires by forming DS Ag/Al alloys [14, 15]. After oxidation, the YS of all four Bi2212/AgAl wires increases by about 20% in comparison to as-drawn (green) wires, whereas the UTS values decrease nearly 15%. By forming nanosize oxide precipitates in the DS Ag/Al outer alloy sheath, the wire becomes stiffer and more brittle with higher YS, but smaller UTS.

After PMP, the Bi2212/AgAl wires are much stronger and stiffer than the Bi2212/Ag0.20Mg wire. The Elastic modulus (E) of the Bi2212/Ag0.20Mg is 53 GPa, whereas for the Bi2212/AgAl, E ranges from 65-75 GPa. Furthermore, after PMP, the Bi2212/AgAl wires show 25-48% higher YS than that of Bi2212/Ag0.20Mg. After PMP, the UTS of Bi2212/Ag0.50Al wire is higher than Bi2212/Ag0.20Mg, but those of Bi2212/Ag0.75Al, Bi2212/Ag1.00Al and Bi2212/Ag1.25Al wires are close to that of Bi2212/Ag0.20Mg. Furthermore, the elongations to failures of Bi2212/AgAl wires are all substantially higher (38%-86%) than that of Bi2212/Ag0.20Mg wire. Note that the YS and E are more important for magnets than the UTS because above the YS (a critical strain), the Bi2212 filaments begin to break and the conductors' J_c decrease permanently.

5.3.3. Transport measurement

Transport measurement results for the identically heat treated Bi2212 wires are presented in Table 5-4. The J_c , 4.2K and self-field, of Bi2212/Ag0.75Al is 26% higher than that of Bi2212/Ag0.20Mg, whereas the other Bi2212/AgAl wires have 16%-20% lower J_c . Transport results obtained from a non-optimized PMP heat treatment show that the presence of Al_2O_3 precipitates in the outer alloy sheath of Bi2212/AgAl wires do not significantly effect on the oxygen solubility or oxygen diffusion through the Ag/Al outer alloy sheath. Therefore, most probably these Al_2O_3 precipitates do not also have any detrimental reactions with the Bi2212 oxide phase. More detailed studies are necessary to obtain a better understanding of electrical behavior of fabricated Bi2212/AgAl wires.

Table 5-3: Room temperature tensile test results for Bi2212 round wires					
Samples type	Condition	E (GPa)	YS (MPa)	UTS (MPa)	EI %
Bi2212/Ag0.20Mg	Green wire	50	70	134	18.00
	PMP	53	100	150	0.96
Bi2212/Ag0.50Al	Green wire	52	110	161	18.11
	Oxidized	63	130	147	0.52
	PMP	75	138	178	1.81
Bi2212/Ag0.75Al	Green wire	50	110	165	18.21
	Oxidized	57	130	138	0.51
	PMP	73	148	152	1.52
Bi2212/Ag1.00Al	Green wire	48	120	170	17.81
	Oxidized	65	136	150	0.95
	PMP	65	132	141	1.36
Bi2212/Ag1.25Al	Green wire	54	120	177	17.91
	Oxidized	69	120	140	0.98
	PMP	67	125	143	1.32

Table 5-4: Transport measurements at 4.2K, self-field			
RW conductor	I _c (A)	n-value	J _c (A/mm ²)
Bi2212/Ag0.20Mg	384	18	2830
Bi2212/Ag0.50Al	264	21	2340
Bi2212/Ag0.75Al	386	18	3560
Bi2212/Ag1.00 Al	265	20	2340
Bi2212/Ag1.25Al	275	22	2430

5.4. Discussion

Ag/Al alloys are made via powder metallurgy whereas Ag/0.2wt%Mg is produced from a cast ingot as a solid solution alloy. During drawing, the Ag/0.2wt%Mg alloy work hardens and loses ductility. The ductility is restored by annealing, but this annealing must be done in an inert atmosphere. If the Ag/0.2wt%Mg alloy is annealed in an oxygen containing atmosphere, MgO precipitates form on grain boundaries and results in brittleness which is problematic for continuing the cold working to the final wire diameter. Therefore, for the Ag/0.2wt%Mg alloy, only during the final PMP heat treatment is it desirable to oxidize the alloy and form MgO precipitates. In the case of Ag/Al alloy, however, powder metallurgy creates fine grain alloy microstructure which can be hardened before wire drawing.

According to the grain size measurement on the outer alloy sheathes, the as-drawn Ag/0.20wt%Mg sheath has four times larger grain size than the Ag/Al alloy in the

Bi2212/AgAl wires. The finer grain structure results in more grain boundaries which are obstacles to dislocation movement and plastic deformation. A higher strength alloy sheath can increase the compressive force on the filament core during wire drawing, improving the Bi2212 filament density [16]. Furthermore, for stiffer and stronger Bi2212 green wires, the probability of damage during handling is reduced.

Internal oxidation is performed to precipitate nanosize Al_2O_3 precipitates in the Ag/Al alloy sheath and form high strength DS Ag/Al. These oxidized samples show the largest grain size of about $10.8 \mu\text{m}$, because the starting material for internal oxidation has no precipitates which would be potent agents for prohibiting grain growth. Precipitate formation is a diffusion controlled process requiring heating at a temperature for a specific time. While the precipitates are forming during internal oxidation, some amount of grain growth occurs. Despite the largest grain sizes in the alloy sheath of the oxidized wires (Figure 5-3), these wires have the highest HVN values, confirming Al_2O_3 precipitates formation and their impact on DS Ag/Al alloy strength.

Both as-drawn and internally oxidized wires are PMP heat treated to see the effect of adding an additional internal oxidation step on the microstructure and strength of Bi2212 wires. The oxidation process is performed for Bi2212/AgAl wire during PMP without a separate internal oxidation heat treatment. The as-drawn wires which are directly PMP heat treated have smaller grain size (about $7.5 \mu\text{m}$) and slightly higher HVN than those which are internally

oxidized and PMP heat treated. The differences in HVN values for these two conditions is small but the smaller grain size of as-drawn wires which are directly PMP heat treated is worth noting. Therefore, this is a preferred condition for Bi2212/AgAl wires. The higher strength in Bi2212/AgAl wires mostly comes from higher Al content and greater volume fraction of oxide precipitates dispersed in the Ag matrix.

HAADF STEM studies show that the average size of Al_2O_3 precipitates is slightly smaller than that of MgO. Owing to the large difference in oxygen affinity between Mg and Al with Ag, formed MgO and Al_2O_3 precipitates are expected to be very small [10]. Large MgO precipitates preferentially localized at the Ag grain boundaries in the Ag/0.20wt%Mg alloy sheath, whereas smaller MgO precipitates formed inside the Ag matrix. By use of powder metallurgy for making Ag/Al alloys, the Al presents as solid solution in the Ag matrix is homogeneously distributed, thus, after internal oxidation, uniform and small size Al_2O_3 precipitates form in the entire Ag matrix. No segregations of Al exists on the Ag grain boundaries as is the case for Ag/0.20wt%Mg alloy which is a cast product; therefore, the precipitation of large Al_2O_3 particles on grain boundaries is impeded for DS Ag/Al alloy. The existence of large MgO precipitates on the grain boundaries of Ag/0.20wt%Mg alloy sheath makes it brittle (see Figures 5-6b and c and Table 5-3). In the case of Ag/Al alloy sheaths, higher amount of Al content results in higher volume fraction of Al_2O_3 precipitates, thus, greater HVN and strength values obtain. The tensile behaviors are more relevant to the Bi2212 applications than HVN. As indicated in Table 5-3, after PMP, Bi2212/AgAl wires

show E and elongation to failures which are nearly 32% and (38%-86%) higher than that of Bi2212/Ag0.20Mg, respectively. After PMP, Bi2212/Ag1.00Al and Bi2212/1.25Al have E, YS and elongation to failures that are slightly smaller than those of Bi2212/Ag0.50Al and Bi2212/Ag0.75Al. This is probably due to higher amount of Al₂O₃ precipitates formed in the outer sheathes of these wires with higher Al content that make them more brittle. Although Bi2212/Ag1.00Al and Bi2212/Ag1.25Al wires strengths are lower than those of Bi2212/Ag0.50Al and Bi2212/Ag0.75Al, but these wires still show improvements for their stiffness and toughness comparing to those of Bi2212/Ag0.20Mg. Bi2212/Ag0.75Al shows the best mechanical properties along with the highest J_c among all Bi2212/AgAl wires.

Majewski et al. studied the diffusion of Cu into the Ag sheath of Bi2212 and they reported that the Cu diffusion coefficient appears to be about two orders of magnitude faster in the Ag/0.20wt%Mg alloy sheath than that of pure Ag sheathed Bi2212 and the main reason is the presence of MgO precipitates in the Ag/0.20wt%Mg alloy sheath [8, 9]. Paranthaman et al. [17] investigated the phase equilibrium of the MgO-CuO system and they found that CuO is quite soluble in the MgO. The solubility of CuO in MgO at the partial melt temperature of Bi2212 is ~20%. The Cu that pumps out of the Bi2212 melt during heat treatment; reduces the amount of formed Bi2212 filaments and degrades the conductor's J_c.

Wesolowski et al. [18] studied the reactions between oxides and Ag sheathed Bi2212 wires and tapes and reported Al₂O₃ as one of the non-reactive oxide when heat treated in contact

with Ag sheathed Bi2212 tape. Our high resolution EDS elemental mappings show that Cu is present in the Ag/0.20wt%Mg outer alloy sheath of Bi2212/Ag0.20Mg wire and the amount of Cu is higher around large spherical MgO precipitates on the Ag grain boundaries (Figure 5-8a). Furthermore, to compare the effect of Al₂O₃ precipitates present in the Ag/Al outer alloy sheaths of Bi2212/AgAl wires with that of Ag/0.20wt%Mg outer alloy sheath in the Bi2212/Ag0.20Mg wire, EDS line scans and EDS spectrums are collected for the samples lifted-out from the Bi2212 filament interfaces with the Ag matrix. As can be seen in EDS elemental mappings showing Cu chemical distributions in Figures 5-14 and 5-16, the amount of Cu diffused out of Bi2212/Ag0.20Mg filament toward the Ag/0.20wt%Mg outer alloy sheath is higher than that of Bi2212/Ag0.75Al filament toward Ag/0.75wt%Al outer alloy sheath. Moreover, the EDS line scans and EDS spectrums for Cu elemental distributions in Figures 5-15 and 5-17 confirm the higher amount of Cu diffused out of filament core in the Bi2212/Ag0.20Mg wire than that of Bi2212/Ag0.75Al wire. Diffusing of Cu outside the Bi2212 filament during PMP would change the Bi2212 stoichiometry and degrades the conductor's J_c . Therefore, using a higher strength DS Ag/Al alloy sheath which is less reactive with Cu for making Bi2212 could be beneficial to improve both electrical properties of conductor along with increasing its stiffness and strength.

5.5. Summary

Ag/Al alloys with various Al content are made by powder metallurgy and used for fabrication of Bi2212/AgAl RW conductors. Microstructure, mechanical and electrical

behavior of Bi2212/AgAl wires with a focus on the strength of outer alloy sheath is studied. Samples are tested at various conditions, including as-drawn, after internal oxidation, and after a PMP heat treatment; the properties of Bi2212/AgAl are compared with those of Bi2212/Ag0.20Mg. Bi2212/AgAl green wires have smaller grain size and nearly 55% higher HVN than Bi2212/Ag0.20Mg. After PMP, they have comparable grain size with Bi2212/Ag0.20Mg, but significantly higher HVN and YS values which is mainly due to higher amount of Al₂O₃ oxide precipitates form in the Ag matrix via internal oxidation because of higher Al content. Furthermore, transport measurements show that the Al₂O₃ precipitates in the outer alloy sheath of Bi2212/AgAl wires have neither any detrimental reactions with the Bi2212 oxide phase nor any significant effect on oxygen solubility or oxygen diffusion through the sheath. HAADF STEM studies demonstrate the formation of nanosize MgO and Al₂O₃ precipitates via internal oxidation. Large spherical MgO precipitates are formed on the Ag grain boundaries of Ag/0.20wt%Mg outer alloy sheath, whereas the Al₂O₃ precipitates are distributed homogenously in the DS Ag/Al alloy. These large MgO precipitates make the Bi2212/Ag0.20Mg more brittle than Bi2212/AgAl wires. High resolution EDS elemental mappings demonstrate the less Cu diffused out of filament cores in the Bi2212/Ag0.75Al wire during PMP than that of Bi2212/Ag0.20Mg. DS Ag/Al alloy is a potential candidate for strengthening Bi2212 conductor by improving its modulus and stiffness. Furthermore, stronger outer alloy sheath can apply higher compressive force during wire fabrication and this result in denser filament cores which is beneficial to improve critical current density (J_c).

5.6. References cited

- [1] S. J. Pennycook, "Z-contrast stem for materials science," *Ultramicroscopy*, vol. 30, pp. 58-69, 1989.
- [2] S. J. Pennycook and D. E. Jesson, "High-resolution incoherent imaging of crystals," *Physical Review Letters*, vol. 64, pp. 938-941, 1990.
- [3] S. J. Pennycook and D. E. Jesson, "High-resolution Z-contrast imaging of crystals," *Ultramicroscopy*, vol. 37, pp. 14-38, 1991.
- [4] S. J. Pennycook, *et al.*, "Elemental mapping with elastically scattered electrons," *Journal of Microscopy*, vol. 144, pp. 229-249, 1986.
- [5] R. E. Koritala, *et al.*, "Microstructure and mechanical properties of internally oxidized Ag/1.12 at.% Mg," *AIP Conference Proceedings*, vol. 614, pp. 768-776, 2002.
- [6] A. Combe and J. Cabane, "Mechanism of internal oxidation in silver alloys," *Oxidation of Metals*, vol. 21, pp. 21-37, 1984/02/01 1984.
- [7] A. Charai and G. Nihoul, "High-resolution phase images of nano-precipitates inside a matrix: Contribution of diffraction and deformation phenomena," *Philosophical Magazine A*, vol. 58, pp. 571-588, 1988/10/01 1988.
- [8] P. Majewski, *et al.*, "Diffusion of Cu into the Ag sheath of BPSCCO tapes," *Physica C: Superconductivity*, vol. 325, pp. 8-12, 1999.
- [9] P. Majewski, *et al.*, "Cu diffusion into Ag during BSCCO tape processing," *Physica C: Superconductivity*, vol. 351, pp. 62-66, 2001.

- [10] L. Charrin, *et al.*, "Reactivity at macroscopic, meso and microscopic scale in oxidized silver magnesium alloys," *Scripta Materialia*, vol. 42, pp. 701-709, 2000.
- [11] L. Charrin, *et al.*, "Evidence for the formation of substoichiometric species during internal oxidation of Ag-Mg alloys," *Oxidation of Metals*, vol. 40, pp. 483-501, 1993/12/01 1993.
- [12] M. F. Ashby and G. C. Smith, "Direct electron microscopy of thin foils of internally oxidized dilute copper alloys," *Philosophical Magazine*, vol. 5, pp. 298-&, 1960.
- [13] L. S. Darken, *Transactions of the American Society Meeting* vol. 54, p. 600, 1961.
- [14] A. Kajbafvala, *et al.*, "High strength oxide dispersion strengthened silver aluminum alloys optimized for $\text{Bi}_2\text{Sr}_2\text{CaCu}_2\text{O}_{8+x}$ round wire," *Superconductor Science and Technology*, vol. 26, 125012, p. 9, 2013.
- [15] A. Kajbafvala, *et al.*, "Dispersion-Strengthened Silver Alumina for Sheathing $\text{Bi}_2\text{Sr}_2\text{CaCu}_2\text{O}_{8+x}$ Multifilamentary Wire," *IEEE Transactions on Applied Superconductivity*, vol. 22, p. 8400210, Feb 2012.
- [16] Z. Han and T. Freltoft, "The mechanical deformation process for preparing Ag-sheathed BiSrCaCuO superconducting tapes," *Applied Superconductivity*, vol. 2, pp. 201-215, 1994.
- [17] M. Paranthaman, *et al.*, "Phase equilibria of the $\text{MgO-Cu}_2\text{O-CuO}$ system," *Materials Research Bulletin*, vol. 32, pp. 165-173, 1997.
- [18] D. E. Wesolowski, *et al.*, "Reactions between oxides and Ag-sheathed $\text{Bi}_2\text{Sr}_2\text{CaCu}_2\text{O}_x$ conductors," *Superconductor Science and Technology*, vol. 18, p. 934, 2005.

CHAPTER 6

Conclusions and Future Work

6.1. Conclusions

This dissertation presents a systematic investigation on developing a high strength and high modulus dispersion-strengthened (DS) Ag/Al alloy sheath for fabrication of $\text{Bi}_2\text{Sr}_2\text{CaCu}_2\text{O}_{8+x}$ (Bi2212) round wire (RW) conductor.

In the chapter 3, a DS Ag/0.5wt%Al alloy manufactured via powder metallurgy with an internal oxidization process was used for making double restack Bi2212/Ag0.50Al multifilamentary round wire (RW) conductor. The DS Ag/0.50wt%Al alloy was used as the outer sheath while pure Ag was used for the inner sheath of Bi2212 next to the filament. The DS Ag/0.50wt%Al metal powder was made by inert gas atomization and internally oxidized at 675-700°C for 24 hours in the flow of 100% oxygen. The oxidized powders were then used for making DS Ag/0.50wt%Al solid alloy wires and sheets. Next, the pre-oxidized and hardened DS Ag/0.50wt%Al alloy sheath was used for making Bi2212/Ag0.50Al wire. Microstructure, mechanical and electrical properties of DS Ag/0.50wt%Al solid alloy wires and sheets and Bi2212/Ag0.50Al wire are studied and compared [1]. In chapter 4, the relationships between the processing and oxidation of Ag/Al alloys with various Al contents and their microstructure, mechanical and electrical properties were investigated. A series of

Ag/Al alloys were studied and the internal oxidation time and temperature were varied to optimize the strength, ductility and microstructure after partial melt processing (PMP) heat treatment [2]. In chapter 5, the microstructure, mechanical and electrical behavior of double-restack Bi2212/Ag/AgAl wires made by various Ag/Al alloy compositions were studied. Furthermore, HAADF STEM and HRTEM imaging were used to study the size, shape and distribution of MgO and Al₂O₃ precipitates formed in the Ag/0.20wt%Mg and DS Ag/Al alloys during internal oxidation [3].

The main findings of this dissertation can be summarized as follow:

- DS Ag/0.50wt%Al alloy for sheathing Bi2212 RW
 - ✓ The non-optimized DS Ag/0.50wt%Al solid alloy wire showed high yield strength (YS) and ultimate tensile strength (UTS) in the annealed condition at both room temperature (RT) and 4.0 K. The DS Ag/0.50wt%Al alloy also showed significant ductility at 4.0 K, i.e., a temperature at which Ag and Ag/0.20wt%Mg have little measurable ductility.
 - ✓ Transport measurements showed that the Bi2212/Ag0.50Al wires made by non-optimized DS Ag/0.50wt%Al alloy sheath outperform Bi2212/Ag0.20Mg wires by nearly 50%, indicating that the Al₂O₃ precipitates in the sheath have neither any significant effect on oxygen solubility or oxygen diffusion through the sheath, nor any detrimental reactions with the Bi2212 filaments.

- ✓ Tensile studies showed that the Bi2212/Ag0.50Al green wire made by non-optimized DS Ag/0.50wt%Al alloy sheath had very high strength. After PMP, the Bi2212/Ag0.50Al wire not only had YS and UTS that were slightly higher than those of Bi2212/Ag0.20Mg wire but also exhibited > 2% elongation, which was several times higher than that of Bi2212/Ag0.20Mg.

- ✓ Although leakage is often seen in similar spirals wound with Bi2212/Ag0.20Mg, no leakage had been observed after heat treatments of Bi2212/Ag0.50Al spirals.

- Oxide dispersion-strengthened Ag/Al alloys optimized for Bi2212 RW
 - ✓ The internal oxidation heat treatment was optimized to maximize the strength and modulus of DS Ag/Al alloy after PMP.

 - ✓ The Ag/Al alloy oxidized at 675-700°C for 4 hours gave the highest tensile strength and Vickers micro-hardness (HVN) after PMP.

 - ✓ The HVN, tensile tests and grain size measurements showed that the optimized DS Ag/Al alloy could retain its fine grain size and strength during PMP treatment in oxygen.

- ✓ After PMP, the mechanical properties of DS Ag/0.50wt%Al solid alloy wire internally oxidized at 675°C for 4 hours were significantly increased compared to those of Ag/0.20wt%Mg.

- Bi2212/AgAl wires with high-strength oxide dispersion-strengthened Ag/Al alloy sheathes having various Al content
 - ✓ Ag/Al alloys with various Al content (0.50, 0.75, 1.00, and 1.25 wt%) were made by powder metallurgy and used for fabrication of double restack Bi2212/AgAl wires.

 - ✓ Microstructure, mechanical and electrical behavior of Bi2212/AgAl wires with a focus on the strength of outer alloy sheath was studied.

 - ✓ Samples were tested at various conditions, including as-drawn, after internal oxidation, and after a PMP heat treatment and the properties of Bi2212/AgAl wires are compared with those of Bi2212/Ag0.20Mg.

 - ✓ Bi2212/AgAl green wires had smaller grain size and nearly 55% higher HVN than Bi2212/Ag0.20Mg.

- ✓ After PMP, they had comparable grain size with Bi2212/Ag0.20Mg, but significantly higher HVN and YS values which was mainly due to higher amount of Al₂O₃ precipitates form in the Ag matrix via internal oxidation because of higher Al content.
- ✓ HAAFD STEM studies demonstrated the formation of nanosize MgO and Al₂O₃ precipitates via internal oxidation. Large spherical MgO precipitates were formed on the Ag matrix grain boundaries of Ag/0.20wt%Mg outer alloy sheath, whereas the Al₂O₃ precipitates were distributed homogenously in the DS Ag/Al alloy. These large MgO precipitates made the Bi2212/Ag0.20Mg more brittle than Bi2212/AgAl wires.

- ✓ High resolution EDS elemental mappings demonstrated that less Cu diffused out of the Bi2212 filament cores in the Bi2212/Ag0.75Al wire during PMP than that of Bi2212/Ag0.20Mg.

- ✓ Stronger outer alloy sheath in DS Ag/Al could apply higher compressive force during Bi2212 wire fabrication and this result in denser filament cores which could be beneficial to improve critical current density (J_c).

- ✓ DS Ag/Al alloys have the potential for achieving significant improvement in Bi2212 electrical and mechanical behavior.

6.2. Recommendation for future work

- It would be interesting to optimize the temperature-time profile of partial melt processing heat treatment for fabricated Bi2212/AgAl wires to achieve the highest possible J_c .
- Porosity is a major problem in Bi2212 and removing it showed significant increase in J_c . Here, DS Ag/Al showed higher stiffness and modulus in as-drawn condition. A stronger outer alloy sheath could apply higher compressive force during Bi2212 wire drawing and this result in denser filament cores which could be beneficial to improve J_c . It would be great to study the porosity variation in the Bi2212/AgAl wires made by different Ag/Al outer alloy sheath compositions in detail and study its effect on the wires performance.
- Because of reactivity between Mg and Bi2212 oxide phase, Ag/0.2wt%Mg is only used as the outer sheath of Bi2212 wire. Since Al_2O_3 precipitates are reported in the literature and also have shown here by preliminary STEM EDS studies that are less reactive with the Cu in Bi2212, it would be interesting to study Cu diffusion using EDS line scans as well as electron energy loss spectroscopy (EELS) analysis in wires heat treated at various conditions.

- Double-restack Bi2212/AgAl wires showed significant improvement in their strength and modulus. In these wires, DS Ag/Al alloys were used only as the second restack while pure Ag was used as the first and primary tube. It would be interesting to make Bi2212 wires using Ag/Al alloy sheathes as both first and second restack tubes. Next, the maximum achievable strength and modulus could be studied. Also, any possible reaction of Al_2O_3 with Bi2212 filament can be studied when use the oxide precipitates in contact to the Bi2212 filament.

6.3. Referenced cited

- [1] A. Kajbafvala, *et al.*, "Dispersion-Strengthened Silver Alumina for Sheathing $\text{Bi}_2\text{Sr}_2\text{CaCu}_2\text{O}_{8+x}$ Multifilamentary Wire," *IEEE Transactions on Applied Superconductivity*, vol. 22, pp. 8400210-8400210, 2012.
- [2] A. Kajbafvala, *et al.*, "High strength oxide dispersion strengthened silver aluminum alloys optimized for $\text{Bi}_2\text{Sr}_2\text{CaCu}_2\text{O}_{8+x}$ round wire," *Superconductor Science and Technology*, vol. 26, p. 125012, 2013.
- [3] A. Kajbafvala, *et al.*, " $\text{Bi}_2\text{Sr}_2\text{CaCu}_2\text{O}_{8+x}$ round wires with high-strength oxide dispersion strengthened Ag/Al alloy sheath," *Superconductor Science and Technology*, To be submitted.